Spatial and Temporal Variability in the Geochemistry of Sediments at the Main Endeavour Field, Juan de Fuca Ridge

by

Melissa Mills

B.Sc (Hons), Memorial University of Newfoundland

A Thesis submitted in Partial Fulfilment
of the Requirements for the Degree of

Master of Science

In the School of Earth and Ocean Sciences

Supervisory Committee

Dr. Laurence Coogan (School of Earth and Ocean Sciences)
Co-Supervisor

Dr. Jay Cullen (School of Earth and Ocean Sciences)
Co-Supervisor

Dr. Blake Dyer (School of Earth and Ocean Sciences)
Departmental committee member

Abstract

Sediments near hydrothermal vents are enriched in metals derived directly from hydrothermal fluids (e.g., Fe, Cu, Zn, Mn) and those associated with scavenging and co-precipitation from seawater with hydrothermally derived Fe-sulfides and Fe-oxyhydroxide minerals (e.g., P, V, Co, Mo, As, REEs). The sediments surrounding active venting have high concentrations of these elements which decrease with distance from the vents due to both hydrothermal plume dilution with seawater and sedimentation of hydrothermal particles. The composition of hydrothermal sediments from the Main Endeavour Field on the Juan de Fuca Ridge, approximately 300 km off the coast of Vancouver Island, was determined using samples collected in sediment traps at three locations along a transect below the hydrothermal plume. These traps were deployed on-axis, 3 km, and 9 km off-axis allowing the spatial variability of the hydrothermal component of the sediments to be assessed. The chemical composition and mass accumulation rates of the hydrothermal component is governed by particle formation in the near vent region and is controlled by particle settling rates with distance from active venting. The concentration and mass accumulation rate of the hydrothermal component of the sediment decreases rapidly with distance, with an order of magnitude decrease between the on-axis and 3 km off axis sediment trap samples, and a further 1-2 orders of magnitude decrease from 3 km off axis to 9 km off axis.

Sediment trap samples are also used to create a high-resolution time series of hydrothermal sedimentation over the course of the approximately year sampling period, with each on-axis sample collecting 21 days of sediment and each off-axis sample collecting 12 days of sediment. These samples allowed for an initial assessment of the temporal variation in the chemical composition and mass accumulation rate of the hydrothermal sediment. The variability observed in the hydrothermal component mass accumulation rate suggests that physical oceanographic processes (e.g., flow reversal) impacts the rate of sedimentation.

The base of a 50 cm sediment core, collected 2.6 km northwest of the Main Endeavour Field, was dated at ~6,000 years and a high-resolution geochemical reconstruction is used to determine how the hydrothermal component has changed on a 100–1000 year time scale. The comparison of the sediment core to fresh sediment collected by the sediment traps is used to understand how post-depositional changes affect the composition of the hydrothermal component preserved in sediment, as well as the utility of some elements, such as Mn, in reconstructing paleo-hydrothermal sedimentation.

Table of Contents

List of Figures

List of Tables

Acknowledgements

I would like to thank Dr. Laurence Coogan and Dr. Jay Cullen for this research opportunity and all of their support and helpful advice throughout this entire project. I would also like to thank Dr. Jody Spence for his incredible help in the lab with the preparation and ICP-MS analysis of my samples. Many thanks to Dr. Patrick Rafter at the University of California Irvine for doing the radiocarbon analysis on the basal section of the sediment core, and Maureen Soon at the University of British Columbia for doing the carbon, nitrogen, and sulfur analyses on the sediment samples. I would also like to thank the staff at Oceans Network Canada for their help in the deployment and collection of the sediment traps and sediment core at the Main Endeavour Field. Finally, a big thank you to my friends and family for their unwavering support during my degree.

1 Introduction

1.1 Hydrothermal Vents at Mid-Ocean Ridges

Hydrothermal systems are found in the ocean along plate boundaries where there Is a link between magmatism, seismicity, and high temperature venting (Hannington et al., 2011). Hydrothermal vents are found predominantly along the global mid-ocean ridge crest that extends 64,000 km, in back arc basins, along volcanic arcs, and intraplate volcanoes, where >300 sites of hydrothermal venting have been discovered (Figure 1.1; Hannington et al., 2011). The magmatic budget of each setting is closely linked to the degree of hydrothermal activity that occurs, indicative of the relationship between spreading rates and the occurrence of hydrothermal vents on mid-ocean ridges.

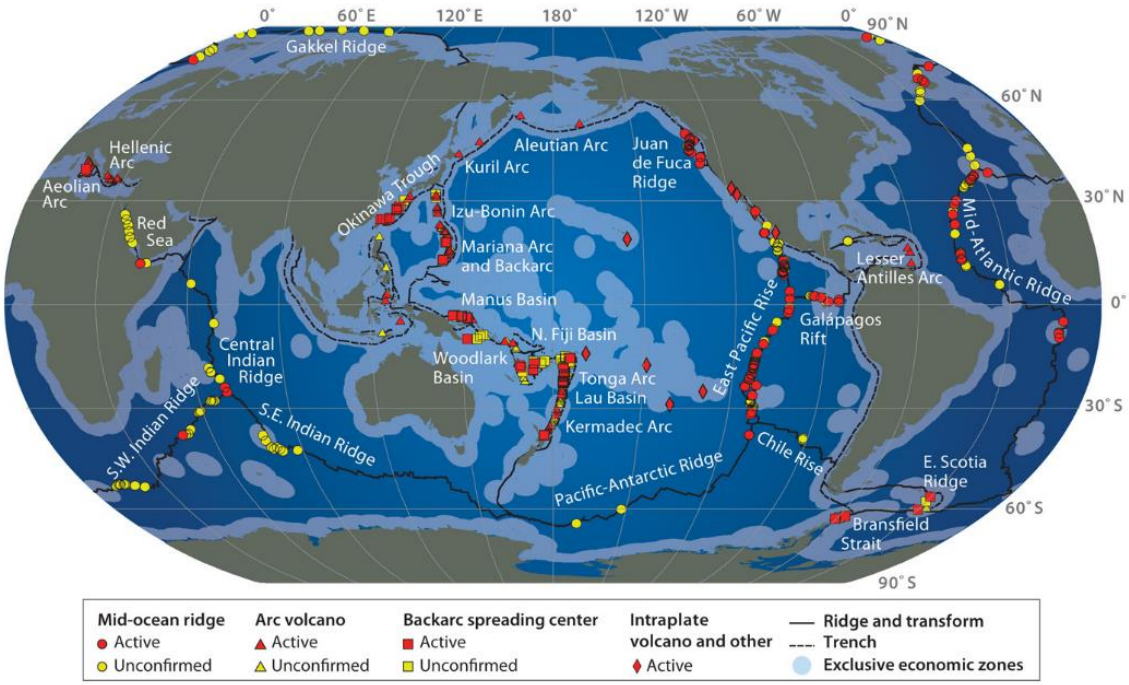

Figure 1.1 Global distribution of seafloor hydrothermal systems (Hannington et al., 2011)

1.2 Hydrothermal Circulation

Hydrothermal venting at mid-ocean ridges occurs when seawater percolates downward through fractures in the ocean crust and is heated by the underlying magma body (German and Seyfried, 2013). Seawater circulates downwards into the crust following regions of high permeability due to spreading processes (e.g., dike margins, normal faults, cooling fractures, etc.). As seawater circulates downward, and temperatures exceed 400°C, it is chemically altered through reactions with the host rock as it circulates deeply through the crust. When the fluid reaches a high temperature, they become buoyant, continually reacting with surrounding rock as they rise through cracks and fissures back toward the seafloor, and are expelled into the

water column (Figure 1.2; German and Seyfried, 2013). The chemical properties of the hydrothermal fluid are dependent on temperature, pressure and the geology of the system which control the water-rock reactions (German and Seyfried, 2013).

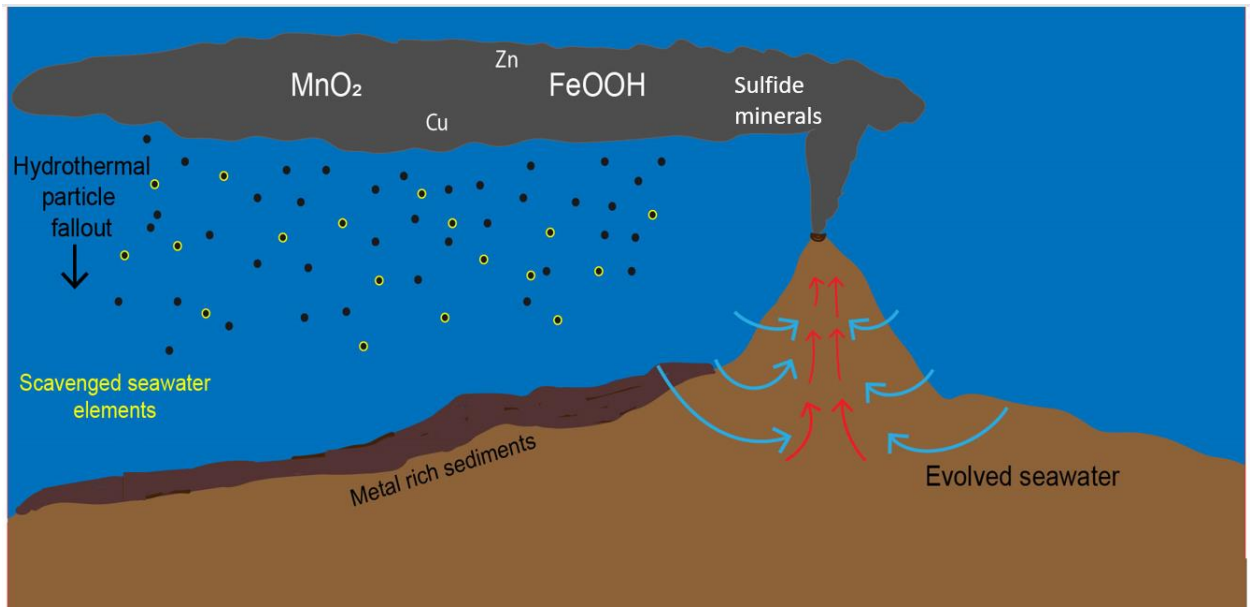

Figure 1.2 Schematic of hydrothermal particulate fallout from the hydrothermal plume

1.2.1 Water-Rock reactions

Chemical reactions between heated seawater and the basaltic crust result in a hydrothermal fluid with a distinct composition compared to seawater. As temperatures reach ~150°C, anhydrite ($CaSO_4$) precipitates which results in a near complete depletion of Ca and about one-third of the sulfate in the fluid (Bischoff and Seyfried, 1978). Further heating results in the fixation of seawater Mg in the crust as Mg^{2+} and OH^- combine to form a component of smectite at temperatures less than 200°C and chlorite at temperatures higher than 200°C (Alt, 1995), as well at high temperatures a magnesium hydroxide sulfate hydrate mineral may precipitate from seawater (Janecky and Seyfried, 1983). The formation of magnesium hydrate minerals (e.g., chlorite and amphibole) by the reaction: $Mg^{2+} + 2H_2O = Mg(OH)_2 + 2H^+$ generates significant acidity, and the resulting pH of the fluid is lower than that of seawater (pH 8.1), typically between 3 and 4 (Janecky and Seyfried, 1983; Hannington et al., 2005).

Continuously, as water circulates through the rock and as temperatures increase to 350-400°C, the composition of the hydrothermal fluid is modified (Alt, 1995). In the high temperature zone, water-rock reactions alter the composition of the basaltic dikes through dissolution and alteration of ferromagnesian minerals, such as olivine and pyroxene, and abundant plagioclase (Alt, 1995). The water-rock reactions result in element depletion in the basalt, and the resulting fluid is enriched in Ca, K, Si, Fe, and Mn, these elements are the “major components” of hydrothermal fluids, along with Na and Cl (German and Seyfried, 2013). Base metals such as Cu, Zn, and Pb are also leached from the rocks during the water-rock reactions,

and due to their mobility in high temperature, acidic environments, they are added to the hydrothermal fluids (German and Seyfried, 2013).

The chemistry of each individual vent varies, though some similarities in the chemical characteristics are observed. Hydrothermal vent fluids are enriched in Fe and Mn, with concentrations 2-3 orders of magnitude higher than the concentration of the ambient water column (German and Seyfried, 2013). Through fluid studies of global vent systems, it has been demonstrated that there is often an enrichment in: SiO_2, H_2S, V, Co, Ni, Cu, Zn, As, Se, Al, Ag, Cd, Sb, Cs, B, W, Au, Tl, Pb, and the REEs relative to seawater, and a depletion in SO_4, Mg, Mo, U relative to seawater due to their solubility (Figure 1.3; German and Seyfried, 2013), though trace metal concentrations vary significantly between vent fields. Specifically on the Juan de Fuca Ridge, enriched basalt (E-MORB) is common, and due to this the hydrothermal fluids are enriched in trace metals incompatible in hydrothermal fluids, such as Ba, Cs, Rb, Th, U, K, and Light Rare Earth Elements (LREE) (Hannington et al., 2005).

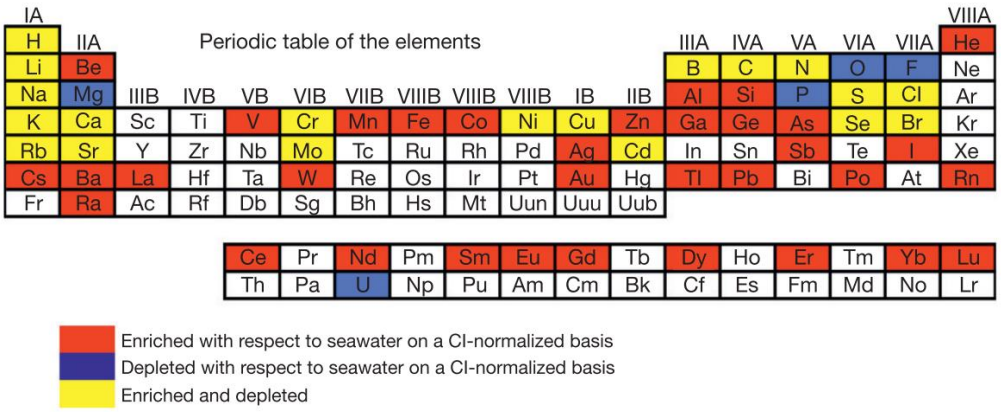

Figure 1.3 Periodic table of elements that are generally enriched in hydrothermal vent fluids relative to seawater (red), depleted (blue) and elements that that have been determined to be both enriched and depleted in different hydrothermal systems (yellow). (Source: German and Seyfried, 2013)

1.3 Hydrothermal Plume Processes

As fluids are heated to a high temperature in the reaction zone, they become buoyant and rise back to the seafloor, where they are expelled into the water column through a hydrothermal vent chimney as a buoyant plume of hot, acidic, and chemically altered fluid. Hydrothermal chimneys are composed of an anhydrite shell, due to the rapid mixing of calcium-rich vent water and sulfate-rich seawater, then metal sulfides as the chimney walls become thicker and are less impacted by mixing with seawater (Von Damm, 1990). In high temperature (>250°C) vent fields, chalcopyrite ($CuFeS_2$) precipitates first as the high temperature sulfide in the interior walls of hydrothermal chimneys, followed by pyrite and sphalerite (Haymon, 1983).

When fluids first interact with seawater, this stage is called the “buoyant plume”, where the hot, acidic, metal-rich hydrothermal fluid is more buoyant than seawater. The buoyant

plume rises and mixes with cold and dense seawater, which results in the progressive dilution of the plume both vertically and laterally. The hydrothermal plume will continue to rise vertically until it reaches a height of neutral buoyancy (the "neutrally buoyant plume"). At this height, the hydrothermal effluent can disperse laterally thousands of kilometers away from the ridge axis (German and Seyfried, 2013). The height of neutral buoyancy is a complex relationship between the physical properties of the hydrothermal fluids (i.e. temperature, salinity, etc.) and the ambient water column (Speer and Helfrich, 1996)

1.4 Formation of Hydrothermal Particulate Material

As hydrothermal fluid enters the ocean, there is rapid mixing between high temperature, Fe and sulfide rich fluids, and the cool, oxidizing ambient seawater endmembers. his mixing process drives precipitation and redox reactions, and results in the rapid precipitation of sulfides (e.g. pyrite, chalcopyrite, and sphalerite) and oxyhydroxides (Rudnicki and Elderfield, 1993).

Rapid precipitation of Fe-sulfides occurs nearly instantaneously within the buoyant plume, where up to 50% of Fe in the buoyant plume may be removed through the precipitation of Fe-sulfides (Rudnicki and Elderfield, 1993). The rapid sulfide precipitation in the buoyant plume occurs predominantly through the FeS-H_2S pathway (Eq. 1.1) as dictated by ambient pH, reactant concentrations, and reaction kinetics (Findlay et al., 2019). The primary factors controlling sulfide formation are the concentration of Fe in the hydrothermal endmember, which can vary widely globally (1 to >1000 mM), and the concentration of H_2S, which varies between 1-10 mM (Von Damm, 1990). The rate of pyrite formation decreases with decreasing H_2S concentration, temperatures lower than 125°C, and pH approaching that of seawater; this confines most of the sulfide precipitation within the buoyant plume (Findlay et al., 2019). On the Juan de Fuca Ridge, pyrite and pyrrhotite ($Fe_{1-x}S$, where x varies from 0-0.125) coexist in the black smoker chimney walls and the rising plume fluids, and are the primary sulfide minerals precipitated from hydrothermal fluids (Feely, 1987; Feely et al., 1994; Findlay et al., 2019). Additionally, in plume studies on the Mid-Atlantic Ridge (e.g., Waeles et al., 2017) and on the Juan de Fuca Ridge (e.g., Feely, 1987), Zn and Cu are predominantly found in Cu- and Zn-bearing sulfides, and do not persist as dissolved species. The early precipitation of Fe before vent fluid is expelled or in the very early buoyant plume may be limited to removal through co-precipitation and inclusion of Fe in Cu- and Zn-bearing minerals (e.g. chalcopyrite, sphalerite), rather than the rapid precipitation of pyrite (Waeles et al., 2017).

$$\mathrm{FeS} + \mathrm{H_2S} \rightarrow \mathrm{FeS_2} + \mathrm{H_2} \qquad (\mathrm{Eq.}\ 1.1)$$

Before fluids are expelled from the hydrothermal vents, Fe and Mn are present in their reduced, dissolved form (Fe(II) and Mn(II)) and after mixing with seawater these are oxidized to Fe(III) and Mn(III/IV) (German and Seyfried, 2013). After rapid precipitation of hydrothermal sulfides, any remaining dissolved Fe in the plume undergoes oxidative precipitation forming Fe-oxyhydroxides (Mottl and McConachy, 1990; Rudnicki and Elderfield, 1993). Fe(III) ions are very

insoluble in oxygenated, circumneutral pH ambient seawater and rapidly form Fe(III)-oxyhydroxides, that aggregate and coagulate into larger particles (Klar et al., 2017). The fundamental control on the formation of Fe(III)-oxyhydroxides is the rate of oxidation of Fe(II) to Fe(III). This is dependent on deep water chemistry, mainly pH and dissolved O_2 (Field and Sherrell, 2000). The Fe(II) oxidation half life varies significantly geographically, from 2.1 minutes at the TAG hydrothermal field at the Mid-Atlantic Ridge to 6.5 hours on the Juan de Fuca Ridge in the Northeast Pacific (Figure 1.4; Field and Sherrell, 2000). Inter-basin variation in Fe-oxidation rates is due to the chemical composition of the ambient deep water, this is due to the thermohaline circulation of the ocean, in which biogeochemical cycling of carbon and oxygen causes the pH and O_2 to decrease in the deep ocean along the flow path from the Atlantic to the Indian to the Pacific Ocean (Field and Sherrell, 2000). The long oxidative half life in the Northeast Pacific Ocean allows Fe-oxyhydroxide formation to persist farther from the hydrothermal vent axis in the Northeast Pacific. Fe(III)-oxyhydroxides particles then aggregate and coagulate into larger particles and are removed from the dissolved Fe fraction and from buoyant plume through gravitational settling (Field and Sherrell, 2000; Klar et al., 2017).

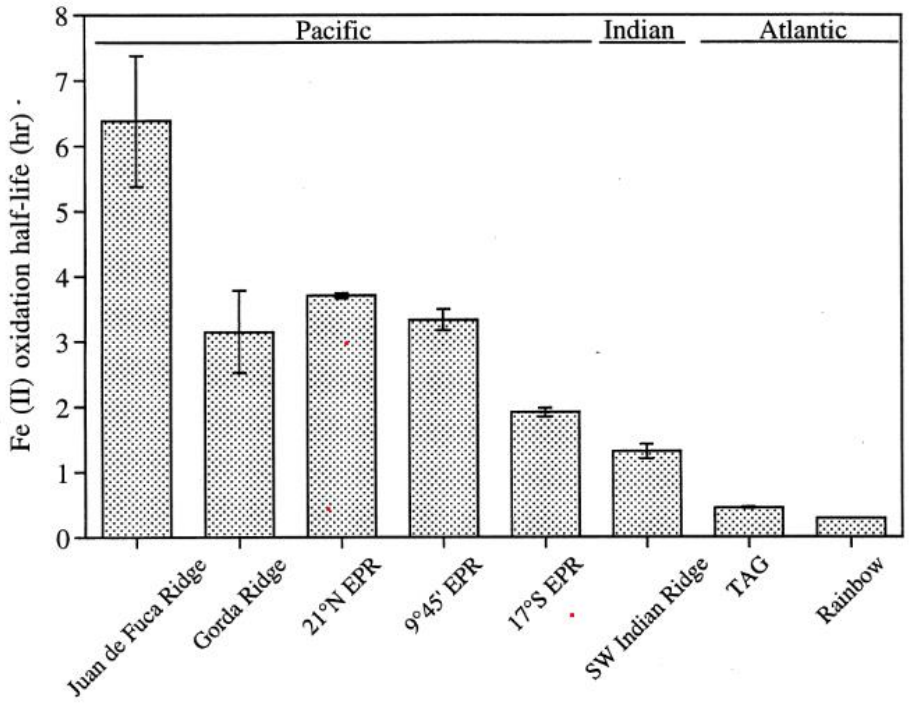

Figure 1.4 Fe (II) oxidation half-lives for ambient deep water conditions at various vent sites in the Pacific, Indian, and Atlantic Ocean on the global ridge system. Error bars are representative of the range of half lives over depths of known black smokers at each vent region (Field and Sherrell, 2000)

Hydrothermal vent fluids are also enriched in Mn(II), and mixing with seawater allows oxidation of Mn(II) within the plume (Cowen et al., 1986). Within the neutrally buoyant plume, Mn(II) is oxidized to Mn(III/IV) and the formation of Mn-oxides. This process, and the cycling of

Mn in hydrothermal systems is often compared to that of Fe, as they are both enriched in hydrothermal fluids and removed from the system by oxidation and particle formation (Von Damm, 1990; German and Seyfried, 2013). The oxidation process of Mn differs from that of Fe as it is microbially mediated, whereas Fe oxidation is predominantly abiotic and orders of magnitude faster than Mn (Field and Sherrell, 2000). Mn uptake into the hydrothermal plume particles is dominated by microbially catalyzed dissolved Mn(II) oxidation to Mn(III/IV) (Cowen et al., 1986; Fitzsimmons et al., 2017; Lee et al., 2021) that would otherwise be kinetically inhibited, and has been shown to form Mn-oxide coatings on bacterial cells (Cowen et al., 1986). Once hydrothermal Mn is oxidized and Mn-oxide particles have formed, they eventually sink to the seafloor, while scavenging other trace elements (German and Seyfried, 2013).

1.4.1 Scavenging by Hydrothermal Particles

The vent derived particles (Fe-oxyhydroxides, Mn-oxides and sulfides) become a sink for the micronutrient P, and trace elements V, Cr, As, Y, Co, Mo, Pb, REEs, U, and Th. Smaller particles that do not sink remain entrained in the plume that can be detected thousands of kilometers away from the ridge axis (German and Seyfried, 2013). Trace elements are removed from the water column by adsorption onto suspended particle surfaces (Figure 1.5) such as plume derived sulfides, colloidal ferrihydrite ($Fe(OH)_3$; Fe-oxyhydroxide), and poorly crystalline Mn oxides (German et al., 1997; Dunk and Mills, 2006; Lee et al., 2021). These minerals are highly efficient sinks for dissolved seawater trace elements due to their abundance, high specific surface area, and their residence time in the hydrothermal plume (German et al., 1997; Hayes et al., 2015). Scavenging processes occur rapidly during the formation of hydrothermal particles close to the ridge axis.

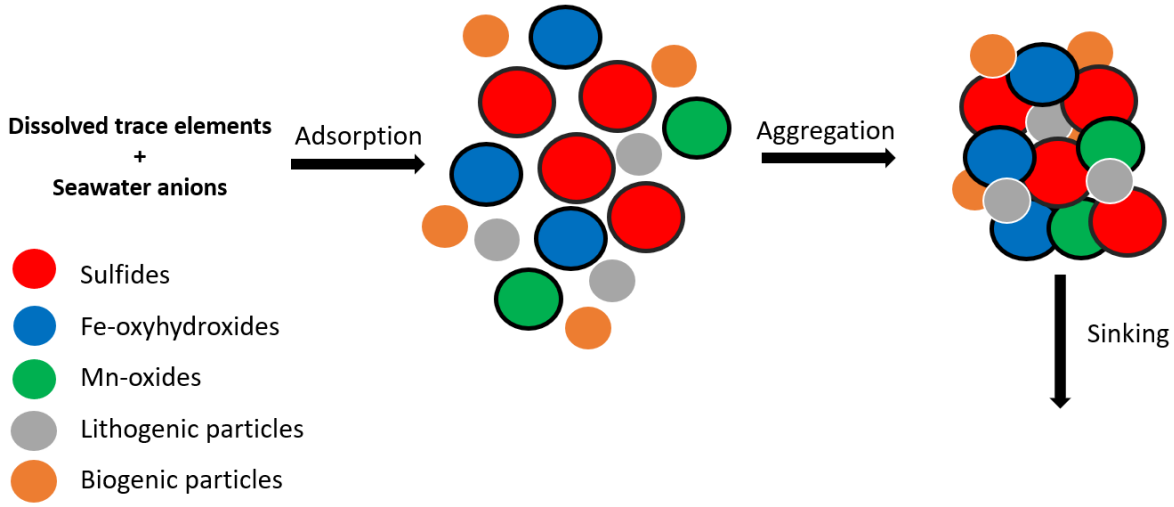

Figure 1.5 Idealized scavenging processes of hydrothermal particles occurring in hydrothermal plumes. Thick black outline indicative of dissolved trace elements and seawater anions being scavenged by hydrothermal particles (Fe-oxyhydroxides, sulfides, and Mn-oxides). Based on Hayes et al. (2015)

1.5 Hydrothermal Sedimentation

The formation of particles within the hydrothermal plume occurs quickly as the plume enters the ocean. With distance from the vent site, the plume becomes progressively more diluted due to mixing with seawater and the progressive fallout of hydrothermal particulate matter. The deposition of plume particles on the seafloor acts as an important removal mechanism in the geochemical cycling of many trace elements in the ocean. The particle settling dynamics control the accumulation rates of the hydrothermally derived components of the sediments as well as the associated scavenged elements. The processes that control the deposition of the particles include physical processes such as currents, turbulence, and the height of the neutrally buoyant plume. The removal of hydrothermally derived elements from the neutrally buoyant plume in the near venting region occurs due to aggregative removal of these elements onto biogenic and/or lithogenic particles that settle from the water column above (Fitzsimmons et al., 2017) as well as aggregation of hydrothermally derived plume particles that increases the particle size and density, which leads to increased removal near the vents.

Up until recently, the hydrothermal contribution to the oceanic dissolved Fe inventory was thought to be negligible as the mineral precipitates were expected to settle rapidly to the seafloor (e.g. Bennett et al., 2009). However, recent studies demonstrate that Fe-bearing sulfide nano-particles are preserved within the plume (Yücel et al., 2011) and observed up to 4,000 km away from active venting (Fitzsimmons et al., 2017). The persistence of Fe in the hydrothermal plume is due to both nano-particulate Fe-sulfides, as well as Fe that is stabilized and complexed by organic ligands allowing Fe to remain in the dissolved phase great distances from sites of active venting (Bennett et al., 2009; Toner et al., 2009; Fitzsimmons et al., 2017). Fitzsimmons et al. (2017) observed hydrothermal particulate Fe in the plume 100-200 km away from active venting as Fe(III)-oxyhydroxide minerals embedded in a matrix of organic carbon. Dissolved Fe and Mn from a hydrothermal source was detected 4,000 km from the vent source as particulate Fe(III)-oxyhydroxides and organically complexed iron phases (Fitzsimmons et al., 2017). The aggregation with organic carbon results in an offset of the high specific gravity of Fe minerals with the low specific gravity of organic matter, allowing the more dense Fe-oxyhydroxide particles to persist for longer distances from active venting (Fitzsimmons et al., 2017). With this persistence in the neutrally buoyant plume, high concentrations of hydrothermally derived elements are observed in the near vent region, which decrease concentrations with distance from the vents due to progressive plume dilution from mixing with seawater and particle fallout into the underlying sediments.

1.6 Study Area

1.6.1 Geologic Setting: Juan de Fuca Ridge

The Juan de Fuca Ridge is a 500 km long ridge located approximately 300 km off the Coast of Vancouver Island (Figure 1.6). The Juan de Fuca plate is a remnant of the Farallon

plate, which has largely been subducted beneath the North American Plate. The Juan de Fuca ridge separates the Pacific plate from Juan de Fuca plate, and has an intermediate spreading rate mid-ocean ridge, with a half spreading rate of 3 cm year^{-1} (Kelley et al., 2012).

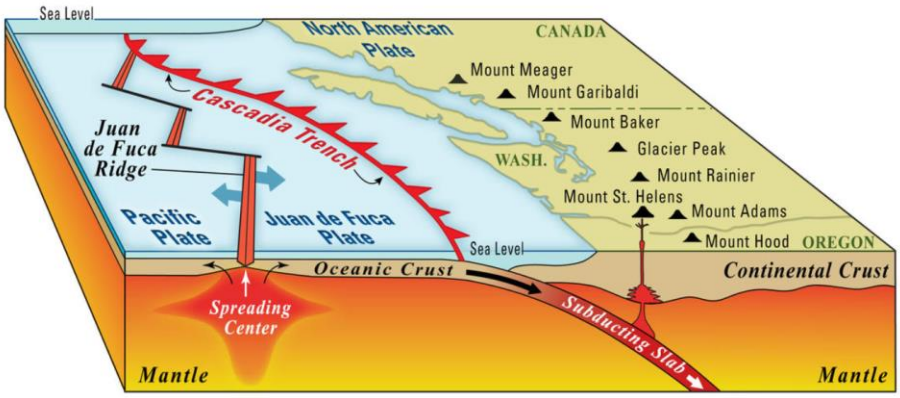

Figure 1.6 Geologic setting of the Eastern Pacific Ocean. Source: USGS

1.6.2 Endeavour Segment, Juan de Fuca Ridge

The Endeavour Segment (47°N, 129°W) of the Juan de Fuca Ridge is 90 km long; it is one of seven segments that comprise the Juan De Fuca Ridge. These segments from North to South are: Middle Valley, West Valley, Endeavour, Northern Symmetrical, Axial, Vance, and Cleft (Kelley et al., 2012, Clague et al., 2014; Figure 1.6). The central rift of the Endeavour Segment is a 25 km long volcanic high that is divided by a 0.5-1 km wide, 75-200 m deep, steep-sided axial rift (Kelley et al., 2012). Within this central rift, there are five major hydrothermal vent fields, from North to South: Sasquatch, Salty Dawg, High Rise, Main Endeavour, and Mothra (Figure 1.7). This region is one of the most active hydrothermal areas known on the global mid-ocean ridge system, with 572 identified chimneys in the central 14 km of the segment, with 47 active vents (Kelley et al., 2012; Clague et al., 2020). The study site for this project is the Main Endeavour segment of the ridge. The Main Endeavour field has 53 mapped chimneys (Clague et al., 2020). The large number of inactive chimneys in the Endeavour segment, suggest that hydrothermal activity has persisted for at least 2,300 years (Jamieson et al., 2013; Clague et al., 2014a).

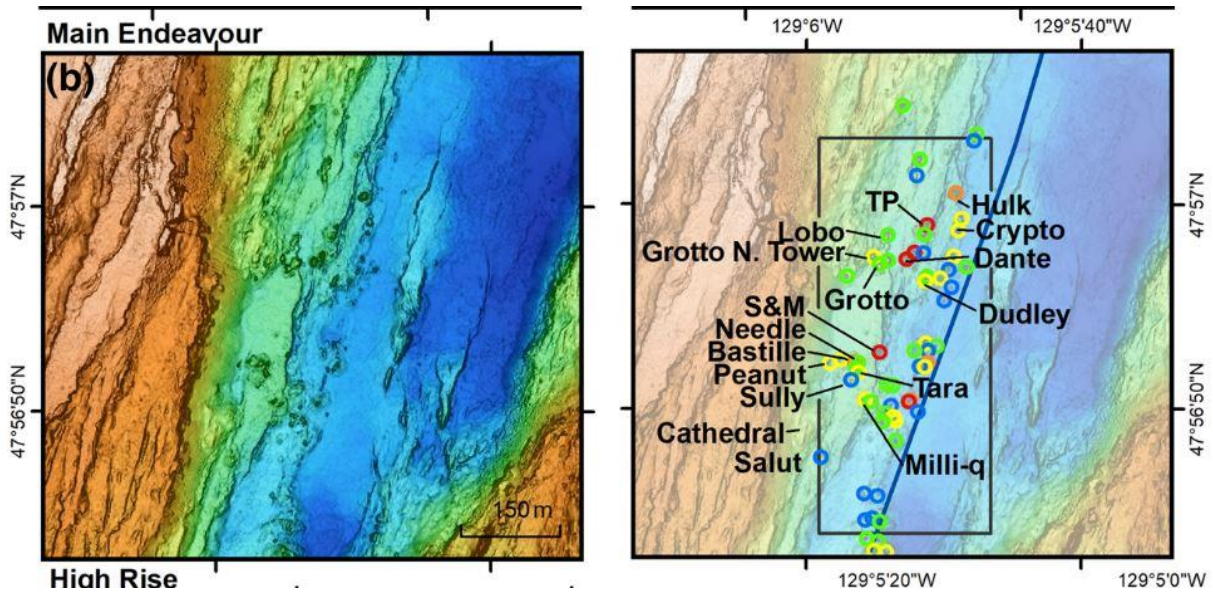

Figure 1.7 Vent distribution on the Endeavour Segment of the Juan de Fuca Ridge. Coloured circles represent chimney locations, with colours representing height of the chimneys as reported in Clague et al., 2020.

The outer flanks of the ridge are bounded to the east and west by low-relief, plains. Based on a 2001-2005 University of Washington (UW) and UW-Monterey Bay Research Aquarium Institute (MBARI) survey of the outer flanks, the eastern flanks have extensive sheet flows and collapse basins with 10-15 cm of sediment, and to the east the ridge flanks are capped by ~1 m of sediment (Kelley et al., 2012). Sediment accumulation rates on the Juan de Fuca Ridge were estimated based on the length of sediment cores and the age at the bottom of the core using radiocarbon dating of planktic foraminifera by Clague et al. (2014). Sediment accumulation rates on lobate flows were determined to range from 0.09-1.25 mm year^{-1} (Clague et al., 2014a).

1.6.3 Endeavour Hydrothermal Plume

The physicochemical characteristics of the hydrothermal plume on the Endeavour Segment of the Juan de Fuca Ridge is well documented and has been the subject of multiple studies over the past 40 years (e.g. Baker and Massoth, 1987; Feely et al., 1992, 1994; Thomson et al., 2005). The temperature of the black smoker vent fluids coming immediately out of the plume have been measured between 300-380°C (Baker and Massoth, 1987; Von Damm and Bischoff, 1987; Feely et al., 1992). An average temperature anomaly, as determined by CTD surveys of the hydrothermal plume of 0.043°C is observed in the area (Baker and Massoth, 1987; Burd and Thomson, 1994; Coogan et al., 2017). Temperature anomalies are quite useful to map the distribution of the hydrothermal plume and are calculated from Equation 1.2:

$$\Delta\theta = \theta - \mathrm{k}\sigma_\theta - b \qquad (Eq.\,1.2)$$

Where θ is potential temperature, σ_θ is potential density, and k and b are the slope and intercept of the trend of θ as a function of σ_θ in hydrothermally unaffected water immediately

above the neutrally buoyant plume (Baker, 1994). The average vent fluid temperature and the water column temperature anomaly can be used to calculate a dilution factor of the hydrothermal fluid to seawater of 8000 (Coogan et al., 2017).

The hydrothermal plume on the Endeavour Segment is made up from emissions from individual vents within the Main Endeavour Vent field that rise and combine into a single ~200 m thick plume that is moving away from the source (Baker and Massoth, 1987). The orientation of flow of the neutrally buoyant plume is to the southwest (Baker and Massoth, 1987). The near steady background current is constrained within the rift-valley and results, in part, to turbulent entrainment by the buoyant plumes rising from vent fields (Figure 1.8; Thomson et al., 2003). The current reverses ~10% of the time, which appears to be linked to strong bursts of southwesterly flow in the overlying water column (Thomson et al., 2003).

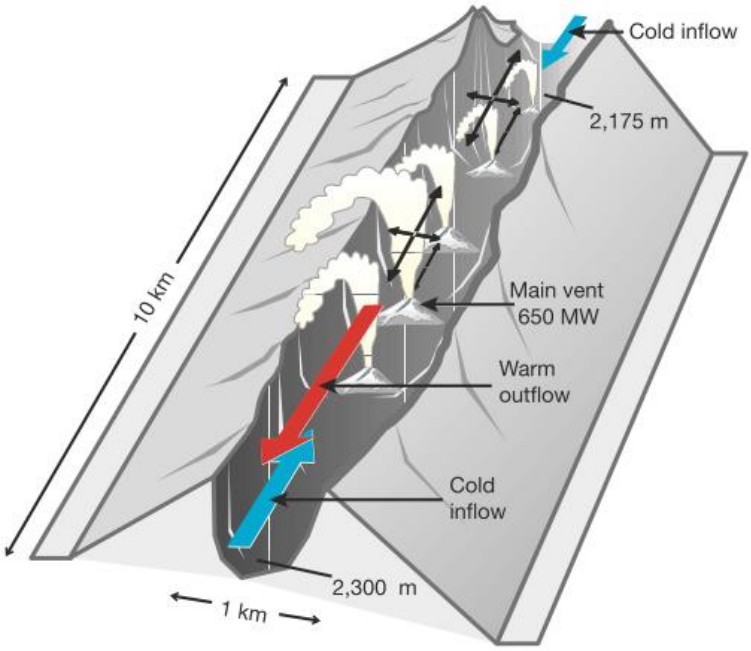

Figure 1.8 Schematic of water flow within the Endeavour Ridge (Thomson et al., 2003).

1.6.4 Chemistry of the Endeavour Hydrothermal plume and plume particles

The chemical composition of the Endeavour hydrothermal fluid has been studied since the 1980's. Early studies of the plume particulates from the buoyant plume on the southern Juan de Fuca Ridge found predominantly sphalerite (ZnS), wurtzite (ZnS), and pyrite (FeS_2) (Feely, 1987). Pyrite was found as inclusions within sphalerite as well as discrete fine-grained particles (Feely, 1987). Pyrrhotite ($Fe_{1-x}S$) and chalcopyrite are minor components of the vent particles and are also found as fine-grained discrete particles and intergrown with sphalerite. Other minor mineralogical components of the hydrothermal particulates include barite, isocubanite (cubic $CuFeS_2$), and elemental sulfur (Feely, 1987). The major chemical components of the Endeavour hydrothermal plume in decreasing order of abundance are: iron, sulfur,

copper, calcium, silicon and zinc; Table 1.1 shows the weight percent of dry particulate matter concentration in the Endeavour plume as reported in (Feely, 1987).

Table 1-1 Composition of dry black smoker particulate matter from the Endeavour hydrothermal plume, reported in weight percent. Samples collected on Alvin dive 1418, using titanium samplers (Feely, 1987)

Sample ID	Al (wt%)	Si (wt%)	S (wt%)	Ca (wt%)	Fe (wt%)	Cu (wt%)	Zn (wt%)
Dive 1418 - 3	0.34	1.7	31.7	0.24	31.2	13	1.56
Dive 1418 - 7	1.06	3.9	32.8	3.54	25	7.39	2.39
Dive 1418 - 9	0.69	2.1	32.9	3.14	31.2	5.73	3.16

1.6.5 Geochemistry of Endeavour sediments

The chemical composition of the sediments is controlled by the composition of the plume, plume dilution and particle fallout moving away from active hydrothermal venting. There have only been a few studies of hydrothermal sediments at the Endeavour Segment prior to this study.

Dymond and Roth (1988) were the first to install sediment traps to analyze the geochemistry of the hydrothermally derived particulate matter at the Main Endeavour Field. A sediment trap was placed directly within the buoyant plume at the MEF, as well as a sediment trap below the neutrally buoyant plume at High Rise for 11 months. From this study, the differences in the flux of hydrothermal material in the near and far field experiments revealed spatial and temporal variation of the hydrothermal plume, with high fluxes in the near field and a sharp decrease with increasing distance from the source (Dymond and Roth, 1988).

Hrischeva and Scott (2007) published the first comprehensive report of the geochemistry, mineralogy, and morphology of the Endeavour sediments through analysis of sediment core and grab samples of near vent and ridge flank (3 km off axis) sediments. They found that the concentrations of Fe, Cu, Zn, Pb, As and Mo decreases rapidly with distance from the vents due to rapid deposition of sulfides near the vents.

Coogan et al. (2017) used a sediment trap emplaced on-axis near the buoyant plume in the Main Endeavour Field and sediment cores from near and far-field locations to determine the geochemistry of the hydrothermal sediments and to understand chemical processes occurring in the hydrothermal plume. It was found that sulfides precipitate early and accumulate rapidly in the sediments near the vents. Using the geochemistry, the proportion of each component (hydrothermal, detrital, biological, and basalt) was separated to determine the spatial variation in the composition of the hydrothermal component. The 2014-2015 sediment trap data from this study is used in this work to expand the time scale of on-axis hydrothermal sedimentation that has been analysed.

1.7 Objectives of This Study

Given that the chemical composition of sediments near the Endeavour Hydrothermal Field (Dymond and Roth, 1988; Hrischeva and Scott, 2007; Coogan et al., 2017) is controlled by the distance from active venting the objectives of this study are to assess:

(1) the spatial variability of the hydrothermal component (e.g., Fe, Cu, Zn and Mn, and associated scavenged elements) of the sediment near the Endeavour ridge using sediment traps emplaced on-axis at the Main Endeavour Field, 3 km off-axis, and 9 km off axis. The concentrations and mass accumulation rates of the hydrothermally derived elements will be used to answer the question "what processes control the chemistry and mass accumulation rates of the hydrothermally derived component of the sediments?".

(2) the temporal variability of the hydrothermal component in the sediments collected from sediment traps on month to year time periods. The variation in the concentration and mass accumulation rate of hydrothermal elements will be used to understand how variable hydrothermal sedimentation is, as well as what processes are controlling this sedimentation.

(3) post-depositional changes that may mask the primary hydrothermal signature preserved in sediment cores over thousand-year time scales. Diagenesis may have an impact on the composition of hydrothermally derived particles over long time scales. The geochemistry of the sediment and pore fluids of a sediment core that represents 6,000 years of sedimentation to the NW of the Main Endeavour Field is used to assess whether post-depositional changes have masked the primary geochemical signature. The hundred to thousand of year time scale changes can also be compared to those preserved across glacial-interglacial time periods.

2 Sample Suite

2.1 Sediment core: sampling and processing

2.1.1 Geographic location and sample collection

A sediment core (H-1581) was collected by Ocean Networks Canada on July 17, 2017, at 16:35 by ROV Hercules roughly 2.8 km West of the High Rise vent field and 2.6 km Northwest of the Main Endeavour Field. The core was taken at a depth of 2360 mbsl (meters below sea level) at the base of the topographic high on the western flank of the ridge (47°57'35.49", -129°7'29.27"; Figure 2.1). After collection, the core was kept frozen until it was processed on shore in the laboratory at the University of Victoria. Unused material was promptly returned to the freezer for archiving.

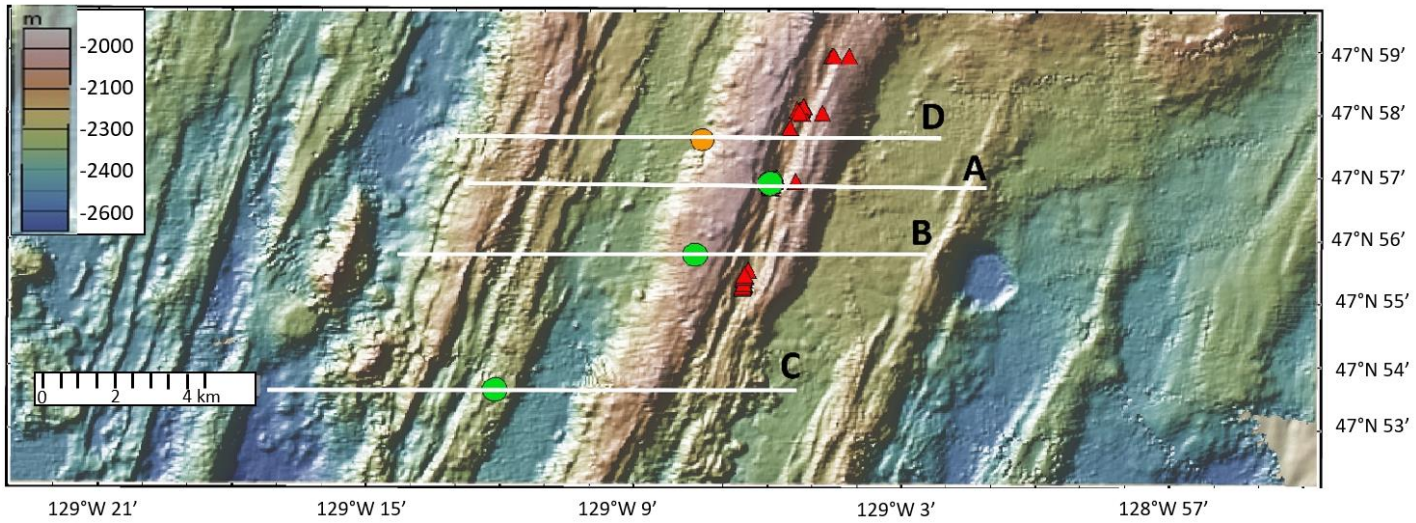

Figure 2.1 Sampling locations of sediment core (orange circle) and sediment traps (green circles) in relation to active vents (red circles) at the Endeavour Hydrothermal Field (vent location data from GeoMapApp, accessed on October 14, 2021). White lines are representative of bathymetry transects shown in Figure 2.2. Transect D (northern-most sample) is representative of the E-W transect intersecting the sediment core sample; Transect A is the on-axis sediment trap, B the 3 km off-axis trap, C the 9 km off-axis trap. Transect utility is to show the positioning of the sediment traps with respect to surrounding bathymetry.

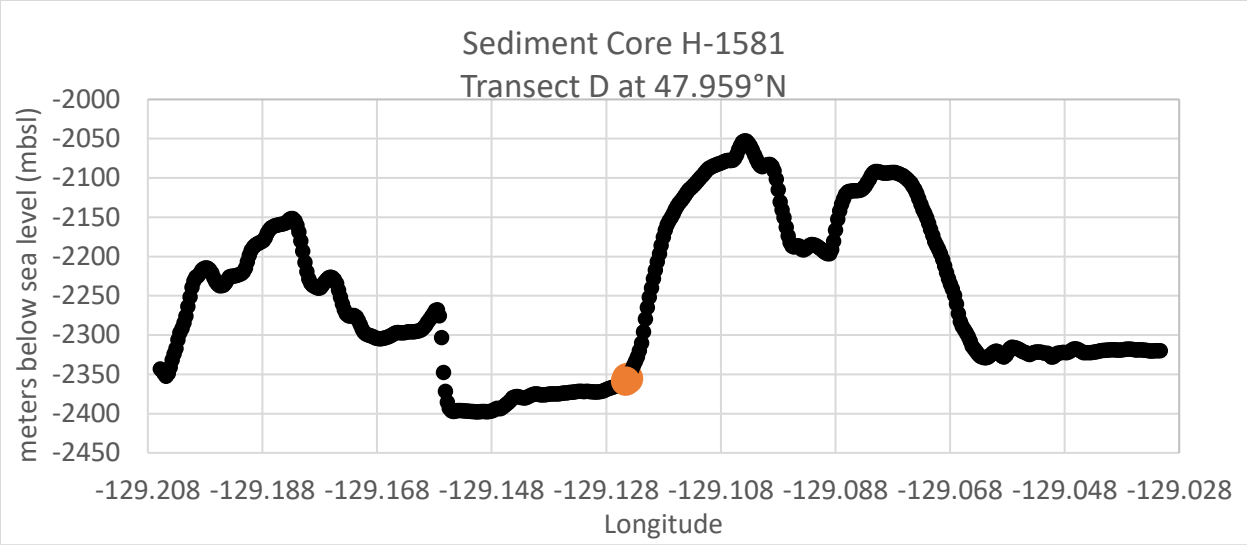

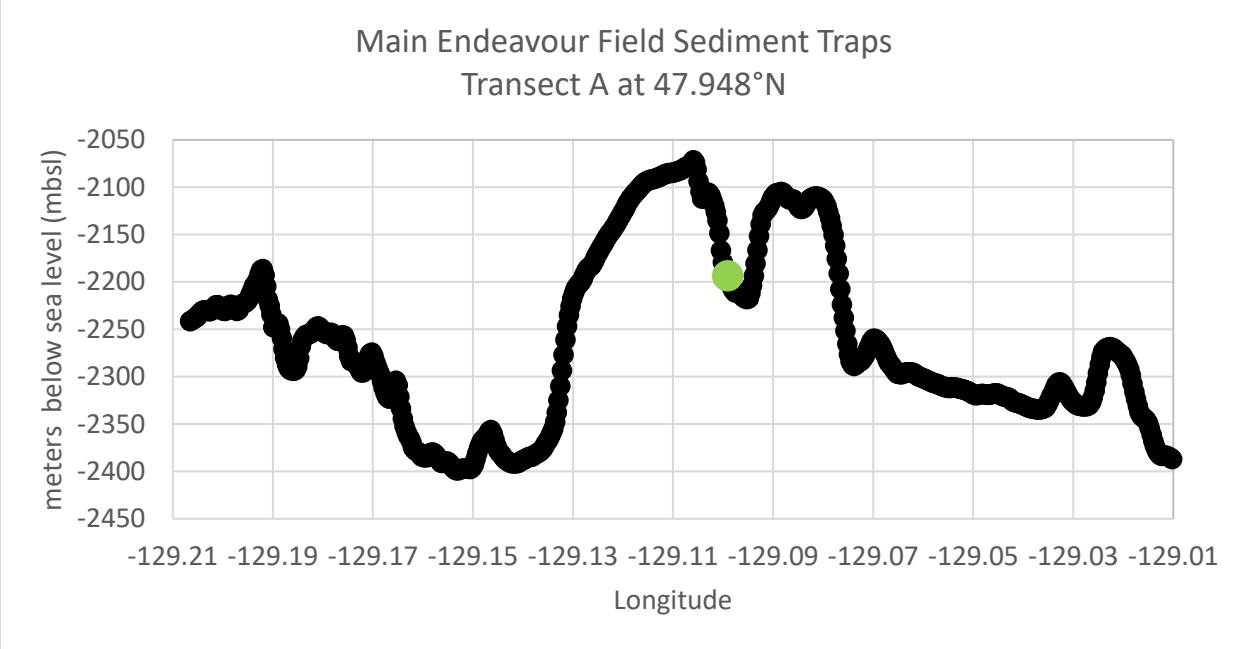

Figure 2.2 Seafloor bathymetry along an east-west transect, from furthest North (sediment core, transect D) to south (Main Endeavour Field sediment trap, transect A; 3 km off axis sediment trap, transect B; 9 km off axis sediment trap, transect C). Bathymetry data from GeoMapApp, downloaded October 14, 2021

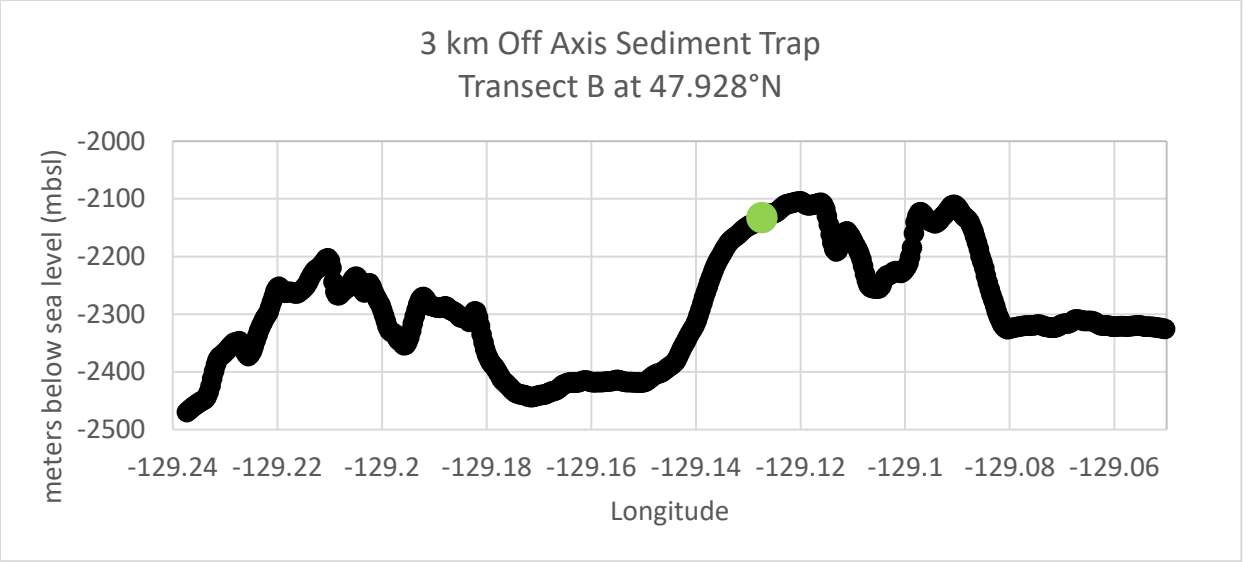

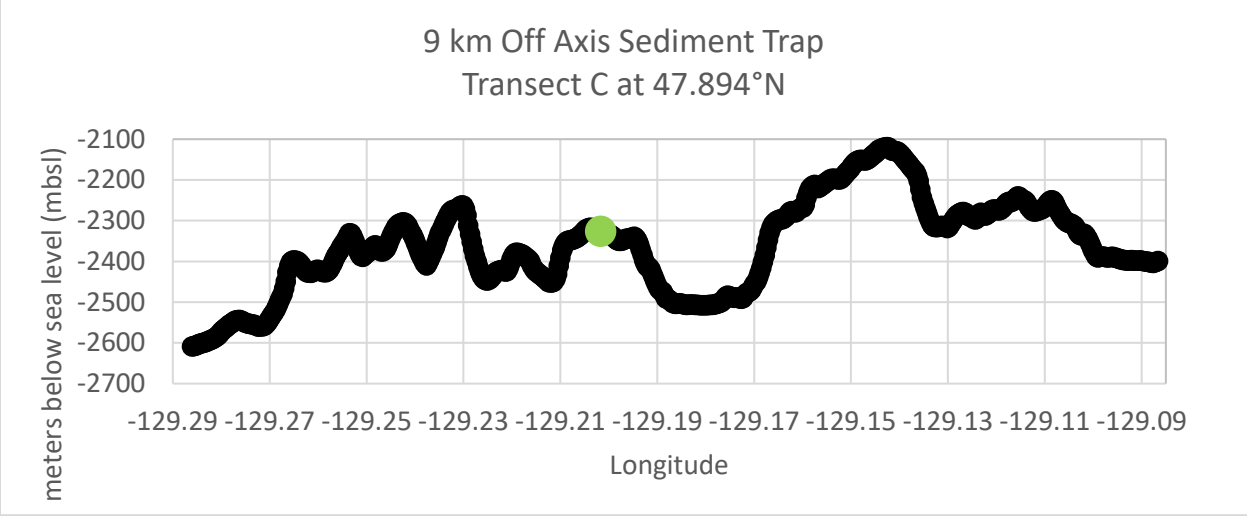

(Continued from previous page) Seafloor bathymetry along an east-west transect, from furthest North (sediment core, transect D) to south (Main Endeavour Field sediment trap, transect A; 3 km off axis sediment trap, transect B; 9 km off axis sediment trap, transect C). Bathymetry data from GeoMapApp, downloaded October 14, 2021

2.1.2 Sediment Core Description

Sediment core H-1581 is 51 cm long and 6.5 cm wide (Figure 2.4). Visual inspection of the

Figure 2.4 (A) Sediment Core H-1581 (B) close up of basal section of sediment core

frozen core showed that the top 6 cm are an oxidized, brown muddy material, which grades into 6-8 cm of lighter, greenish-grey sediment, representing the grey-green boundary generally interpreted as an oxidation front (Lyle, 1983). The rest is a homogeneous dark grey colour (Figure 2.4). The dried sediment is light brown-grey at all depths. The bottom two segments were observed under a binocular microscope before being crushed and is composed of biological material (foraminifera, radiolarians, and diatom tests) and pellet-shaped material (possible organic material), volcanic glass shards, volcanic hair, and fine detrital grains (Figure 2.5)

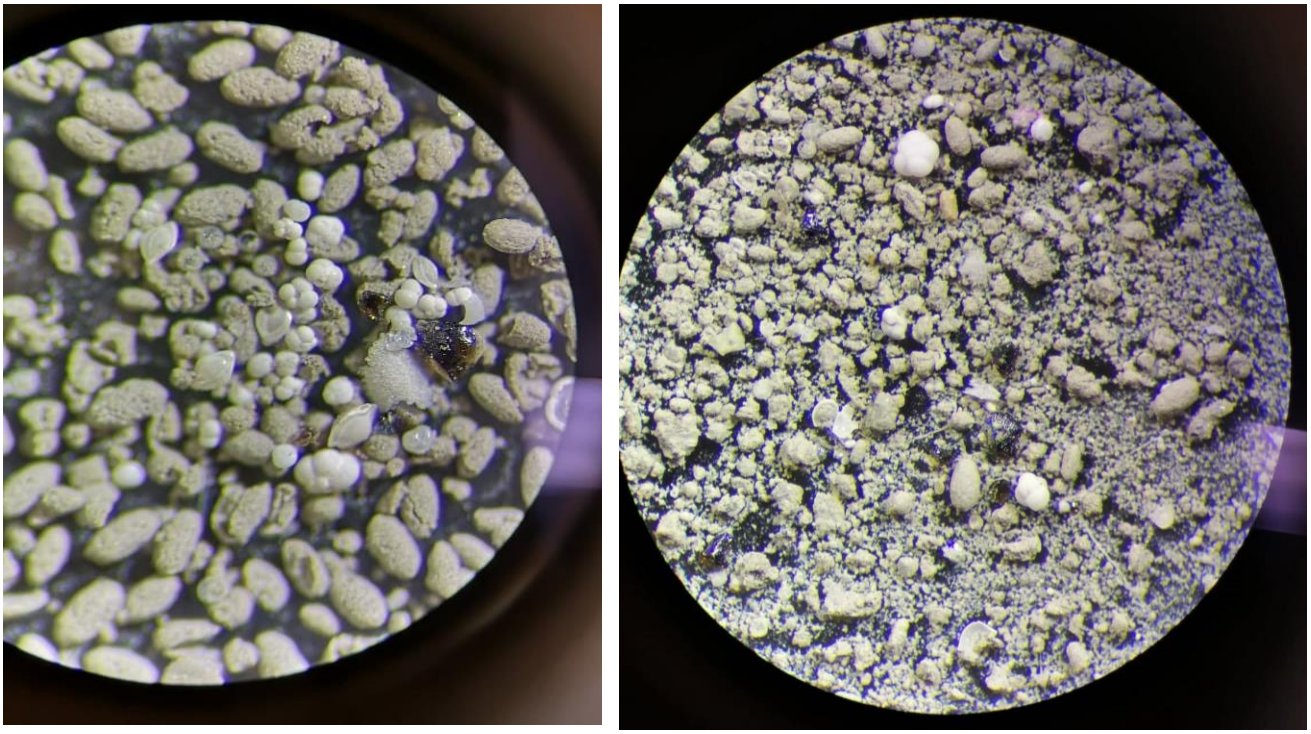

Figure 2.5 125 – 425 µm size fraction showing foraminifera, volcanic shards, elongated pellet shaped material, and fine grained sediment

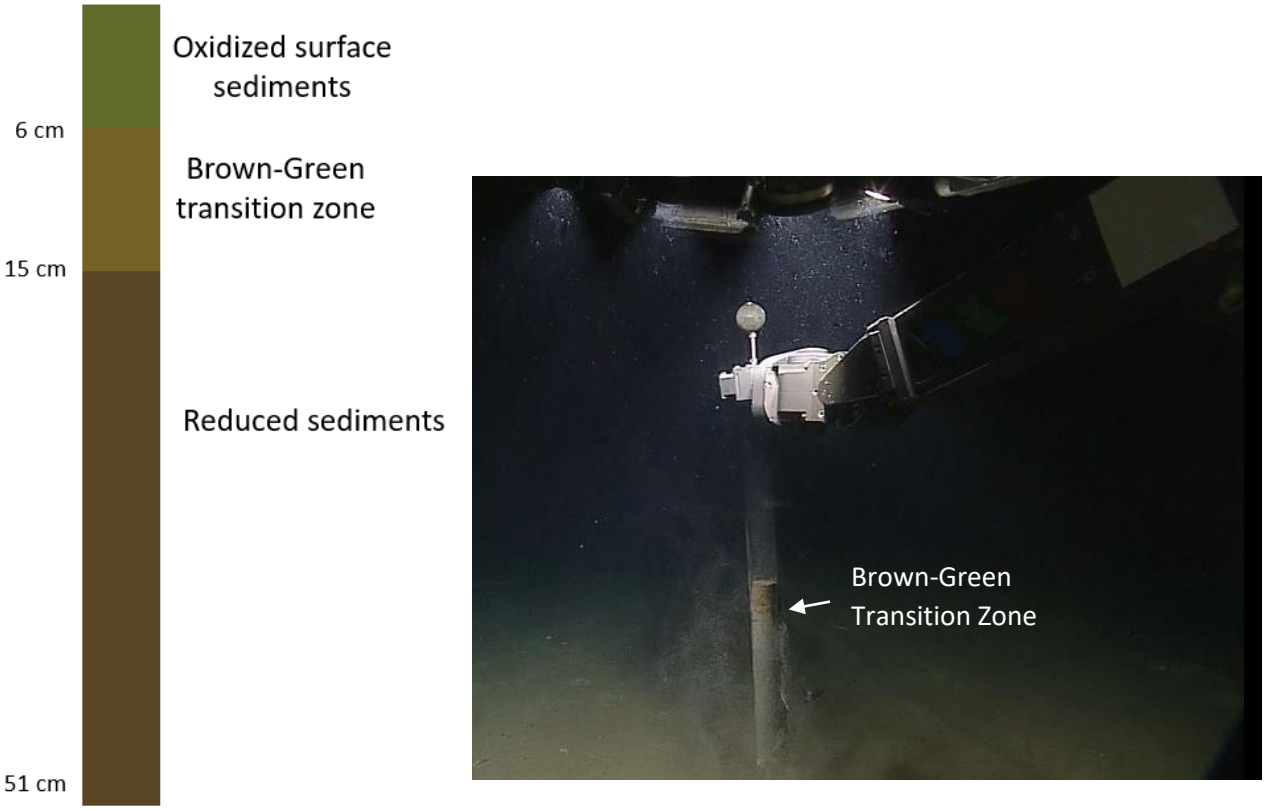

Figure 2.6 (left) schematic of sediment composition zones in sediment core H-1581, (right) capture from collection of sediment core H-1581 (Source: ONC SeaTube; July 17, 2017, 16:54)

2.2 Sediment Traps: collection and processing

2.2.1 Sediment trap deployment and sample collection

A series of sediment traps were placed at the Endeavour Hydrothermal vent field at 3 distances away from the active vents: within the Main Endeavour Field, 3 km southwest of the vent field, and 9 km southwest by Ocean Networks Canada (Figure 2.1, Figure 2.7). The sediment traps are McLane Parflux MK78H-21 which are equipped with 21x 500 mL sampling bottles filled with a 5 wt% NaCl brine with a higher density than seawater to isolate samples in the trap and prevent resuspension of particles (GOFS, 1989). The sediment traps are equipped with a 0.65 m^2 cone to collect sediment into the narrow mouth HDPE sample bottles (Figure 2.8).

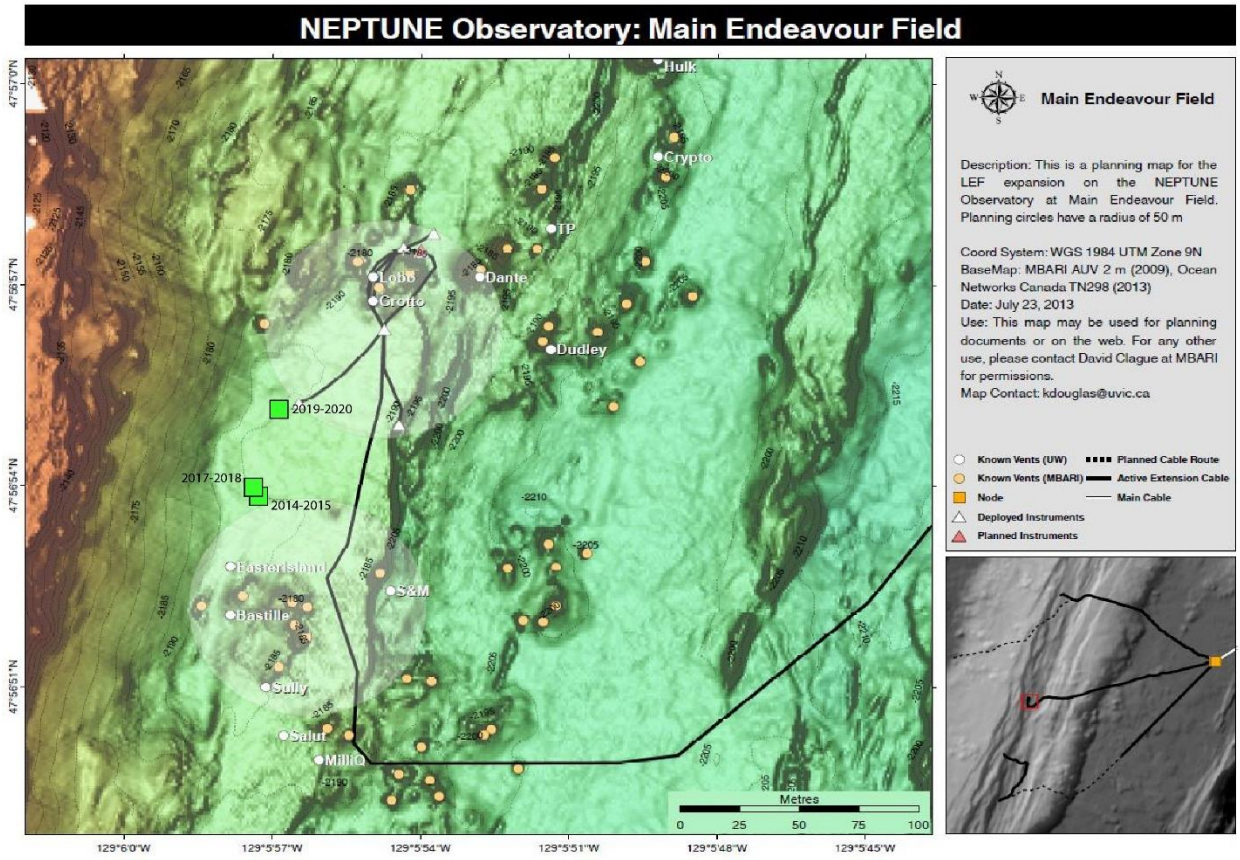

Figure 2.7 Location of MEF On-Axis sediment traps (2014-2015, 2017-2018, 2019-2020) with relation to individual vents in the Main Endeavour Field (Source: Dave Clague, MBARI)

Two on-axis traps were deployed within the Main Endeavour field at separate times to cover the time periods of July 1, 2017 – July 14, 2018 (https://data.oceannetworks.ca/Sites?siteId=1000861) and May 16, 2019 – September 9, 2020 (https://data.oceannetworks.ca/Sites?siteId=1007439). The approximate position of the 2017-2018 on axis trap is 47°56'53.97'N, 129°5'57.37"W, at a depth of approximately 2190 mbsl (depth derived from MBARI AUV bathymetry) on a mooring extending 8 m above the bottom (Figure 2.7)). This trap was to be recovered in 2018 but could only be retrieved on September 9, 2020. The approximate position of the 2019-2020 on axis trap is 47°56'55.12"N, 129°5'56.81"W, at a depth of approximately 2184 m also on an 8 m mooring. The sampling interval for both on axis sediment traps was set at 23 days.

The 3 km off-axis trap (https://data.oceannetworks.ca/Sites?siteId=1013600) was deployed at approximately 47°55'46.3"N, 129°7'38.34"W at a depth of 2115 m, near the top of the ridge on the west flank on a 20 m mooring with the trap mouth approximately 28 m above the seafloor (Figure 2.7) to reduce the chance of collecting resuspended bottom sediment. This trap was located about 3 km SW from the nearest vent in the MEF based on the direction of prevailing bottom currents (Section 1.6.3). Material was collected from September 16, 2019 to February 28, 2020 with a sampling interval of 12 days. The closing mechanism failed after the

collection of sample 14 during rotation 15, therefore the last sample (15) was collected from February 28-September 28, 2020, a collection time of 213 days and the bottle remained open as the trap was transported to the surface and therefore may be contaminated with material collected as it moved upward through the water column.

The 9 km off axis trap (https://data.oceannetworks.ca/Sites?siteId=1013620) was deployed at approximately 47°53’37.64”N, 129°12’6.43”W at a depth of 2320 m, about 9.5 km SW of the Main Endeavour Field using the same deployment method as the 3 km trap. Samples were collected with a fixed sampling interval of 11 days from September 17, 2019 to May 30, 2020 and recovered on September 28, 2020.

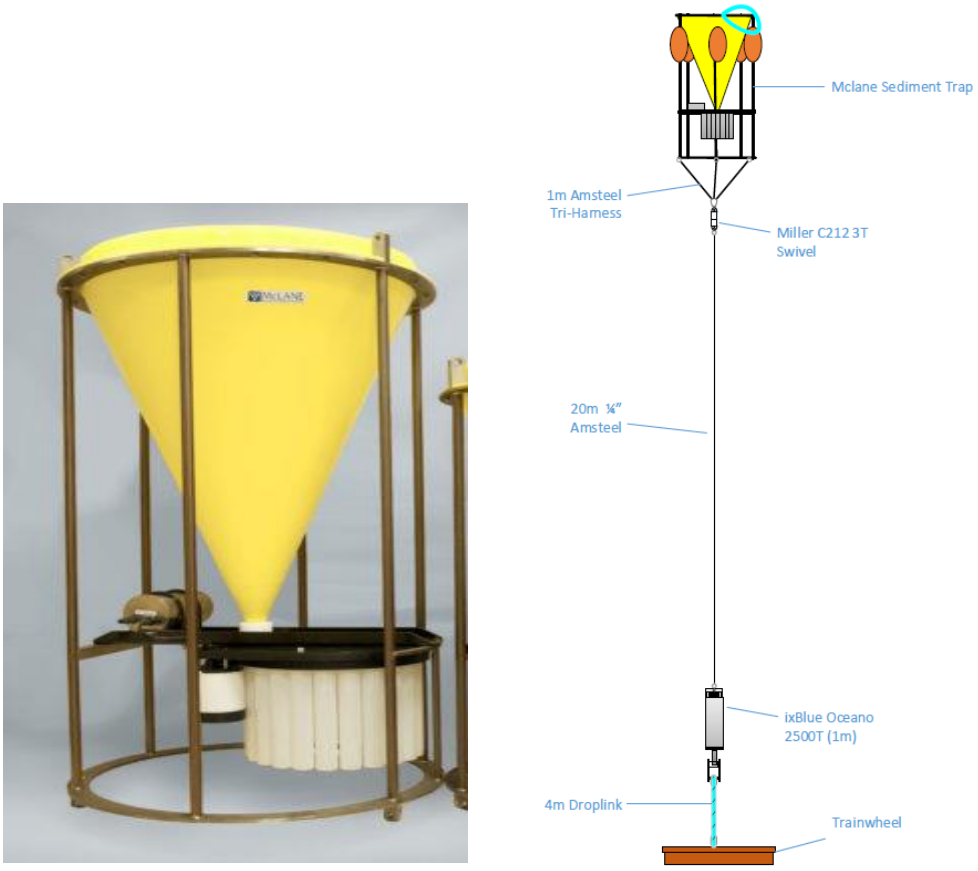

Figure 2.8 (left) McLane Parflux MK78H-21 Sediment trap (https://mclanelabs.com/sediment-traps/) (right) Sediment trap mooring configuration (Steve Mihaly, Ocean Networks Canada)

3 Analytical Methods

3.1 Sample Preparation

3.1.1 Sediment core preparation

The still frozen core was cut into 34, approximately 1.5 cm long, segments using a ceramic (ZrO_2) serrated bladed knife to minimize metal contamination and processing time was kept to a minimum to ensure material did not thaw significantly during handling. Small aliquots of samples, dry mass between 5 and 9 g of material, were separated and transferred to clean 50 mL centrifuge tubes. Where they were left to thaw at room temperature, centrifuged and pore fluid was removed using a rubber free syringe and passed through a 0.2 µm Luer lock filter for dilution and analysis. The remaining unfiltered material was transferred to a clean 15 mL analysis tube and returned to the freezer. The sediment aliquots were then placed in a drying oven, partially covered to avoid contamination, at ~40°C temperature until they were completely dry. They were then crushed using an agate mortar and pestle, weighed using an analytical balance, and transferred into glass storage vials.

3.1.2 Sediment trap sample preparation

To separate the sediment from the brine, samples were filtered in a class 100 fume hood. Before starting sample processing all filtering equipment, tweezers, and 50 mL centrifuge tubes were cleaned using 2 M HNO_3. First, all material was passed through a 1 mm Nitex mesh to remove swimmers (large shells, plankton, tube worm casings, and jelly-like organisms). The residual material was then filtered with 0.2 µm hydrophilic polycarbonate Isopore membrane filters (Millipore Sigma) using a 500 mL Polysulfone Nalgene vacuum filter tower. The filter tower was connected to a vacuum pump using ¼ inch PVC tubing (Figure 3.1). The vacuum pressure used was approximately 35 psi. The material retained in the filter was transferred to a 50 mL centrifuge tube using deionized (DI) water in a squirt bottle. The samples were centrifuged for 40 minutes, and the majority of the water was removed from the material by a combination of pouring and disposable plastic transfer pipettes. Samples were then dried, partially covered by a clean glass beaker in a low temperature drying oven (40-50°C) until completely dried, weighed, and then crushed by hand using an agate mortar and pestle until ground into a fine powder.

Figure 3.1 Filter tower setup

3.1.3 Sample preparation for pore fluid trace element analysis

After pore fluid was separated from the sediment, as described in Section 3.1.1, it was prepared for trace element analysis. Approximately 1 mL of pore fluid was removed from the separated total and weighed using an analytical balance. This was then diluted to approximately 1:10 gravimetrically with 2% HNO_3 immediately after filtering.

3.1.4 Digestion procedure for sediment ICP-MS analysis

For major and trace element analysis of sediment from the core and traps, a multiple step HF-HNO_3 digestion and dilution procedure was followed using a method modified from Eggins et al. (1997). Digestion batches contained duplicates, procedural blanks, and the standards: BCR-2, DNC-1, BIR-1a, IAEA-405, DR-N, SY-4, LKSD-2, IF-G and AGV-1 (Table 3-1).

Table 3-1 Geologic rock standard information (Source: GeoRem)

Standard	Standard Information
BCR-2	Columbia River Basalt; USGS
DNC-1	Olivine-normative dolerite; USGS
BIR-1a	Icelandic Basalt; USGS
IAEA-405	Estuarine sediment powder; International Atomic Energy Agency (IAEA)
DR-N	Diorite powder; Centre de Recherches Petrographiques et Geochimiques (CRPG)
SY-4	Diorite gneiss powder; NRCan
LKSD-2	Lake sediment powder; NRCan
IF-G	Iron formation powder; CRPG
AGV-1	Andesite powder; USGS

For each sample and standard, 0.1000 g ± 0.001 g (or 0.02-0.03 g for sediment trap samples with limited sample mass; volumes of acid used for smaller samples in brackets) was

weighed into a 15 mL Teflon vial. Then, 5 mL (2.5 mL) of concentrated environmental grade HF and 0.5 mL (0.25 mL) 16 N HNO_3 were added to each sample, standard, and blank and set on a hot plate at 125°C for at 24 hours. Samples were then left to dry with the lids off on the hot plate at ~150°C. Once the samples were dried down, some dark coloured material remained in the vials which is thought to be organic material did not dissolve. After samples were dry, 4 mL (2 mL) of 8M Environmental Grade HNO_3 and 1 mL (0.5 mL) of 0.2 M oxalic acid were added and left on a hot plate at 125°C for 12 hours. The addition of oxalic acid is to help with the dissolution of samples with high Fe by complexing the Fe in the sample and increasing its solubility (Longerich et al., 1990). Samples were once again dried at ~150°C and 4 mL (2 mL) of 8 M HNO_3 and 0.5 mL of 0.2 M oxalic acid were added. After the second dry down, some material remained un-dissolved in the on-axis sediment trap samples. In an attempt to dissolve the residual material another 4 mL of 8 M HNO_3 and 1 mL of 0.2 M oxalic acid were added to the samples, and they were left on the hot plate overnight. Some material remained undissolved so before drying down, a solution composed of 1 mL 0.2 M oxalic acid and 0.667 mL concentrated HCl was added and set on a hot plate at 150°C to dry. This step was successful in dissolving the material and was not dried to completion as some material started to reprecipitate. Samples were watched carefully and frequently agitated, they were removed from the heat immediately when reprecipitation was observed. After this, 4 mL of 8 M HNO_3 and 1 mL of 0.2 M oxalic acid were added, vials were capped and left on a warm (~80°C) hot plate overnight. Some of the dark particulate material remained undissolved, but if, as thought, this is charred organic matter it will not have a significant impact on determined metal concentrations.

Samples were then diluted to reduce the signal of highly concentrated elements, minimize matrix effects, and reduce the risk of contamination during the analysis. A two-step dilution procedure was used to reduce the chance of barite precipitating out of the sample before analysis due to the decrease in acid strength, with the second dilution done on the day of analysis.

As the first dilution step, 8 M HNO_3 was added to the dried down sample using a benchtop balance in the fume hood until an approximately 250-fold dilution factor was reached (Table 3-2).

Table 3-2 Mass of acid required to achieve a 250-fold dilution with varying sample mass

Sample Mass (g)	Mass 8 M HNO_3 added (g)
0.1	25
0.03	7.5
0.027	7
0.025	6

The mass was then precisely determined using an analytical balance. The first dilution factor (DF1) was calculated using:

$$\mathrm{DF1} = \frac{\mathrm{M_S + M_A}}{\mathrm{M_S}} \quad (\mathrm{Eq.\ 3.1})$$

Where, M_s is the mass of the solid sample digested, and M_A is the mass of 8M HNO_3 added.

On the day of analysis, 1 mL of the 8 M HNO3 solution at a 250x dilution factor was removed with a pipette and weighed using an analytical balance (1 mL of 8M is approximately 1.2 g (M_{DF1})). Then 9 mL of DI was added and weighed. Samples were diluted to ~2200x. The final dilution factor (DF2) was calculated from:

$$\mathrm{DF2} = \frac{\mathrm{M_{DF1} + M_W}}{\mathrm{M_d}} \quad (\mathrm{Eq.\ 3.2})$$

$$\mathrm{M_d} = \frac{\mathrm{M_{DF1}}}{\mathrm{M_S + M_A}} \mathrm{x\ M_S} \quad (\mathrm{Eq.\ 3.3})$$

Where M_{DF1} is the mass of sample from the first step of dilution (sample diluted to 250x with 8 M HNO_3); M_d is the mass of the initial digested sample being diluted in the second dilution step; and M_W is the mass of DI water added.

3.1.5 Preparation and dilution of standards

Standards were prepared identically to the samples. For the analysis of the on-axis sediment trap samples a multi-element spike was added to some of the standards to extend the concentration range for the calibration of elements that occur in very high abundances (Table 3-3) using standards BIR-1a, SY-4, and AGV-1. A sulfur-spike was added to IF-G. The multi-element spike contained the following elements and concentrations:

Table 3-3 Concentrations of elements in the prepared multi-element spike solution

Element	Concentration (ppb)
Mn	13701
Cu	71030
Zn	71261
As	1568
Se	149.8
Sr	12112
Mo	500.5
Ag	149.8
Cd	450.2
Sb	74.8
Ba	69216
Pb	3793
Tl	149.8

Three reference standards were prepared with two different amounts of spike solution. The low concentration spiked standards were prepared with 1 mL of solution diluted to 250x with 8 M HNO_3, 0.2 mL of the spiked solution, and 9.8m mL of DI water. The high concentration spiked standards were prepared with 1 mL of solution as above, 1 mL of spiked solution, and 9 mL of DI water. The spiked standards have a final dilution factor of 2200x.

For the pore fluid analysis, a Pacific seawater standard collected by the Cullen lab was used. A multielement spike was added to the seawater standard to create a three-point calibration curve with pure seawater, seawater + 10 ppb spike added, and seawater + 20 ppb spike added. The elements added to the seawater spike included: Cr, V, Mn, Fe, Co, Ni, Cu, Zn, Mo, Ag, Cd, Ba, Pb, U.

3.1.6 Preparation of drift solution

For sediment core samples and the off-axis sediment trap samples, small aliquots of multiple samples were mixed and diluted to the same dilution factor as the samples to make a drift monitor with a composition that represents an "average" of the samples. A separate drift monitor was made for the on-axis sediments because the concentrations some elements in near vent sediments are significantly higher than off axis. The on-axis drift solution was made with a combination of multiple on-axis sediment trap samples and diluted identical to the samples to make an average representative solution of the concentrations of the on-axis samples.

3.1.7 ICP-MS analysis instrument set-up

Samples were analyzed at the University of Victoria using an Agilent 8800-100 Triple Quadrupole ICP-MS. The instrument conditions such as the nebulizer and carrier gas settings, sample gas, and lens settings are optimized daily for instrument stability, oxide formation and doubly charged ion formation. The Ar auxiliary gas flow rate is set at 1 L/min, sample gas flow rate at 1 L/min, and Ar plasma gas at 12-14 L/min. Samples were analysed both with helium gas in the collision reaction cell, to decrease molecular interferences, and in no gas mode. Helium gas analyses are a single quadrupole ICP-MS analysis, and no-gas mode are a double quadrupole ICP-MS analysis. In single and double quadrupole analyses, the ratio of $^{156}CeO^{1+}/^{140}Ce^{1+}$ is monitored for typical oxide formation and was around on average 3.6% in single quadrupole analysis and 4.7% in double quadrupole analysis. Similarly, the ratio of ThO/Th is also monitored for oxide formation and on average is 0.9% in single quadrupole and 1.12% in double quadrupole analysis.

An internal standard of Indium (^{115}In) is added to each sample, standard, and blank during the sample introduction and the count rate on this is used to correct for changes within the instrument during the analysis and sample matrix effects that may change the analyte signal (Wilschefski and Baxter, 2019).

During analysis of both sediment core and sediment trap samples and pore fluids the contents of each vial were analyzed in four blocks in each analysis, and the average values of

the counts per seconds (CPS) were used for the data reduction. At the beginning of each run, several 2% HNO_3 blanks were run followed by drift solutions and procedural blanks before analysing the standards and samples. For the sediment core, samples were analyzed in blocks of 8 samples, followed by a drift solution, and a procedural blank was run after every 12-15 samples. The sediment trap samples were analyzed in blocks of 5 samples followed by a drift solution, and a blank after every 10 samples, as well as 3-4 analytical duplicates were analyzed randomly during each run.

3.1.8 ICP-MS Data Reduction

Dilution factors for each sample and standard were calculated using equations 3.1-3.3 above. To correct the raw CPS for dilution (CPS_{DF}; Equation 3.4):

$$CPS_{DF} = \mathrm{CPS}_{raw} \text{ x DF2} \qquad (\text{Eq. } 3.4)$$

To correct the CPS for changes in instrument sensitivity during the analysis (CPS_{INT}), the dilution factor corrected CPS for each analyte (CPS_{DF}) was normalized to the raw uncorrected CPS of ^{115}In in that sample (CPS_{In}; Equation 3.5).

$$\mathrm{CPS_{INT}} = \frac{\mathrm{CPS_{DF}}}{\mathrm{CPS_{In}}} \qquad (\text{Eq. } 3.5)$$

For blank corrections (CPS_{BL}), the average of the CPS_{INT} for each procedural blank was taken for each element ($CPS_{BL\text{-}Avg}$). The average was then subtracted from all samples (Equation 3.6):

$$\mathrm{CPS_{BL}} = \mathrm{CPS_{INT}} - \mathrm{CPS_{BL-Avg}} \qquad (\text{Eq. } 3.6)$$

Drift solutions are used to monitor the changes in the sensitivity of the instrument at different masses over the course of the run. Secondary instrumental drift is corrected by normalizing the blank corrected CPS for each analyte in the drift solutions to the first analysis of the drift solution. For each analyte, CPS_{BL} for each drift monitor is normalized to the first analysis of the drift solution, and the slope and intercept of the lines were calculated by regression against the corresponding run number. The equation of the line is used to determine a correction factor applied to each sample (Equation 3.7) with 12 significant figures to reduce rounding errors. For sediment core and pore fluid samples, the drift correction curve was linear as the analysis run was shorter, and less drift monitors were analysed when compared to sediment trap analyses, where a third order polynomial was used.

$$CPS_D = \frac{CPS_{BL}}{D} \qquad (3.7)$$

Where CPS_D is the drift corrected CPS and D is the drift factor.

3.1.9 External calibration

External calibrations are used to convert the signal measured by the ICP-MS detector in counts per second to a concentration using calibration standards with known concentrations to

construct a calibration curve. All analytes in the sediment core samples were calibrated using ten standards BCR-2, DNC-1, BIR-1a, IAEA-405, DRN, SY-4, LKSD-2, IF-G, BHVO-2, and AGV-1. In the sediment traps, all elements except Mn, Cu, Zn, As, Se, Sr, Mo, Ag, Sb, Cd, Ba, Pb, and Tl were calibrated using nine standards DNC-1, BIR-1a, IAEA-405, DRN, SY-4, LKSD-2, IF-G, BHVO-2, and AGV-1. The aforementioned elements were calibrated using six spiked standards (a high and low concentration spike of BIR-1, AGV-1, and SY-4; section 3.2.2) and the above nine un-spiked standards.

The concentrations of each element in the spike standard (X_{SP}) is calculated using Equation 3.8:

$$X_{SP} = \left(\frac{M_S}{M_T} x\, C_{GR}\right) + (M_{SP}\, x\, C_{SP}) \qquad (Eq.\ 3.8)$$

Where M_S is the mass of the initial sample digested (as previously defined), $M_T = M_S + M_{SP} + M_W$; M_{SP} is the mass of the spike solution; C_{GR} = GeoRem concentration multiplied by M_S to determine the concentration of the standard in the solution before the spike is added; C_{SP} is the concentration of the element in the spike solution (Table 3.2).

For each element, the drift corrected CPS for the standard reference materials were regressed against the GEOREM preferred concentration values, and if those were not available the compiled values were used (http://georem.mpch-mainz.gwdg.de/; Table 3-4). The slope of the linear line forced through the origin is used as the calibration factor (Y) to go from CPS_D to concentration in weight percent oxide for major element oxides and parts per million (μg g^{-1}) for trace elements. The concentration is calculated using Equation 3.9:

$$\text{Concentration} = (CPS_D)(Y) \qquad (Eq.\ 3.9)$$

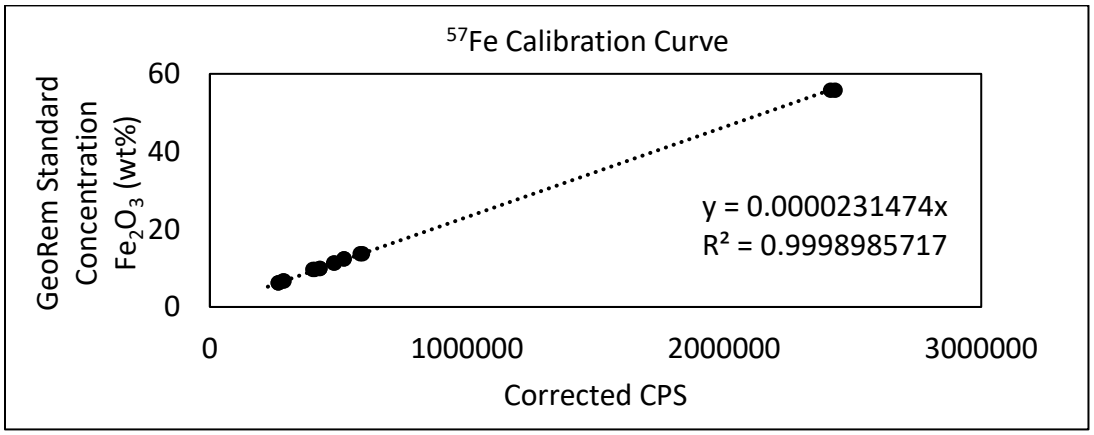

Figure 3.2 Example calibration curve of ^{57}Fe. Calibration curves were constructed for every element after each analysis

Table 3-4 Compilation of GEOREM preferred and compiled standard concentration values
http://georem.mpch-mainz.gwdg.de/
Where no value is reported this standard was not used in the calibration of the element.

	BIR-1a	DNC-1	BHVO-2	AGV-1	DRN	SY-4	IAEA-405	LKSD-2	IF-G
^{7}Li	3.203	5.2	4.5	10.72	40	37	72	20	1
^{9}Be	0.102	1	1.076	2.3	1.8	2.6	3.56	2.5	4.7
^{25}MgO	9.689	10.05	7.257	1.508	4.4	0.54		1.7	1.89
$^{27}Al_2O_3$	15.51	18.3	13.44	17.11	17.52	20.69		12.3	0.15
$^{31}P_2O_5$	0.03	0.07	0.2685	0.4927	0.25	0.131		0.28	0.063
^{34}S	70	392	164	26	350	150		1400	700
^{44}CaO	13.29	11.27	11.4	4.89		8.05		2.2	1.55
^{45}Sc	43.21	31	31.83	12.43	28	1.1	13.5	13	0.3
$^{47}TiO_2$	0.9587		2.731	1.05	1.09	0.287		0.56	0.014
^{51}V	320.6	148	318.2	119.4	220	8	95	77	2
^{52}Cr	392.9	285		9.474	40	12	84	57	4
^{55}MnO	0.1731	0.149	0.169	0.0966	0.22	0.108		0.26	0.042
$Fe_2O_{3(t)}$	11.4	9.93	12.39	6.755	9.7	6.21		6.24	55.85
^{59}Co	52.22	55	44.89	15.14	35	2.8	13.7	17	29
^{60}Ni	168.9	247	119.8	15.41	15	9	32.5	26	22.5
^{63}Cu	120.7	96	129.3	58.42	50	7	47.7	37	13
^{66}Zn	70.4	66	103.9	86.8	145	93	279	209	20
^{71}Ga	15.46	15	21.37	20.36	22	35	18		0.7
^{75}As	0.17	0.12	0.7	0.954	3		23.6	11	1.5
^{78}Se	0.019	0.2	0.18	0.006	0.087		0.44	0.684	
^{85}Rb	0.21	4.5	9.261	67.8	73	55	140	85	0.4
^{86}Sr	108.6	145	394.1	661	400	1191	118	220	3
^{89}Y	15.6	18	25.91	19.69	26	119	23.5	44	9
^{90}Zr	14.8	41	171.2	231.5	125	517	243	254	1
^{93}Nb	0.553	2	18.1	14.53	7	13		8	0.1
^{95}Mo	0.068	0.7	4.07	2.103	0.9		2	2	0.7
^{107}Ag	0.041	0.027	0.089	0.078		0.6	0.939	0.8	
^{111}Cd	0.077	0.18	0.152	0.075	0.9		0.73	0.8	
^{115}In	0.0576		0.117	0.042	0.08				0.02
^{118}Sn	0.701		1.776	4.88	2	7.1	7.6	5	0.3
^{121}Sb	0.462	0.96	0.1034	4.24	0.4		1.81	1.1	0.63
^{125}Te	0.0057	0.021	0.014	0.0022					
^{133}Cs	0.00646	0.3	0.0996	1.252	6.3	1.5	12.5	3	0.06
^{137}Ba	6.75	118	130.9	1218	385	340	486	780	1.5
^{139}La	0.627	3.53	15.2	38.19	21.5	58	40.4	68	2.8
^{140}Ce	1.92	8.19	37.53	68.61	46	122	82.1	108	4
^{141}Pr	0.3723	1.1	5.339	8.31	5.7	15			0.4
^{146}Nd	2.397	4.86	24.27	32.07	23.5	57	37.5	58	1.8
^{147}Sm	1.113	1.4	6.023	5.764	5.4	12.7	6.86	11	0.4

^{115}Eu	0.5	0.59	2.07	1.6			1.25	1.9	
^{157}Gd	1.809	2	6.207	4.862	4.7	14			0.74
^{159}Tb	0.3623	0.39	0.9392	0.673	0.77	2.6	0.93	1.4	0.11
^{163}Dy	2.544	2.76	5.28	3.583	4.6	18.2	6.7	7.3	0.8
^{165}Ho	0.5718	0.65	0.9887	0.68	1	4.3	2.25		0.2
^{166}Er	1.68	1.9	2.511	1.825	2.5	14.2			0.63
^{169}Tm	0.2558	0.33	0.3349	0.2737	0.39	2.3			0.09
^{172}Yb	1.631	1.97	1.994	1.66	2.5	14.8	3.04	4	0.6
^{175}Lu	0.2484	0.309	0.2754	0.2518	0.4	2.1	0.468	0.6	0.09
^{178}Hf	0.5822	1.05	4.47	5.086	3.5	10.6	5.8	7	0.04
^{181}Ta	0.0414	0.098	1.154	0.866	0.6	0.9	1.6	0.8	0.2
^{205}Tl	0.0021	0.026	0.0224	0.337	0.7				0.02
^{208}Pb	3.037	6.2	1.653	36.35	55	10	74.8	44	4
^{232}Th	0.0328	0.22	1.224	6.351	5	1.4	14.3	13.4	0.1
^{238}U	0.01051	0.05	0.412	1.903	1.5	0.8	3	7.6	0.02

3.1.10 Data quality checks for ICP-MS analysis

The precision of the analysis was determined using the procedural and analytical duplicates, where the percent difference of the duplicate measurements was <5% for all elements. The accuracy of the analysis is estimated by comparison of the measured values to the GeoRem recommended values for the standard material.

3.2 ^{14}C analysis

3.2.1 Sample preparation for ^{14}C analysis

Foraminifera were separated from the bulk sediment through wet sieving material for radiocarbon analysis at the University of California Irvine to determine the age of the base of the core. A small aliquot of the bottom 2 segments of the core was thawed to ensure an adequate mass of $CaCO_3$ could be obtained for the analysis. After the sediment thawed, it was wet sieved through a 425 µm and 125 µm mesh using deionized water (DI) water. The material retained in the >425 µm mesh and >125 µm-<425 µm mesh were transferred into two separate Petri dishes and left in an ~40°C drying oven overnight.

Approximately 0.15 mg of foraminifera were separated using a binocular microscope and placed in a small glass vial. Approximately 2 g of finely ground, homogenous bulk sediment from the bottom 2 segments were also sent for bulk ^{14}C analysis. At the Keck Carbon Cycle Accelerator Mass Spectrometry Laboratory at University of California, Irvine (Southon et al., 2004), the foraminifera sample was split by species for analysis: Neogloboquadrina dutertrei (*N. dutertrei),* Globigerinoides ruber *(G. ruber),* and Globigerinoides bulloide *(G. bulloide).* An ATA National Electrostatics (NEC) 0.5MV 1.5SDH-1 accelerator mass spectrometry (AMS) system with a 40-sample MC-SNICS ion source was used for radiocarbon analysis (Southon et al., 2004). The sample preparation and analysis method followed is reported in Rafter et al (2019).

3.3 Inorganic carbon analysis

The inorganic carbon content of the sediment core and sediment trap samples were measured by coulometry at the University of Victoria. Coulometry is based on an electrochemical method where the total charge (total number of coulombs) consumed in the redox conversion of an analyte at an electrode is measured (Hauser, 2019). The coulometer cell is filled with a cathode solution composed of dimethyl sulfoxide (DMSO), ethanolamine, and tetraethylammonium bromide (TEA), an indicator solution, and a platinum electrode, then as gas passes through the solution CO_2 is absorbed. The CO_2 reacts with ethanolamine in the cathode solution, which forms a strong acid and an electrically generate base automatically titrates the acid (UIC Inc.). During this reaction, the analyte in the sample is completely exhausted (Hauser, 2019), and from the total amount of analyte and mass of the sample, the concentration is derived.

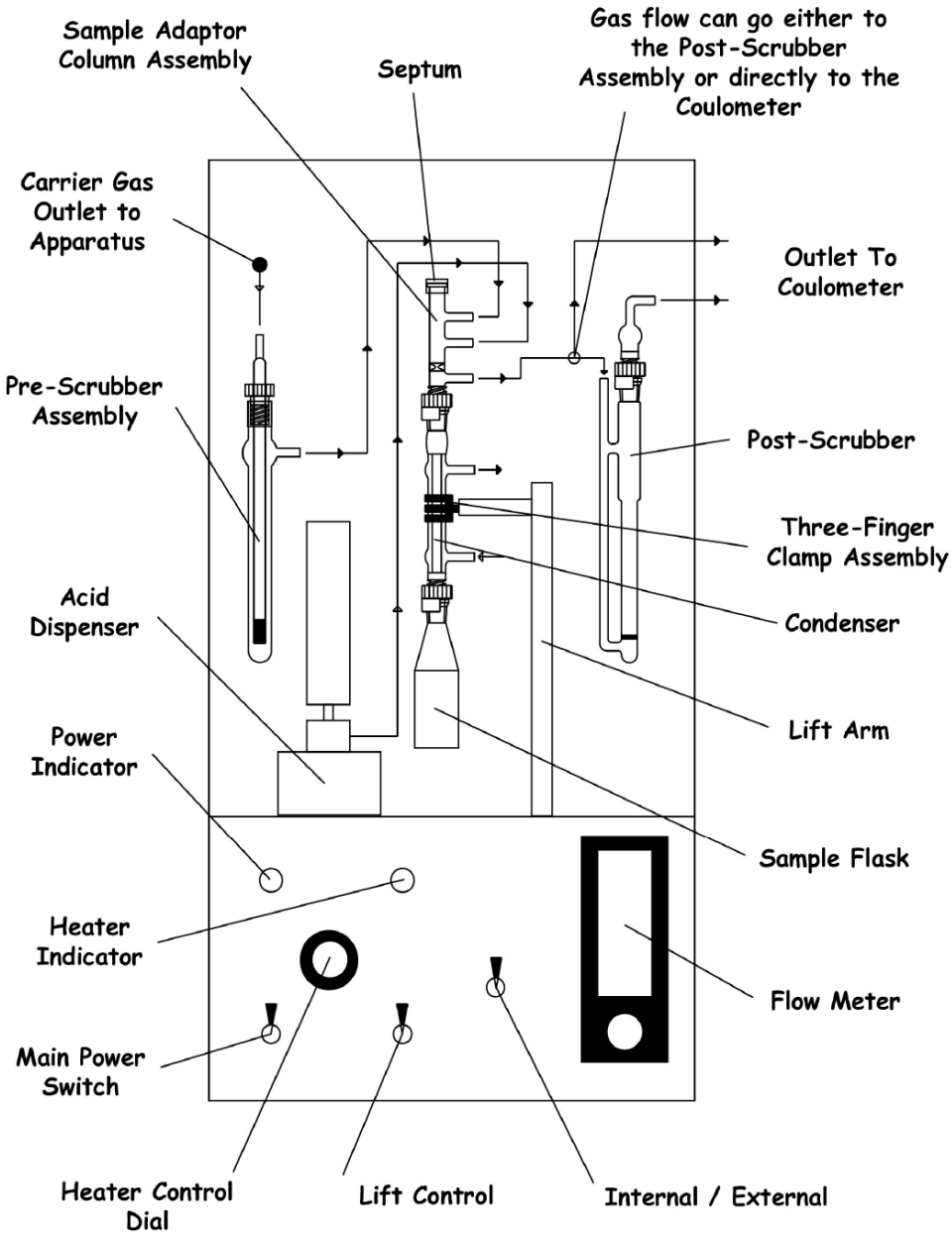

Figure 3.3 CM5130 Acidification module flow diagram (Source: University of Victoria School of Earth and Ocean Science teaching lab designed schematic, based on schematic from UIC Inc. operating manual)

3.3.1 Sample preparation for bulk sediment inorganic carbon analysis

All sediment core samples, and select samples from 2017-2018, 2019-2020 MEF on-axis sediment traps, and 9 km off axis sediment trap samples were analysed at the University of Victoria with a UIC Inc. CM5014 Coulometer for inorganic carbon. Samples were selected to be spread out evenly over the entire sampling period, due to the large mass required for analysis (at least 50 mg) this was decided as sample mass is limited. The coulometer acidification module (Figure 3.3) is set up with a pre-scrubber solution of 45 g of potassium hydroxide (KOH)

to remove CO_2 from the carrier gas and a post-acidification scrubber of 50 g of potassium iodide and a small amount of sulfuric acid until a pH of 3 is reached to remove interfering compounds that are released during sample digestion. At the beginning of each analysis run, 2-3 blanks of 4 mL H_2SO_4 was analysed, and 2-3 $CaCO_3$ standards to determine daily analytical precision and calibration correction. Powdered sediment samples were analysed with the addition of 4 mL H_2SO_4. The analysis of each sample takes 9 minutes, with 3 measurements taken at 3, 6, and 9 minutes, with the final value taken from the 9-minute measurement. The blank value for the analysis is automatically subtracted from the coulometer reading by the instrument, and the final reading is given in weight % carbon of the sample.

3.3.2 Coulometer data correction

Though calibration of the coulometer is not required, the analysis of calcium carbonate standards was used to create a one-point calibration curve of the measured values versus the known concentration of C in $CaCO_3$ (12 wt%) to correct the concentrations measured on each day of the analysis. At the beginning and end of each run 2-3 $CaCO_3$ standards were analysed, the average was taken, and calibration factor was calculated. This allows data to be compared between multiple days of analysis. Multiple duplicate samples were analyzed to determine the precision, which is reported as the standard deviation of the mean.

3.4 Total Carbon, Nitrogen, and Sulfur Analysis

All sediment core samples, as well as the same samples from the on-axis and 9 km off axis sediment traps analysed for inorganic carbon, were analysed at the University of British Columbia with an Elementar Vario MICRO cube CHNS elemental analyzer for total carbon, nitrogen, and sulfur. Sample masses used were between 1.5 to 5.5 mg. Initially, sample masses of 1.5-2 mg were analysed, and then samples with low sulfur and carbon concentrations were repeated with a higher mass ranging from 5-6 mg. The samples were analysed in 4 batches with 45-50 samples per batch.

Due to limited sample available for analysis, and the high amount of sample required to perform reliable and reproducible CNS analysis, the concentration of nitrogen and sulfur were below detection limit for many samples. An optimal sample mass for analysis would be approximately 20 mg. Due to this, the raw data was analysed to isolate the most representative data for the sample. Firstly, the detection limit was calculated as 3 standard deviations of the mean of the concentrations, the detection limits are as followed and anything below detection limit was automatically excluded from the dataset: N = 1 µg, C = 11 µg, S = 11 µg. Secondly, the limit of quantification is calculated as 10 standard deviations of the mean of the concentrations, this the value at which there is some confidence in the data, the limit of quantification for the analysis are as followed: N = 3 µg, C = 35 µg, S = 21 µg. Concentrations above the limit of quantification were included in the final dataset. When concentrations were between the limit of detection and limit of quantification, each sample was individually assessed, and the following criteria were used to choose the final dataset.

- Samples with a higher mass analysed are likely more representative of the sample, if the concentrations of the analysis with the higher mass was larger than the limit of quantification, the analysis of the smaller mass sample was excluded from the dataset.
- Duplicates of a similar mass with concentrations within 10% of each other were averaged and the standard deviation is reported as an error bar on all plots
- Duplicate samples with a low sample mass resulted in concentrations with >50% difference, were excluded as this was likely due to sample inhomogeneity.
- Duplicate samples with a low mass and high mass analysis with concentrations within 10% of each other, the concentrations are averaged, and the standard deviation is reported as an error bar on all plots.

4 Results

The geochemistry of sediment trap samples at the Main Endeavour Field (MEF) will be presented using an elemental classification based on their likely origin; terrigenous derived elements (Ti and Al), largely hydrothermally derived elements (Fe, Cu, Zn, Mn, Ag, Mo), elements largely scavenged from seawater by hydrothermally derived particles (Pb, As, Cd, P), and biological material (C and N). This elemental classification will be used to present and discuss the sediment data in terms of spatial and temporal variability. As there were sediment traps placed at three distances from active venting, the spatial variation of these elements will be presented from on-axis at the MEF, 3 km off-axis, the uppermost segments of the core collected 2.8 km off axis, and 9 km off axis. Variability of element concentrations over the course of the year of sampling will also be examined. Samples were collected over three periods on-axis at the MEF (2014-2015, 2017-2018, and 2019-2020), as well as one sampling period in 2019-2020 at the 3 km off-axis and 9 km off-axis locations. The sediment core H-1581 that was collected 2.8 km from active venting preserved ~6,000 years of sedimentation, the elemental concentrations through the core will be examined. Pore fluid chemistry for the sediment core is also presented to understand post-depositional changes.

4.1 Sediment mass accumulation rates

Sediment mass accumulation rates (MARs) are calculated for each sediment trap period and reported in Table 4-1. Over the sampling period, there are small scale variations with the assumption that the accumulation rate is constant per day over the sampling period, with a range in daily mass accumulation rates from 3.6 – 13.1 mg m^{-2} day^{-1} observed across the three on-axis sediment trap sampling periods (Figure 4.1 D).

The 9 km off axis sediment trap has a mass accumulation rate of 15.76 g m^{-2} $year^{-1}$ (Table 4-1) averaging 43 mg m^{-2} day^{-1}. There are large variations in the mass accumulation rate in each sample period, on a similar scale to those observed in the on-axis sediment trap samples, with a range of daily mass accumulation rates from 9-178 mg m^{-2} day^{-1} (Figure 4.1 E).

Table 4-1 Sediment trap sampling dates and mass accumulation rates.

Sediment Trap Location	Sampling Start	Sampling End	Total Sampling Days	Mass accumulation Rate (g m^{-2} $year^{-1}$)
2014-2015 MEF On-Axis	May 23, 2014	May 18, 2015	234	32.1
2017-2018 MEF On Axis[1]	July 1, 2017	July 14, 2018	378	18.08
2019-2020 MEF On Axis	May 16, 2019	September 10, 2020	483	24.84
3 km off axis[2]	October 1, 2019	March 10, 2020	165	3.07
9 km off axis[3]	October 1, 2019	May 30, 2020	240	15.76

1. The last sample collected from the 2017-2018 sediment trap had no evidence of the closing mechanism malfunctioning, though the sample mass is 4 g, approximately 8x higher than the rest of the samples. Included in the calculation of total mass.
2. 3 km off axis sediment trap malfunctioned and the final bottle was open from February 28, 2020-September 28, 2020 (213 days) and collected 2.09 g of sediment. This sample is excluded from analysis as bottle was open as it returned to the surface and likely contaminated.
3. Sample 2 in the 9 km off axis sediment trap had contamination from brine precipitation and was excluded from mass calculations and geochemical analysis.

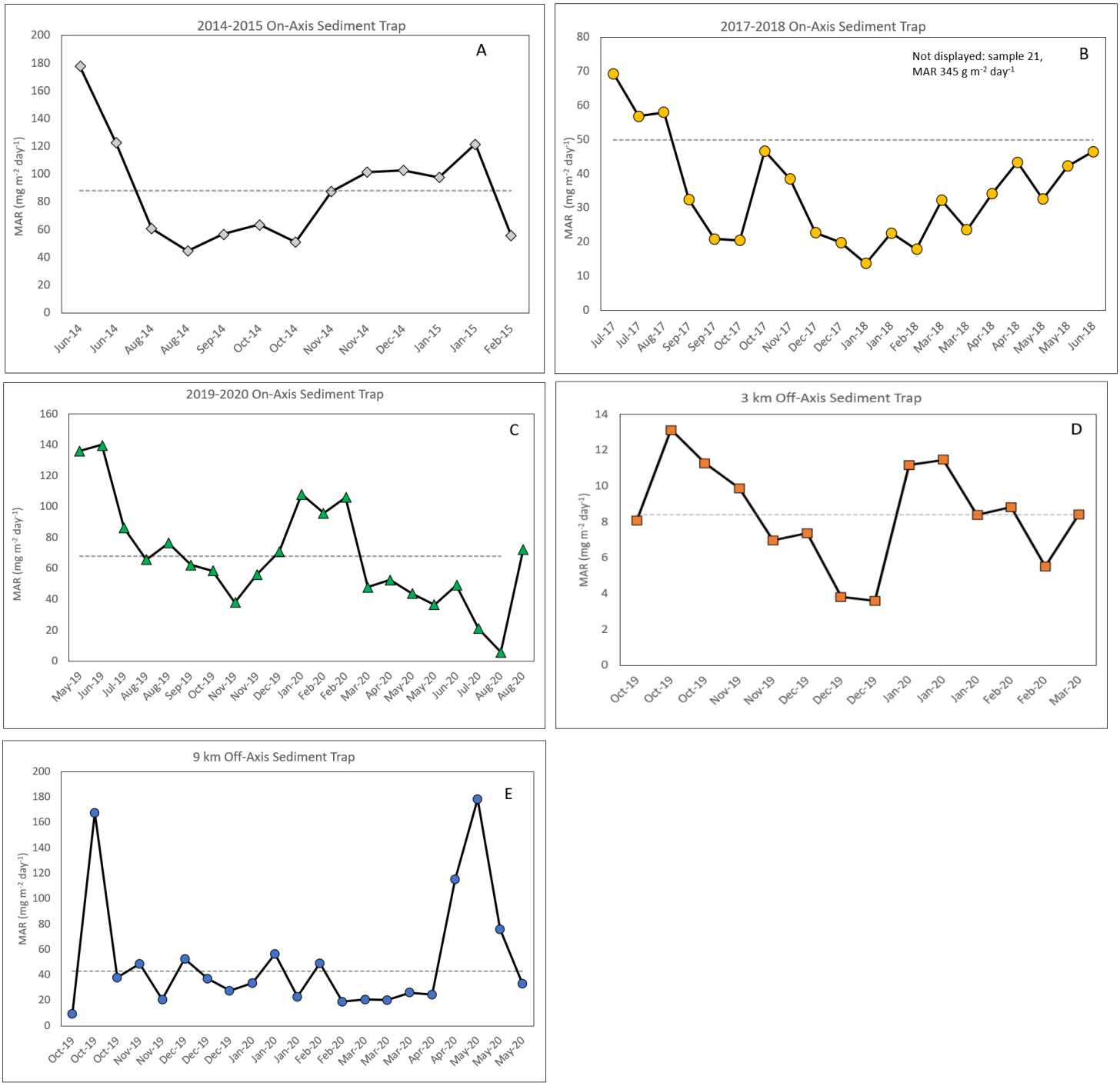

Figure 4.1 Average daily mass accumulation rates (mg m^{-2} day^{-1}) for on-axis (A-C), 3 km (D) and 9 km (E) off axis sediment trap collection periods. Grey dashed line represents steady state accumulation rate.

4.2 Spatial variation in sediment geochemistry

The aim of this section is to describe how the hydrothermally derived component of the sediments vary with distance from active venting. For the most part, the concentration of metals is presented using the proportion of the total that is of hydrothermal origin. This is calculated by removing the contribution from detrital material from the total concentration, with the assumption that the concentration of background, terrigenous derived sediment has the same composition as the Cascadia Basin sediments as reported by Carpentier et al. (2013). The continental detrital component supplies excess metals to marine sediments surrounding hydrothermal vent systems, thus is removed to isolate the hydrothermal signal (Costa et al., 2016). This approach is detailed in Section 4.2.2. Most metals discussed will be compared to hydrothermally derived Fe (Fe_{HT}), as it has high concentrations in hydrothermal fluids, and particulate Fe-bearing minerals such as Fe-Mn oxyhydroxides in the plume adsorb many elements from seawater by scavenging.

4.2.1 Terrigenous input

An understanding of how the proportion of terrigenous material changes moving off axis helps us to constrain how the hydrothermal component changes with distance from the vents. Ti and Al are used as tracers for terrigenous material as they are predominantly sourced from the continent, and have low concentrations in seawater, hydrothermal vent fluids and hydrothermal particles (German and Seyfried, 2013). Ti is almost entirely derived from the lithogenic fraction (Murray and Leinen, 1993) whereas Al can be enriched in hydrothermal fluids relative to seawater (Shimmield and Price, 1986; Von Damm and Bischoff, 1987); therefore the concentration of Ti is used as a proxy for continental material in the sediments near the hydrothermal vents. Sediment trap samples are found to lie on a mixing line between a hydrothermal component, which has a near zero concentration of these elements and detrital sediments from the Cascadia Basin (Carpentier et al., 2013).

One way of understanding how the hydrothermal component of elements change moving off axis is by separating the hydrothermally derived elemental component from the detrital Cascadia Basin component of that element as the total concentration of these elements are from two sources. For calculation of the hydrothermal component of Fe, Cu, Zn, and Mn, it is assumed that there is a negligible contribution from seawater scavenging and biological debris. This approach may over- or under-estimate the hydrothermal component in the off axis sediment trap (Costa et al., 2017) because the concentration ratio of $X_{Cascadia\ Basin}/Ti_{Cascadia\ Basin}$ (where X is a major or trace element) in the sediment may vary. Costa et al. (2017) approached this method of calculating the hydrothermal component of Juan de Fuca Ridge sediments by detailing the various potential lithogenic endmembers (Table 4-1).

Within the Endeavour hydrothermal vent field, the most appropriate endmember is Cascadia Basin sediments, taken from ODP 168 – Site 1027 sediments, which are likely the most predominant source of terrigenous sediment (Carpentier et al., 2013). To identify the bulk composition of the siliciclastic material in the central Cascadia Basin that is most representative

of the area, the raw data was manipulated to remove samples that have very high CaO concentrations (sample 1027C 2R2 49-97) and high MnO and low Fe_2O_3 (sample 1027 B56 X2 133-34). The average value for each element was calculated and the uncertainty on this. For elements not reported in Carpentier et al. (2013) for the Cascadia Basin, the average Upper Continental Crust concentrations were used, as reported by Rudnick and Gao (2013). These values, reported in (Table 4-3), were then used in a 1000 iteration Monte Carlo simulation on Equation 4.1 to determine the hydrothermal element concentration and the error associated with the removal of the Cascadia Basin terrigenous component. Each calculated concentration has an associated error, noted with error bars on all further plots.

Table 4-2 Fe/Ti lithogenic endmembers as reported in Costa et al. (2017) and references therein, to compare to the Cascadia Basin endmember used in this study

Potential Lithogenic Source Material	Fe/Ti ratio
Average Upper Continental Crust	11.7
Asian dust	~11
Pelagic Pacific Sediments	10-11
Mid-Ocean Ridge Basalts	8
Columbia River Sediments	6.7
Regional turbidite layer	10.7-11.5

To calculate the hydrothermal component, Eq. 4.1 can be used to quantify the amount of the element contributed from detrital material assuming all the TiO_2 is derived from the background, terrigenous sediment. The detrital concentration is subtracted from the total element concentration to determine the hydrothermally derived component. The following equation is written for iron, though modified for each element.

$$\mathrm{X_{hydrothermal}} = \mathrm{X_{measured}} - \mathrm{Ti_{measured}} \left(\frac{\mathrm{X_{Cascadia\ Basin}}}{\mathrm{Ti_{Cascadia\ Basin}}} \right) \qquad (\mathrm{Eq.}\ 4.1)$$

Table 4-3 Concentration and uncertainty values used to calculate the hydrothermal component of each element using a Monte Carlo simulation. Cascadia Basin data reported by Carpentier et al. (2013) and Average Upper Continental Crust reported by Rudnick and Gao (2013). The uncertainty is 1 standard deviation on the mean.

Cascadia Basin Concentrations Site 1027 (Carpentier et al., 2013)	Average (wt% oxide)	± Uncertainty
TiO_2	0.81	0.02
Al_2O_3	16.41	0.2
Fe_2O_3	7.36	0.22
MnO	0.15	0.03

P_2O_5	0.21	0.01
	µg g^{-1}	**± Uncertainty**
V	148.88	31.98
Cr	80.16	2.28
Co	20.04	1.17
Ni	52.50	2.40
Cu	49.83	3.08
Zn	115.90	6.44
La	19.49	0.60
Ce	39.79	1.11
Pr	4.96	0.13
Nd	20.17	0.49
Sm	4.29	0.10
Eu	1.10	0.02
Gd	4.10	0.10
Tb	0.64	0.02
Dy	3.85	0.10
Ho	0.79	0.02
Er	2.24	0.06
Yb	2.18	0.05
Lu	0.32	0.01
Hf	3.28	0.10
Pb	12.45	0.75
U	1.86	0.09
Average Upper Continental Crust (Rudnick and Gao, 2013)	**Average (µg g^{-1})**	**± Uncertainty**
Mo	1.1	0.3
As	4.8	0.5
Cd	0.09	0.01

The concentration (µg g^{-1}) and mass accumulation rates (µmol m^{-2} day^{-1}) of terrigenous elements (Ti and Al) are lowest in the on-axis sediment trap samples. The samples collected in the on-axis sediment trap have Ti concentrations between 380 and 900 µg g^{-1} in the 2014-2015 sediment trap, 840 and 1,700 µg g^{-1} in the 2017-2018 sediment trap, and 370 to 1,600 µg g^{-1} in the 2019-2020 sediment trap. The sediment trap samples from 3 and 9 km off axis have Ti concentrations ranging from 750 to 2,500 µg g^{-1}, and 1,100-3,300 µg g^{-1} respectively. Similarly, for Al, the on-axis sediment trap samples have concentrations between 6,619 and 15,956 µg g^{-1} in the 2014-2015 sediment traps, 12,500 and 26,300 µg g^{-1} in 2017-2018 sediment traps, and 5,454 and 24,034 µg g^{-1} in the 2019-2020 sediment traps. The sediment trap samples from 3 and 9 km off axis have an Al concentration ranging from 13,300 and 41,500 µg g^{-1}, and from 19,900 and 58,500 µg g^{-1}, respectively. The Ti/Al ratio is similar in all sediment traps at 0.067 in

both the 2017-2018 and 2019-2020 on axis sediment traps, and slightly lower at 0.058 in the 2014-2015 on axis, 3 km off axis, and 9 km off axis sediment traps.

The mass accumulation rate of Ti and Al is similar in the on-axis and 9 km off-axis sediment trap locations (Table 4-4, Figure 4.3). The mass accumulation rate for the terrigenous derived elements in on-axis sediment traps and 9 km off-axis sediment trap are comparable, with all samples from all years, within one standard deviation of the mean. The mass accumulation rate of Ti for 2014 - 2015, 2017 - 2018, and 2019-2020 on axis sediment traps are 1.15 ± 0.54 µmol m^{-2} day^{-1}, 0.9 ± 0.4 µmol m^{-2} day^{-1} and 1.45 ± 0.98 µmol m^{-2} day^{-1} respectively. The mass accumulation rates of Al for 2014 - 2015, 2017 - 2018, and 2019-2020 on axis sediment traps are 36.1 ± 17.1 µmol m^{-2} day^{-1}, 23.7 ± 11.7 µmol m^{-2} day^{-1}, and 37.0 ± 24.4 µmol m^{-2} day^{-1}, respectively. The mass accumulation rates of Ti and Al in the 9 km sediment trap are 2.04 ± 1.38 µmol m^{-2} day^{-1} and 65.2 ± 39.7 µmol m^{-2} day^{-1}, respectively. Material accumulation rates in the 3 km off axis sediment trap were much lower due to the trap malfunction, than in the on-axis and 9 km off axis sediment traps. The mass accumulation rate of Ti and Al are 0.30 ± 0.11 µmol m^{-2} day^{-1} and 9.0 ± 3.4 µmol m^{-2} day^{-1} respectively.

Table 4-4 Concentration and MARs of terrigenous elements in the on-axis, off-axis sediment trap samples and sediment core

	Titanium				**Aluminium**			
	Concentration (µg g^{-1})		MAR (µmol m^{-2} day^{-1})		Concentration (µg g^{-1})		MAR (µmol m^{-2} day^{-1})	
	Range	*Average*	*Average*	*SD*	*Range*	*Average*	*Average*	*SD*
2014-2015 MEF On Axis	384 – 906	631	1.16	0.54	6,619 – 15,956	11,073	36.1	17.1
2017-2018 MEF On Axis	839 - 1,696	1255	0.9	0.4	12,487 – 26,302	18,597	23.7	11.7
2019-2020 MEF On Axis	374 – 1,596	976	1.45	0.98	5,454 – 24,034	14,008	37	24.4
3 km off axis	754 – 2,535	1719	0.3	0.11	13,296 – 41,466	29,151	9	3.4
9 km off axis	1,118 – 3,284	2428	2.04	1.38	19,939 – 58,474	42,431	65.2	39.7
H-1581	2,600 - 3,600	3,078						

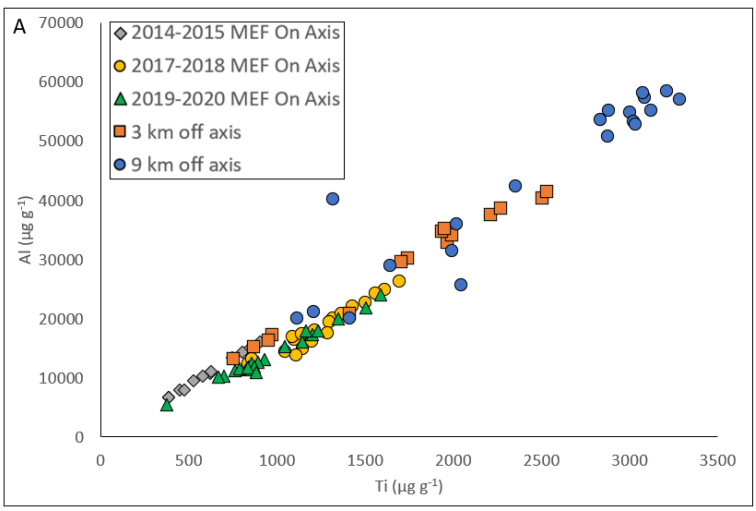

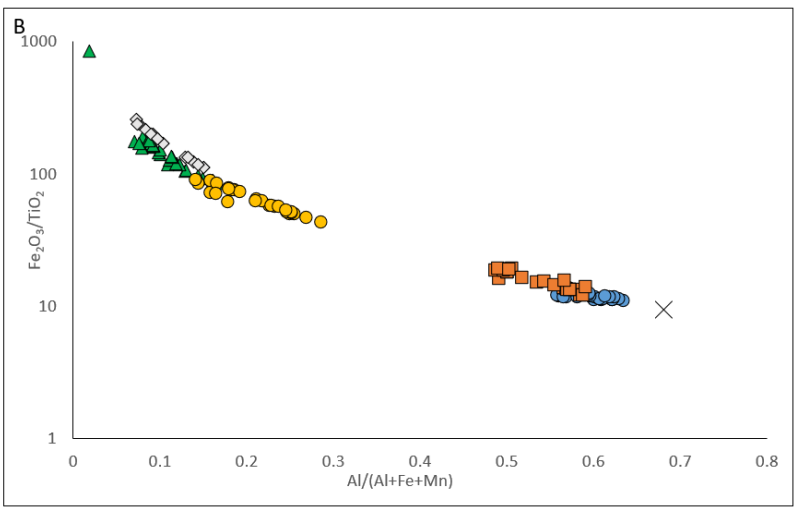

Figure 4.2 (A) Concentrations of Ti and Al, thought to be derived entirely from the terrigenous component, in sediment traps compared to endmember Cascadia Basin B. Comparison of Al/(Al+Fe+Mn) versus Fe/Ti to compare the amount of ferromanganoan material with the ratio of hydrothermal material to detrital material. Cascadia Basin background sediment composition (marked X)

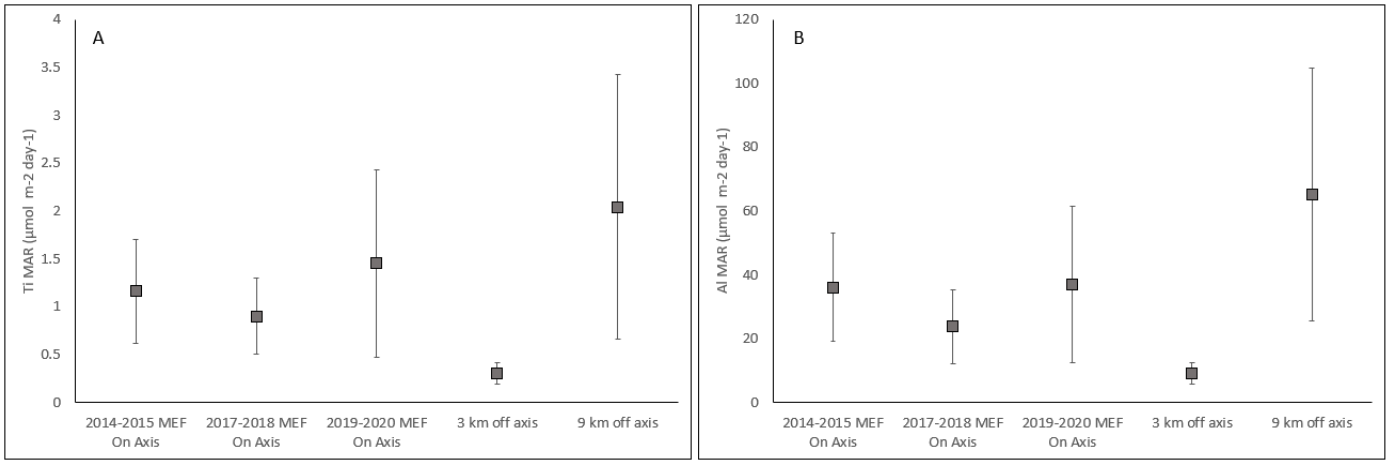

Figure 4.3 (A) Ti mass accumulation rate (µmol m^{-2} day^{-1}) for on axis, 3 km off axis and 9 km off axis sediment traps, reported as average with error bars representing one standard deviation. (B) average Al mass accumulation rate (µmol m^{-2} day^{-1} ± 1SD)

The ratio of Al/(Al+Fe+Mn) is used to identify Al-poor ferromanganoan sediments close to the ridge axis (Bostrom and Peterson, 1968). As previously discussed, Fe and Mn are used as tracers of hydrothermal activity, and Al and Ti are immobile in hydrothermal fluids (German and Seyfried, 2013), and the main source for Al and Ti are terrigenous material. A plot of Fe_2O_3/TiO_2 versus Al/(Al+Fe+Mn) is used to identify variation in the amount of hydrothermal and detrital components of sediments (Figure 4.4; Hrischeva and Scott, 2007). Sediments collected by on axis sediment traps have the highest Fe_2O_3/TiO_2 and lowest Al/(Al+Fe+Mn), indicative of a high ratio of hydrothermal to terrigenous material. As hydrothermal input decreases at 3 km off axis and further at 9 km off axis, the Al/(Al+Fe+Mn) ratio increases, approaching the Cascadia Basin sediment end-member (

Figure 4.2B).

4.2.2 Hydrothermal elements

Variations in the concentration of elements derived from hydrothermal fluids (Fe, Cu, Zn, Mn, Ag and Mo) are dictated by the distance from the vent as these elements are enriched in primary vent fluids, and the non-buoyant plume can exhibit concentrations 100-fold higher than ambient seawater (German and Seyfried, 2013). Fe, Cu, Zn, and Mn are the primary hydrothermal elements that will be considered in this section, though Ag and Mo have the same behaviour and are largely hydrothermally derived, though also sourced through seawater

scavenging.

Table 4-5 Concentrations and Mass Accumulation Rates of hydrothermally derived Fe, Cu, Zn, and Mn in the on-axis and off-axis sediment trap samples, and sediment core

	Iron				**Copper**			
	Concentration ($\mu g\ g^{-1}$)		MAR ($\mu mol\ m^{-2}\ day^{-1}$)		Concentration ($\mu g\ g^{-1}$)		MAR ($\mu mol\ m^{-2}\ day^{-1}$)	
	Range	*Average*	*Average*	*SD*	*Range*	*Average*	*Average*	*SD*
2014-2015 MEF On Axis	91,151 – 135, 466	113,706	173.1	55.1	6,263 – 11,629	8,291	11.6	5.97
2017-2018 MEF On Axis	42,140 – 106,903	78,850	46.2	16.2	2,848 – 8,172	5,698	2.91	0.98
2019-2020 MEF On Axis	101,490 – 462,228	156,325	184.2	96.8	7,578 – 11,900	9,997	9.48	4.64
3 km off axis	8,266 – 14,495	10,872	1.68	0.54	237 – 729	445	0.061	0.014
9 km off axis	4,305 – 9,185	6,988	5.21	3.52	50.8 – 165	111	0.069	0.037
H-1581	14,778 – 29,323	25,891			109 – 280	184		
	Zinc				**Manganese**			
	Concentration ($\mu g\ g^{-1}$)		MAR ($\mu mol\ m^{-2}\ day^{-1}$)		Concentration ($\mu g\ g^{-1}$)		MAR ($\mu mol\ m^{-2}\ day^{-1}$)	
	Range	*Average*	*Average*	*SD*	*Range*	*Average*	*Average*	*SD*
2014-2015 MEF On Axis					614 – 1,865	1,059	1.61	0.61
2017-2018 MEF On Axis	3,184 – 13,220	8,170	4.26	2.2	405 – 2,447	1,020	0.61	0.33
2019-2020 MEF On Axis	12,318 – 26, 454	18,138	18.8	9.16	660 – 2,572	1,680	2.11	1.27
3 km off axis	297 – 2,205	717	0.101	0.06	988 – 3,741	2,240	0.33	0.084
9 km off axis	50.5 – 392	124	0.072	0.04	2,191 – 5,459	4,089	3.01	1.77
H-1581	125 – 394	174			591 – 4,057	928[1]		

1. Manganese concentrations in sediment core H-1581 reported as the total Mn concentration, not the hydrothermally derived component as once detrital Mn/Ti content has been removed the concentration of Mn below the redox transition zone in the sediment core is calculated to be below zero due to redox remobilization.

The total Fe content of the on-axis sediment traps range from 42,000 to 460,000 μg g^{-1} where 80 to 99% of the total Fe in the on-axis sediment trap samples is hydrothermally derived. The hydrothermal component of the on-axis sediment trap samples is highest due to the proximity to the vents, with concentrations having a large range between and within sampling periods: 91,100 – 135,500 μg g^{-1} (2014-2015), 42,100 – 106,900 μg g^{-1} (2017-2018), and 101,500 – 462,200 μg g^{-1} (2019-2020). The concentration of hydrothermally derived Fe in the 3 km off axis sediment trap ranges from 8,300 – 14,500 μg g^{-1} and further decreases 9 km off-axis ranging from 4,300 – 9,200 μg g^{-1} (Figure 4.4, Table 4-5). The percentage of the total Fe that is derived from a hydrothermal source is lower in the off-axis sediment traps, with 16-28% of the total Fe in the 9 km off-axis trap calculated to be hydrothermally derived.

In the hydrothermal plume, Cu and Zn precipitate quickly with the rapid formation of sulfide minerals. The calculated concentrations of hydrothermally derived Cu and Zn in the on-axis sediment traps range an order of magnitude from 2,800 – 12,300 ug g^{-1} and 3,200 – 27,500 ug g^{-1}, respectively. Almost 100% of the Cu and Zn in the on-axis sediment trap is derived from hydrothermal material, with hydrothermally derived Cu ranging from 99.6-99.9% of the total Cu, and hydrothermally derived Zn ranging from 99.2-99.9% of the total Zn. In the 3 km off axis trap, the concentrations of hydrothermally derived Cu and Zn are lower than in the samples from the on-axis traps by one to two orders of magnitude and range from 237 – 729 ug g^{-1}, and 297 – 2205 ug g^{-1}, respectively. In the 9 km off axis trap, there is a further decrease in Cu and Zn concentrations, ranging from 50.8 – 165 ug g^{-1} and 50.5 – 392 ug g^{-1}, respectively (Figure 4.4, Table 4-5). The concentration of Cu, Zn and Fe in the 9 km off axis sediment trap remains elevated above Cascadia Basin background sediment concentrations. 75-86% of the total Cu and 59-91% of the total Zn in the 9 km off axis sediment trap is hydrothermally derived.

The mass accumulation rates of Fe, Cu, and Zn are highest in the on-axis sediment traps and the average mass accumulation rate for both 2014-2015 and 2019-2020 on-axis sediment trap samples are comparable within one standard deviation of the mean. The 2017-2018 sediment trap sample has a lower mass accumulation rate. The mass accumulation rates of Fe, Cu, and Zn are presented in Table 4-5. Where the highest mass accumulation rates are observed in the on-axis sediment trap samples, closest to the vents.

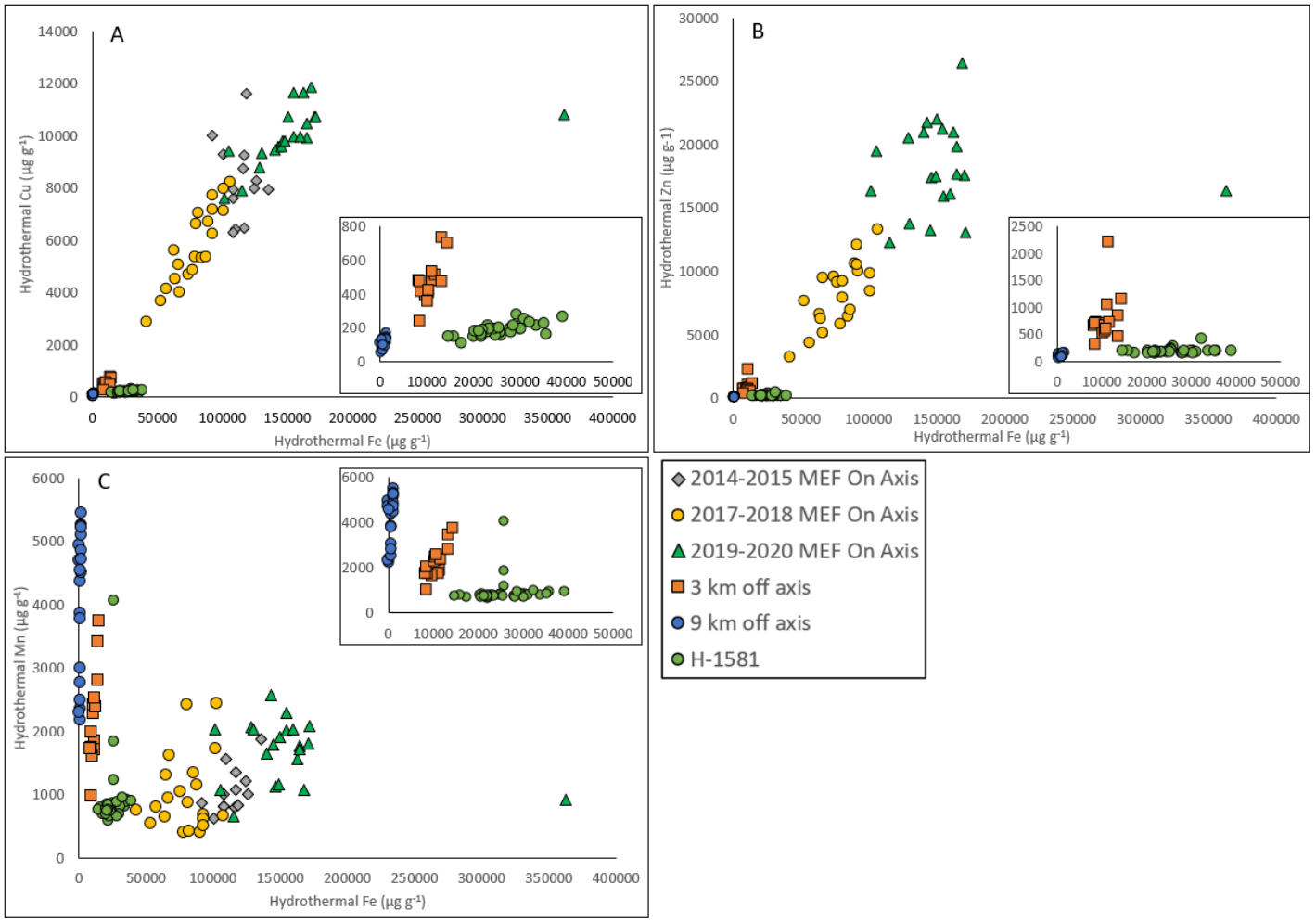

Figure 4.4 Cross plots of the A. calculated concentration of hydrothermally derived Cu against hydrothermally derived Fe for the sample suite. Inset zooms in on the low concentration samples showing that the sediment core samples, H-1581, have lower Cu/Fe in the hydrothermally derived component. B. calculated hydrothermally derived Zn against hydrothermally derived Fe. Inset zooms in on the low concentration samples, showing that the sediment core samples have lower Zn/Fe in the hydrothermally derived component. C. calculated hydrothermally derived Mn against hydrothermally derived Fe. Inset zooms in on the low Fe concentration samples. Sediment core Mn is plotted as total Mn (µg g-1) as the removal of the background component results in concentrations less than zero.

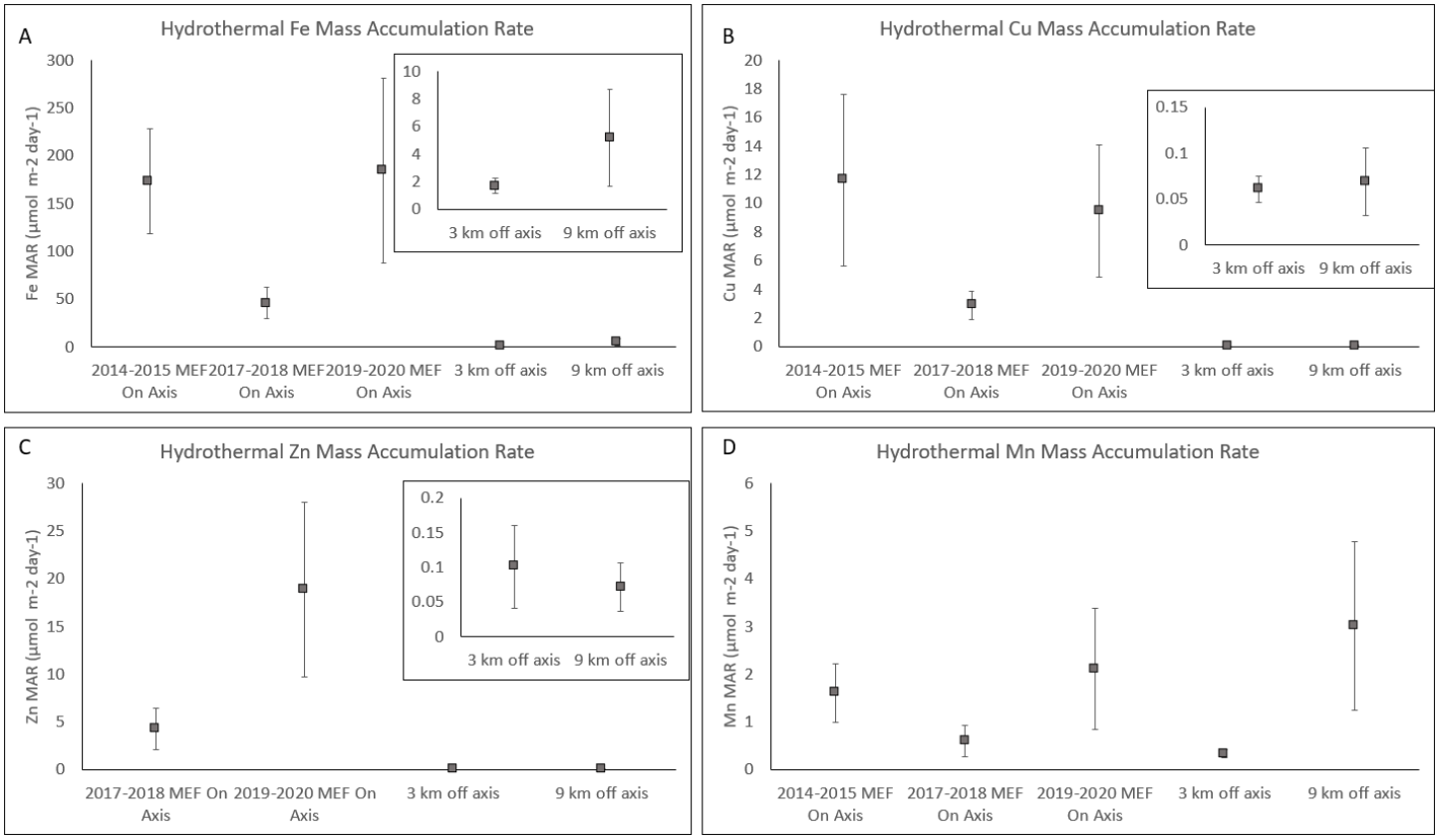

Figure 4.5 Average mass accumulation rate for hydrothermal elements (A) Fe, (B) Cu, (C) Zn, (D) Mn reported as µmol m-2 day-1

Manganese is hydrothermally derived, though its behaviour differs from that of Fe, Cu and Zn, where when hydrothermal Fe is high on axis, Mn concentration is low, and concentrations increase moving away from the ridge axis (Figure 4.4, Table 4-4). In each of the on-axis sediment traps, the concentration of hydrothermal Mn is comparable, range from 600-1,900 µg g^{-1} (2014-2015), 400-2,400 µg g^{-1} (2017-2018), and 660-2,600 µg g^{-1} (2019-2020). At 3 km off axis, the concentration of hydrothermal Mn increases to 990 – 3,700 µg g^{-1}, and further increases at 9 km off axis to 2,200 – 5,500 µg g^{-1} (Figure 4.4, Table 4-5)

Though the Mn concentration increases with distance from the vent, the average mass accumulation rate in the 9 km off axis sediment trap samples is only slightly higher than in the on-axis sediment trap samples. The on-axis sediment trap samples have average mass accumulation rates of 1.6 ± 0.6 µmol m^{-2} day^{-1} (2014-2015), 0.61 ± 0.32 µmol m^{-2} day^{-1} (2017-2018), and 2.1 ± 1.3 µmol m^{-2} day^{-1} (2019-2020). The 9 km off-axis sediment trap samples had a mass accumulation rate of 3.01 ± 1.8 µmol m^{-2} day^{-1}, slightly higher than the on-axis sediment traps samples. The 3 km off axis sediment trap samples had a mass accumulation rate of 0.33 ± 0.08 µmol m^{-2} day^{-1}, much lower than all of the others due to the small mass of sample collected (Figure 4.5,Table 4-5).

Hydrothermal Ag (Ag_{HT}) concentrations in the on-axis sediment traps range from 11-22 μg g^{-1} in 2014-2015 to 2.5 – 11 μg g^{-1} (2017-2018), and 4-22 μg g^{-1} (2019-2020). The concentration of Ag in the sediment trap samples is lower in the 3 km off axis sediment trap samples (0.7-1.5 μg g^{-1}), and lower still (0.3-0.75 μg g^{-1}) in the 9 km sediment trap samples. Mo_{HT} concentrations in the on-axis sediment trap samples range from 46-66 in 2014-2015, 14-63 (2017-2018), and 38-87 (2019-2020). The Mo_{HT} concentration is lower in the 3 km off-axis sediment trap samples (1.5 – 10 μg g^{-1}) in the 3 km off axis sediment trap samples and lower still (0.8-2.5 μg g^{-1}) in the 9 km off-axis sediment trap samples.

4.2.3 Scavenged elements

The detritally corrected, hydrothermal concentrations of the elements Pb_{HT}, As_{HT}, Cd_{HT}, and P_{HT} show strong linear correlations with Fe_{HT} with higher concentrations in the on-axis sediment trap samples and lower concentrations in the off-axis sediment trap samples (Figure 4.6). These elements have been associated with hydrothermal scavenging onto sulfides and Fe-Mn-oxyhydroxides within the hydrothermal plume (e.g, Mottl and McConachy, 1990; Feely et al., 1991; German et al., 1991, 1997; Kadko et al., 1994). These elements may also be in part hydrothermally derived, due to their high concentrations in the on-axis sediment trap samples; it is difficult to distinguish between these processes. Rapid scavenging of these elements by hydrothermal particles occurs quickly near axis. Scavenging is suggested as a controlling process by looking at the ratio of Pb_{HT}/Fe_{HT} and As_{HT}/Fe_{HT} that are higher off axis, which suggest a scavenged component of these elements (Figure 4.5). For the above listed elements, the element/Fe_{HT} ratio is lower in the sediment core samples than any of the sediment trap samples which will be discussed in Section 5.1.

The concentration of phosphorus (P_{HT}) in the on-axis sediment trap samples range from 2,900 – 4,700 μg g^{-1} in 2014-2015, 1,600 – 3,000 μg g^{-1} in 2017-2018, and 2,100 – 4,800 μg g^{-1} in 2019-2020. By subtracting P associated with the Cascadia Basin sediments, we see that between 86 – 98% of the phosphorus is associated with hydrothermal particles. Samples in the 3 km off-axis sediment trap have a lower hydrothermally derived P concentration, ranging from 82017 to 1,600 μg g^{-1}. There are two samples collected at 3 km off-axis with a comparatively high hydrothermally associated phosphorus concentration, with concentrations of 5,900 μg g^{-1} and 7,800 μg g^{-1}. The proportion of hydrothermal versus detrital content in these samples is much higher than the rest of the samples in the 3 km off-axis sediment trap. The hydrothermally associated P in the 3 km off axis sediment trap samples ranges from 64- 90%, whereas in these two samples the hydrothermal proportion is 96% and 97% respectively. These two samples are not high in other hydrothermal elements. This high concentration of P could be of biological origin; however, due to sample size restrictions the 3 km off axis sediment trap samples were not analyzed for carbon and nitrogen, therefore the biological origin cannot be tested, and does not appear to correlate in timing with increased biological input to the other sediment traps at this period of the year. In the 9 km off axis sediment trap samples the P_{HT} ranges from 430 – 740 μg g^{-1}.

Phosphorous is also in part biological in origin. As seen in Figure 4.6, a high concentration of organic C corresponds with a high concentration of P_{HT}, and a low P_{HT}/Fe_{HT} ratio due to the high hydrothermal component. The 9 km off-axis sediment trap samples have a similar organic C content; however, the P/Fe ratio is higher due to the decreased amount of Fe at this distance from active venting. The low organic C, P, and P/Fe ratio in the sediment core can be explained by the breakdown of organic material due to post-depositional processes which will be discussed further below.

In the on-axis sediment traps, 98.8 - 99.8% of the Pb is associated with the hydrothermal component. The concentration of Pb_{HT} ranges between 350-530 μg g^{-1} in the 2014-2015 on-axis sediment trap samples, 220 – 570 μg g^{-1} (2017-2018), and 360-590 μg g^{-1} (2019-2020). Samples from the 3 km off axis sediment trap have a lower Pb_{HT} concentration than the on-axis samples ranging from 37 – 135 μg g^{-1}, and 18-50 μg g^{-1} in the 9 km off-axis sediment trap samples. There is a strong linear correlation between Pb_{HT} and FeHT in the sediment trap samples with increasing distance from active venting.

Along with Pb_{HT}, As_{HT} and Cd_{HT} correlate linearly with Fe_{HT} in the sediment trap samples. As_{HT} concentrations in the on-axis sediment traps range from 90-180 μg g^{-1} in the 2014-2015 sediment trap samples, 46-115 μg g^{-1} (2017-2018), and 100-177 (2019-2020). In the 3 km off axis sediment trap samples, the concentration of As_{HT} ranges from 9-65 μg g^{-1}, and in 9 km off axis ranges from 6 – 24 μg g^{-1}.

Cd_{HT} concentrations in the on-axis sediment trap samples have a strong linear correlation with Fe_{HT}, though this is not as strong in the off-axis sediment trap samples compared to the other hydrothermally associated elements. The concentration of Cd in the 2014-2015 on-axis sediment trap samples range from 40-60 μg g^{-1}, 10-50 μg g^{-1} (2017-2018), and 45-110 μg g^{-1} (2019-2020). In the 3 km off axis sediment traps, the Cd_{HT} ranges from 1.5-3.5 μg g^{-1} and in the 9 km off axis sediment trap samples are low and relatively constant, ranging between 0.2-0.4 μg g^{-1}.

For Pb_{HT}, As_{HT}, and Cd_{HT}, there are two separate trends (Figure 4.6) with the on-axis samples having low Pb_{HT}/Fe_{HT} and As_{HT}/Fe_{HT}, and these ratios being higher off axis. The low Pb_{HT}/Fe_{HT} and As_{HT}/Fe_{HT} ratio is interpreted as a hydrothermal component, and the higher ratios off axis suggest a scavenged component. The scavenging processes likely occur early as the Fe_{HT} normalized metal concentrations the 3 km and 9 km off-axis sediment traps are approximately the same.

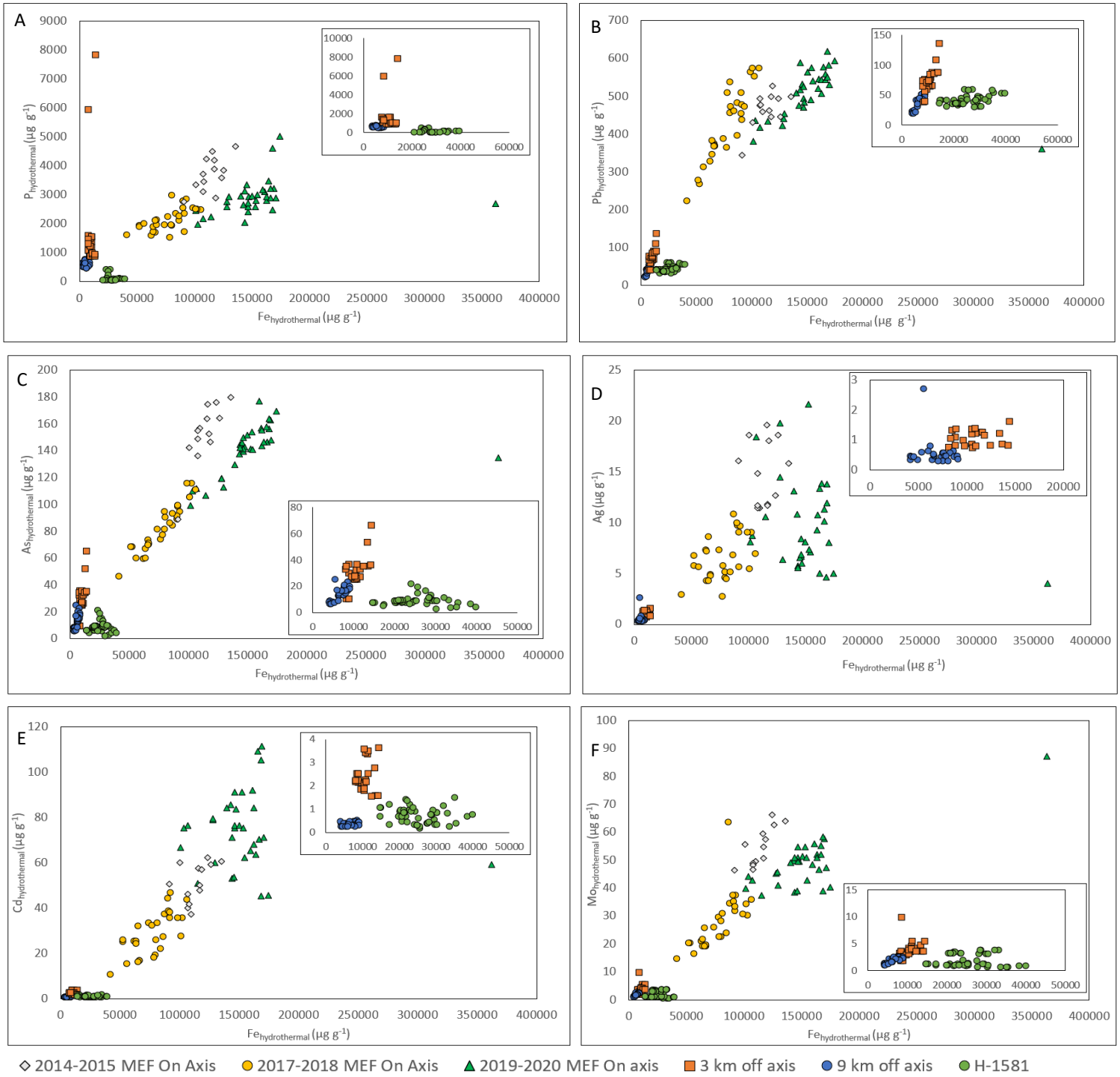

Figure 4.6 Cross plot of hydrothermal Fe versus hydrothermally associated component of scavenged element (A) P, (B) Pb, (C) As, (D) Ag, (E) Cd, (F) Mo. Insets zoom in on low elemental concentration in sample.

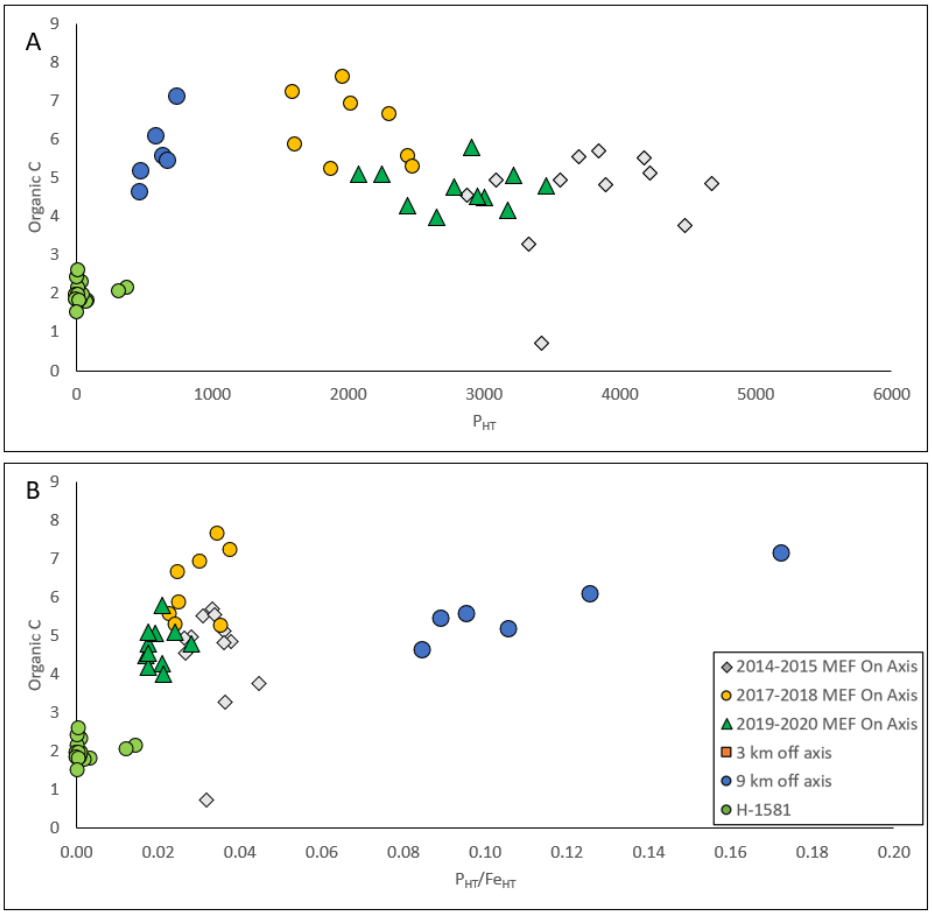

Figure 4.7 Cross plot of (A) hydrothermal P versus Organic C, (B) P_{HT}/Fe_{HT} versus Organic C

Rare earth elements are taken up from seawater onto hydrothermally derived Fe-Mn-oxyhydroxides through co-precipitation and scavenging (Rudnicki and Elderfield, 1993; Bao et al., 2008). In the buoyant plume, co-precipitation is the main mechanism for removal, and in the neutrally buoyant plume scavenging is dominant (Mitra et al., 1994). With normalization of total REE concentrations to Cascadia Basin background sediments, the spatial variation of the REE pattern changes moving away from active venting to 3 km and 9 km off axis due to changing proportions of scavenged, hydrothermal and detrital components (Figure 4.8). To describe the composition of the samples, the Ce anomaly (Ce/Ce*; Eqn. 4.2) and Eu anomaly (Eu/Eu*; Eqn 4.3) are calculated using Cascadia Basin normalized concentrations (CBN). A positive Eu anomaly is a typical signature of hydrothermal vents fluids, and a negative Ce anomaly is characteristic of seawater (German et al., 1990).

$$Ce/Ce^* = \frac{Ce_{CBN}}{(La_{CBN} * Nd_{CBN})^{0.5}} \tag{4.2}$$

$$Eu/Eu^* = \frac{Eu_{CBN}}{(Gd_{CBN} * Sm_{CBN})^{0.5}} \quad (4.3)$$

On-axis sediment traps samples from 2014-2015, 2017-2018 and 2019-2020 exhibit negative Ce anomalies, positive Eu anomalies and a slight HREE enrichment (Figure 4.8A B C). Eu data for the 2014-2015 sediment trap samples is not reported (Coogan et al., 2017). The range of colours, from light to dark, in the plots are used to differentiate between samples collected at different times of year showing that there is no temporal change in REE concentration. The Eu/Eu* in the 2017-2018 sediment trap samples ranges from 1.5-2.3 and in the 2019-2020 sediment trap samples ranges from 1.6-2.5. The Ce/Ce* in the 2014-2015 sediment trap samples ranges from 0.66-0.76, 2017-2018 samples range from 0.73-0.88, and the 2019-2020 samples range from 0.69-0.83. In the 2019-2020 sediment trap, sample 21, the darkest green line in Figure 4.8C, deviates from the pattern observed in the rest of the on-axis sediment trap samples. This sample has a very high Fe-concentration in comparison to the rest of the on-axis sediment traps, with a concentration of approximately 3.6 x 10^5 µg g^{-1}, nearly double the Fe content of the other samples from this trap. Visually, due to its colour being very red compared to the other samples that are more grey-brown, this sample appeared to have a high concentration of Fe-oxyhydroxides (as described in Section 2.2).

The REE pattern changes moving 3 km off axis. The pattern for all samples are similar except for sample 15, the darkest orange line in Figure 4.8D. This is the sample that clogged the sediment trap during collection and thus collected a large amount of material compared to the rest of the trap samples as it did not close, and likely collected water column material as it was brought up to the ship. This sample has a Ce/Ce* and Eu/Eu* that differs from the rest, at 0.78 and 1.12, respectively. There remains a slight negative Ce anomaly, ranging from 0.85-0.99, excluding sample 15. The Eu anomaly is negative for all but one sample, sample 15, ranging from 0.87-0.94. At 9 km off axis, the REE pattern is comparable to the 3 km off axis sediment trap. There remains a slight negative Ce anomaly ranging from 0.86-1.0, and a negative Eu anomaly ranging from 0.86-0.93. The relationships between Ce/Ce* and Eu/Eu* show distinct groupings based on distance from active venting (Figure 4.9), off-axis samples have higher Ce/Ce* (i.e. a larger fraction of REE scavenged from seawater) and lower Eu/Eu* compared to on-axis sediment trap samples

The sediment core, H-1581, has a HREE enrichment, a negative Ce anomaly ranging from 0.75-0.86, and a positive Eu anomaly ranging from 1.04-1.1. The REE composition of these samples lies in between on-axis and off axis sediment trap samples (Figure 4.9).

Figure 4.8 Mean Cascadia Basin sediment (Table 4-2) normalized REE plot for (A) 2014-2015 MEF On-Axis sediment trap samples, (B), 2017-2018 MEF On-Axis sediment trap samples, (C), 2019-2020 MEF On axis sediment trap samples, (D) 3 km off axis sediment trap samples, (E) 9 km off axis sediment trap samples, (F) sediment core H-1581; Plot does not include Tb as data calibration curve was not satisfactory . Only a subset of the REE's are plotted as this is all that Carpentier et al (2013) published the composition of for background sediments in the Cascadia Basin.

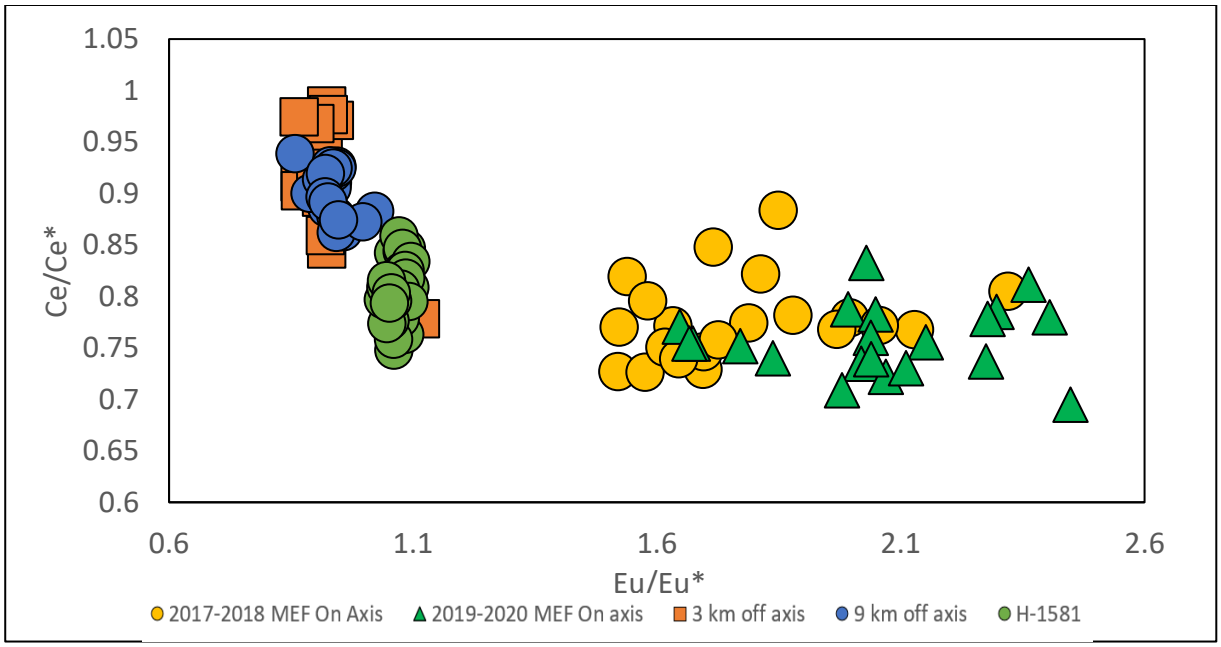

Figure 4.9 Eu/Eu* versus Ce/Ce* for on-axis sediment trap samples, 3 km off axis and 9 km off axis sediment trap samples, and sediment core H-1581.

4.2.4 Biological component

Some proportion of the material captured in the sediment trap is of biological origin. To compare each sampling period and distance from the vent, the yearly mass accumulation rate of each component is calculated and compared. In the on-axis sediment trap samples, the MAR of carbon and nitrogen are comparable between sampling periods (Table 4-6, Figure 4.10). The total yearly MAR of carbon is 1.70 g m^{-2} $year^{-1}$ in 2014-2015, 1.16 g m^{-2} $year^{-1}$ in 2017-2018 and 1.58 g m^{-2} $year^{-1}$ in 2019-2020. The flux of inorganic carbon in each sampling period is 0.36 g m^{-2} $year^{-1}$ (2014-2015), 0.22 g m^{-2} $year^{-1}$ (2017-2018), and 0.31 g m^{-2} $year^{-1}$ (2019-2020). The flux of organic carbon in each sampling period is 1.36 g m^{-2} $year^{-1}$ (2014-2015), 0.94 g m^{-2} $year^{-1}$ (2017-2018), and 1.27 g m^{-2} $year^{-1}$ (2019-2020). The nitrogen flux in the on-axis sediment traps are also comparable in magnitude, with a flux of 0.23 g m^{-2} $year^{-1}$ (2014-2015), 0.10 g m^{-2} $year^{-1}$ (2017-2018), and 0.14 g m^{-2} $year^{-1}$ (2019-2020). In the 9 km off axis sediment trap samples, the total flux of carbon Is 2.0 g m^{-2} $year^{-1}$, inorganic carbon flux of 0.63 g m^{-2} $year^{-1}$, organic carbon flux of 1.41 g m^{-2} $year^{-1}$, and nitrogen flux of 0.10 g m^{-2} $year^{-1}$. There is little difference between the N concentration in the samples collected in the on-axis sediment trap samples and those collected 9 km off-axis, suggesting there is little spatial variation in biologic flux.

Table 4-6 Total yearly carbon, inorganic carbon, organic carbon, and nitrogen fluxes for on-axis and 9 km off axis sediment traps

	Total carbon flux $g\ m^{-2}\ yr^{-1}$	Daily TC flux $mg\ m^{-2}\ day^{-1}$		Inorganic carbon flux $g\ m^{-2}\ yr^{-1}$	Daily IC flux $mg\ m^{-2}\ day^{-1}$		Organic carbon flux $g\ m^{-2}\ yr^{-1}$	Daily OC flux $mg\ m^{-2}\ day^{-1}$		Nitrogen flux $g\ m^{-2}\ yr^{-1}$	Daily N flux $mg\ m^{-2}\ day^{-1}$	
		Avg	SD		Avg	SD		Avg	SD		Avg	SD
2014-2015 On Axis	1.719	4.71	1.92	0.360	0.99	0.54	1.359	3.72	1.46	0.233	0.64	0.23
2017-2018 On Axis	1.160	3.18	1.27	0.217	0.60	0.34	0.943	2.58	0.92	0.0987	0.27	0.09
2019-2020 On Axis	1.576	4.32	2.54	0.311	0.85	0.81	1.266	3.47	1.93	0.142	0.39	0.21
9 km off axis	2.033	4.32	1.27	0.625	1.71	1.58	1.41	3.86	2.05	0.108	0.30	0.18

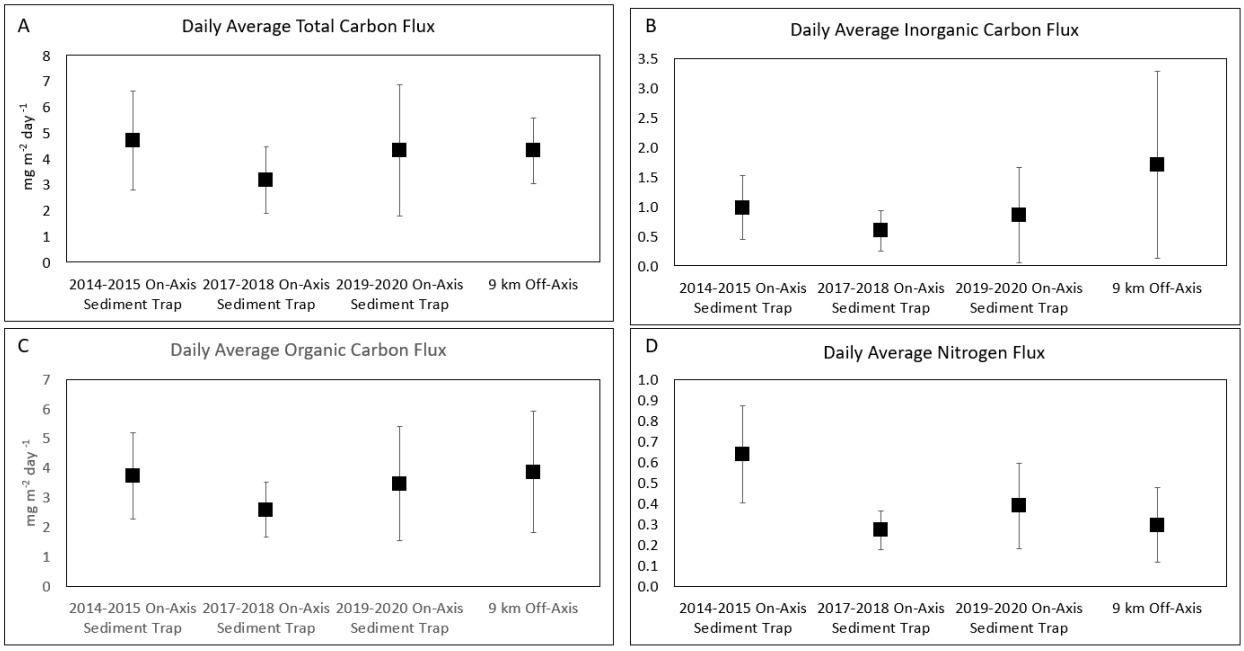

Figure 4.10 Average (± 1SD) daily mass accumulation of (A) total carbon, (B), inorganic carbon, (C) organic carbon, (D) nitrogen

4.3 Temporal variation in sediment geochemistry

A high-resolution time series of the composition of the sediments on-axis at the Main Endeavour Field, 3 km off axis, and 9 km off axis is useful for investigating changes that occur on a monthly to yearly timescale. The data presented in this section will be used to understand the stability of the chemistry and location of the hydrothermal plume in both space and time, and processes that occur in the water column that affect the sedimentation of hydrothermally derived and scavenged elements. These variations may include changes in the hydrothermal activity, or physical changes in the water column, such as changes in sediment mass accumulation rate, the amount of detrital input from the Cascadia basin, variation in the biological flux, changes in bottom currents, etc.

4.3.1 Terrigenous elements

An understanding of how terrigenous material changes over the course of the year is important, as the measured TiO_2 concentration is used to constrain the detrital component used to calculate the hydrothermal metal concentration (Section 4.1.1). Samples from the on-axis sediment traps collected between 2014 and 2020 show large variations in the concentration of Ti (400 – 1,700 μg g^{-1}) (Figure 4.11). The mass accumulation rate of Ti in the on-axis samples ranges from 0.15-3.5 μmol m^{-2} day^{-1}. The highest concentrations and mass accumulation rates of detrital elements in each sediment trap are observed between November and April. This is most evident in the 2014-2015 and 2019-2020 sediment trap samples where the changes are more systematic compared to the 2017-2018 sediment trap samples.

The terrigenous component in both the 3 km and 9 km off-axis sediment trap samples behave similarly and increase with distance from active venting (Figure 4.11). In the 3 km off-axis sediment trap samples, the Ti concentration ranges from 750-2,500 μg $g^{-1}$and the mass accumulation rate ranges from 0.1-0.6 μmol m^{-2} day^{-1}. In the 9 km off axis sediment trap samples, the concentration of Ti ranges from 1,100 - 3,300 μg g^{-1} and the mass accumulation rates 0.5-5 μmol m^{-2} day^{-1}. The lower mass accumulation rate in the 3 km off axis sediment trap samples is due to limited mass collected by the sediment trap. The increase in mass accumulation rate in the 2019-2020 on-axis sediment trap samples between November and April are observed on a slightly short timescale, from December to March, in the 3 and 9 km off-axis sediment trap samples.

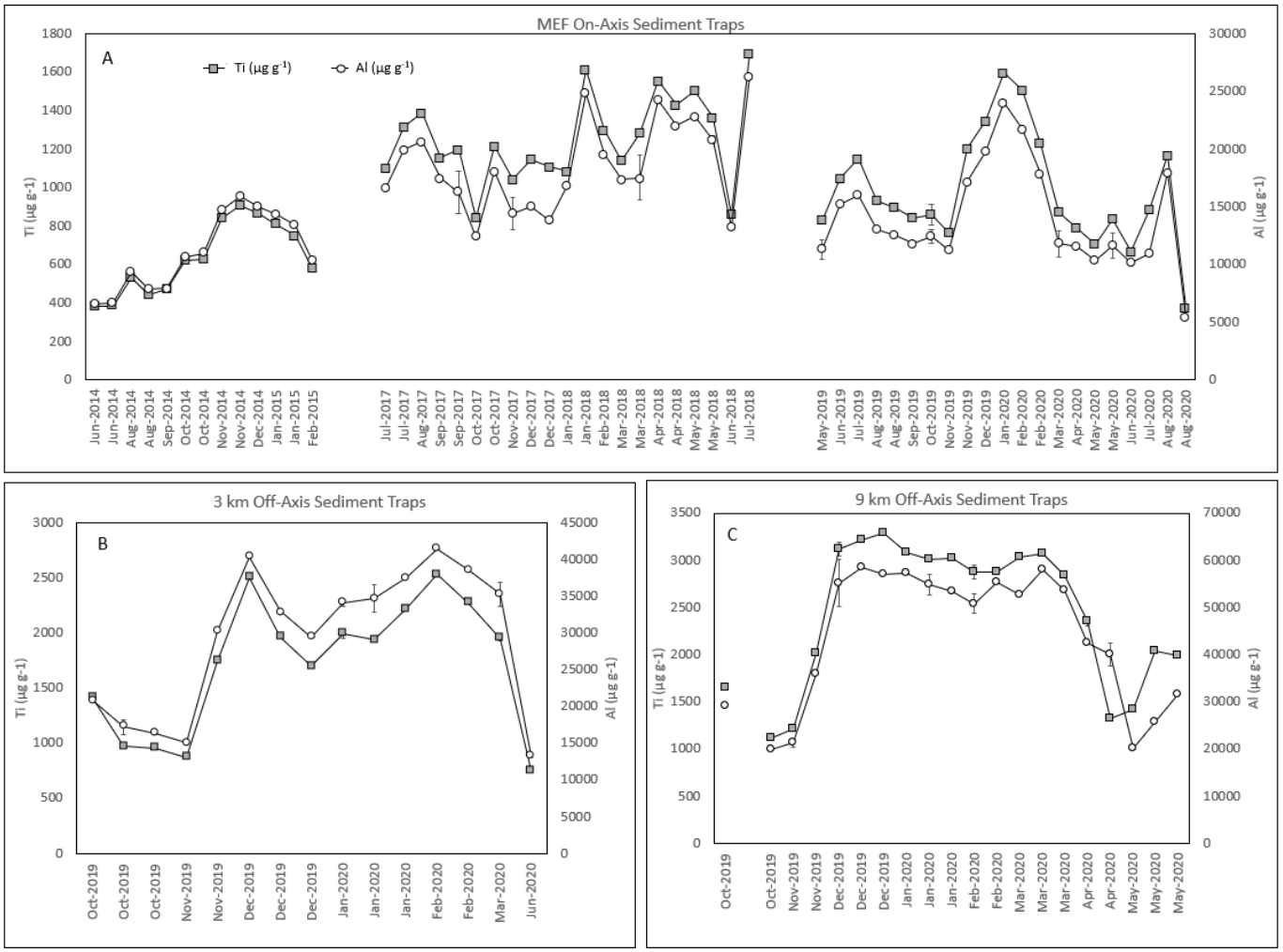

Figure 4.11 Concentrations of terrigenous derived elements Ti and Al for on-axis sediment traps (A), 3 km off axis sediment trap (B), and 9 km off-axis sediment trap (C). Concentrations are plotted at the middle date of the collection period.

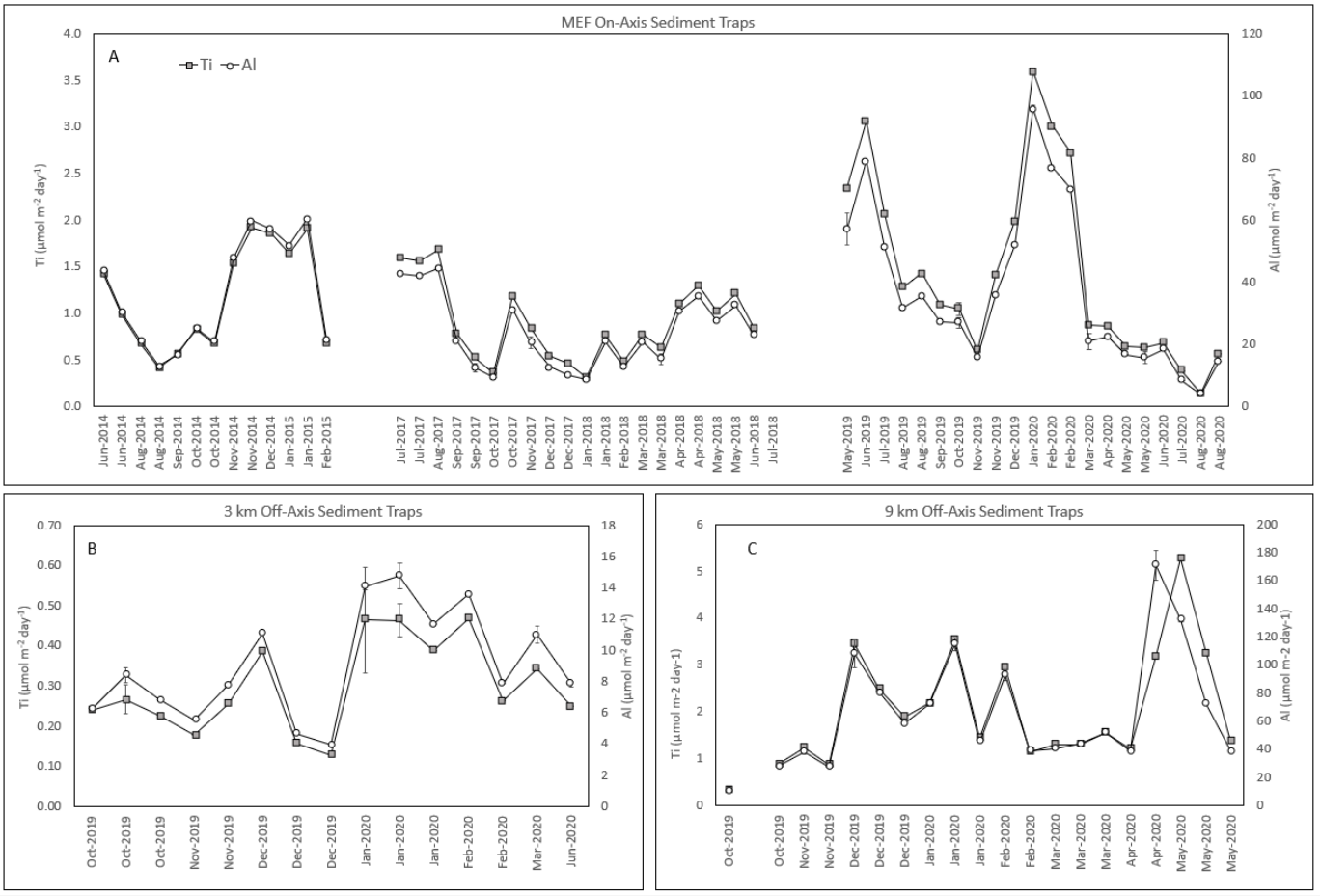

Figure 4.12 Daily mass accumulation rates for terrigenous derived elements. MAR for Ti reported on left-hand Y-axis, and Al reported on right-hand Y-axis. (A) MEF on-axis sediment traps, (B) 3 km off-axis sediment trap, (C) 9 km off axis sediment trap.

4.3.2 Hydrothermal elements

To examine the variation of the hydrothermal component in each sediment trap, the calculated hydrothermal metal concentration (Table 4-5) is used for Fe, Cu, Zn, and Mn.

Within each sampling period in the on-axis sediment traps, there is variability across the year on monthly scale in all hydrothermally derived elements (Figure 4.13). The concentration of Zn in the 2017-2018 sediment trap varies at the same frequency as Fe and Cu, though this is not observed in the 2019-2020 sediment trap samples where there is a lot more variability in the concentration of Zn. Across all three on-axis sediment trap sampling periods, there is a large amount of short time scale variability in hydrothermally derived Mn, that does not correlate with either Fe, Cu, or Zn.

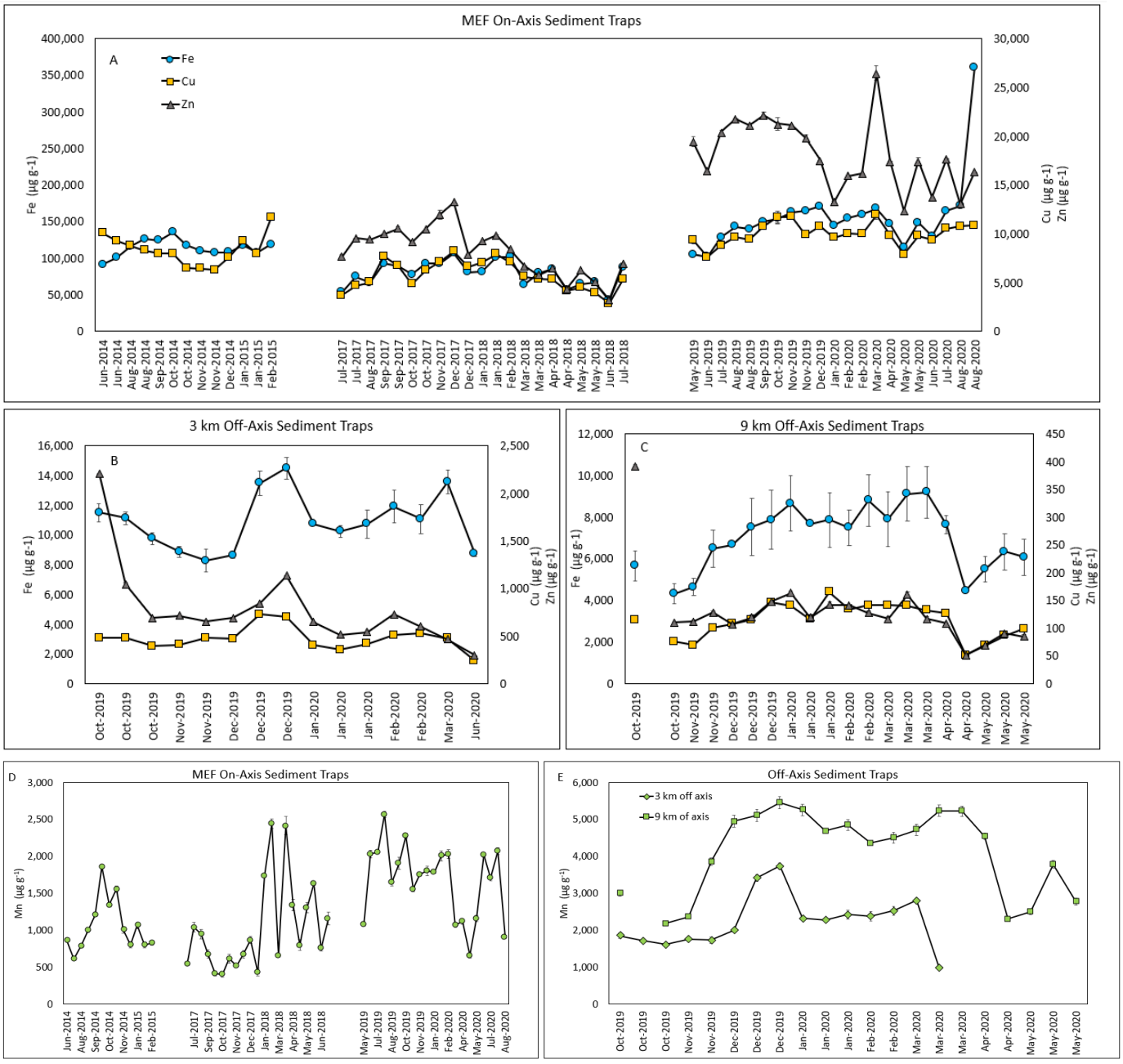

Figure 4.13 Concentration of hydrothermally derived Fe, Cu, Zn, and Mn in sediment trap samples. (A) Fe, Cu, Zn in MEF on-axis sediment traps, (B) Fe, Cu, Zn in 3 km off-axis sediment trap, (C) Fe, Cu, Zn in 9 km off axis sediment trap, (D) hydrothermally derived Mn in MEF On-axis sediment traps, (E) Mn in 3 and 9 km off axis sediment traps

The concentrations and mass accumulation rates of Ag_{HT} and Mo_{HT} appear to support a hydrothermal origin for these elements. The mass accumulation rates of Ag and Mo are comparable to the timing of changes in the mass accumulation rates of Fe_{HT}, Cu_{HT}, and Zn_{HT} in the on-axis, 3 km off-axis, and 9-km off axis sediment trap samples (Figure 4.15).

In the 3 km off axis sediment trap samples, the concentration and mass accumulation of Fe_{HT} is less variable than in the on-axis sediment trap samples. The timing of the variability in both concentration and mass accumulation rate of Fe_{HT} correlates strongly with that of Cu_{HT}, Zn_{HT}, and Mn_{HT} (Figure 4.13).

In the 9 km off-axis sediment trap samples, considering the uncertainties associated with the concentration of hydrothermal Fe after removing the detrital component, there is little observed variation. The concentrations of Fe_{HT}, Cu_{HT}, Zn_{HT} and Mn_{HT} are lowest from April-May 2020 compared to the rest of the sampling period. The timing of the variability observed in all hydrothermal elements are similar in the 9 km off axis sediment trap samples.

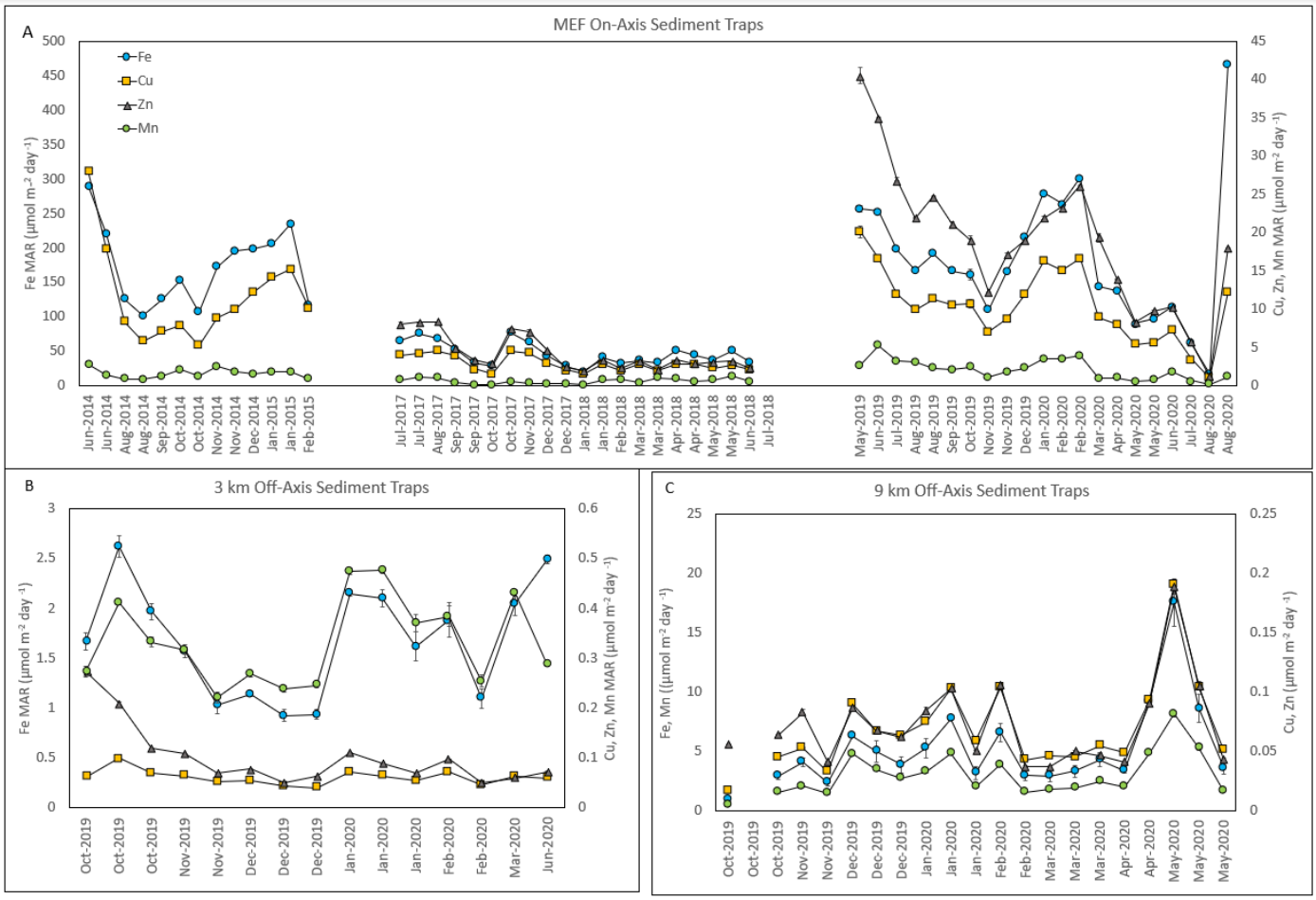

Figure 4.14 Daily average mass accumulation rate for Fe_{HT}, Cu_{HT}, Zn_{HT}, and Mn_{HT} in (A) On-axis sediment trap samples, (B) 3 km off axis sediment trap samples, (C) 9 km off axis sediment trap samples. Note that

in the 9 km off axis sediment trap, the MAR of Mn is reported on the left Y-axis, versus on the right for on-axis and 3 km off-axis sediment traps.

In the on-axis sediment trap samples, hydrothermal Fe, Cu, and Zn show similar temporal variations (Figure 4.14 A). In the 2014-2015 and 2019-2020 sediment trap samples, there is an increase in mass accumulation rates in the early Summer (June 2014 and May-June 2019) as well as the Winter (November 2014-January 2015, and November 2019-March 2020), this increase in mass accumulation rate of hydrothermal elements is associated with an increase in sample mass collected (Figure 4.1) as well as an increase in terrigenous mass accumulation rate (Figure 4.3). This is not seen in the 2017-2018 sediment trap samples, the sample masses are smaller with comparison to 2014-2015 and 2019-2020 on axis sediment trap samples, thus resulting in a smaller hydrothermal element mass accumulation rate.

The relationship between the hydrothermally derived elements differ from what is observed in the on-axis sediment trap samples, where in the 3 km off axis sediment trap samples there is a clear correlation between the mass accumulation rate of Fe and Mn (Figure 4.14), with highest mass accumulations in October 2019 and January – February 2020. The rate of change in these two hydrothermal components is comparable over the sampling period. There is little temporal change in the mass accumulation rate of Cu and Zn over the 2019-2020 3 km off axis sampling period, aside from a high unexplained Zn concentration in the first sample from October 2019. A slight increase in Cu and Zn mass accumulation rates is observed in January – February 2020, though not comparable to the magnitude of change over time to Fe and Mn.

In the 9 km off axis sediment trap samples (Figure 4.14) the mass accumulation rates of Fe, Cu, Zn, and Mn, show the same temporal variations. The change in Fe and Mn mass accumulation is approximately one order of magnitude higher than the changes in Cu and Zn, though the temporal variations are similar. There is an increase in the mass accumulation rates from January – February 2020, a lower mass accumulation rate from February – March 2020, and a large peak in hydrothermal Fe, Cu, Zn, and Mn in May 2020 that is not observed in any other sediment trap.

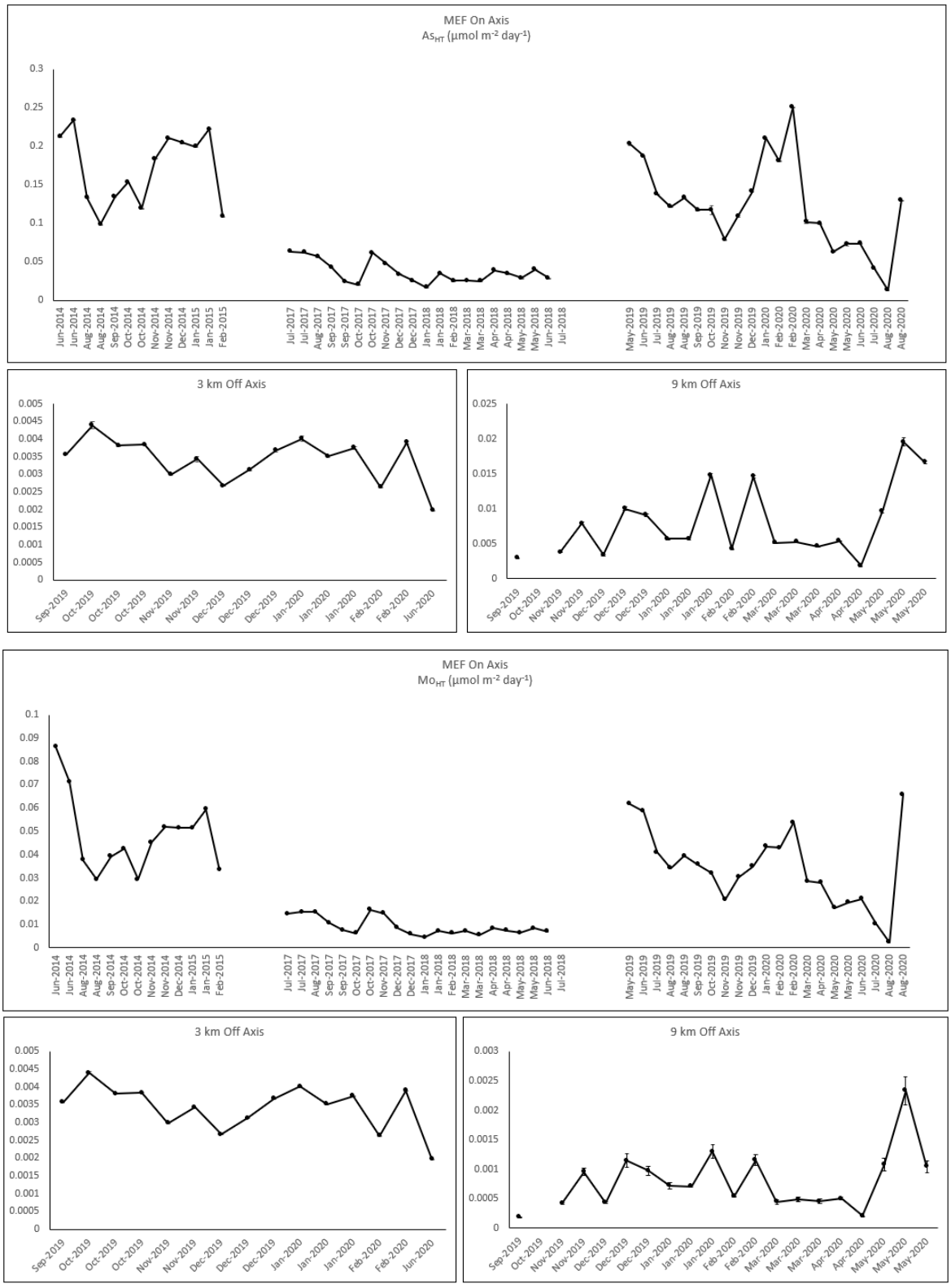

Figure 4.15 Temporal variation of the mass accumulation rate of As_{HT} and Mo_{HT} in the on-axis sediment trap samples, 3 km off axis and 9 km off axis samples.

4.3.3 Scavenged elements

The detritally corrected P mass accumulation rate in the on-axis sediments varies throughout the year, ranging from 1 – 20 µmol m^{-2} day^{-1}, with the variation correlating with the variation in the on-axis hydrothermally derived elements Fe and Cu (Figure 4.14,Figure 4.16). The detritally corrected P in the 3 km off axis sediment trap samples has two peaks in MAR. The first peak, in October 2019, correlates with a high detrital mass accumulation rate (Figure 4.16) and is not seen in the other scavenged elements. This may be a biological signal as P is not only hydrothermal or detrital in origin. The second peak, in December 2019, correlates with a high mass accumulation rate of hydrothermally derived elements Fe and Cu, and is also present in other elements (Pb, Cd, and As) that are in part hydrothermally derived, as well as scavenged.

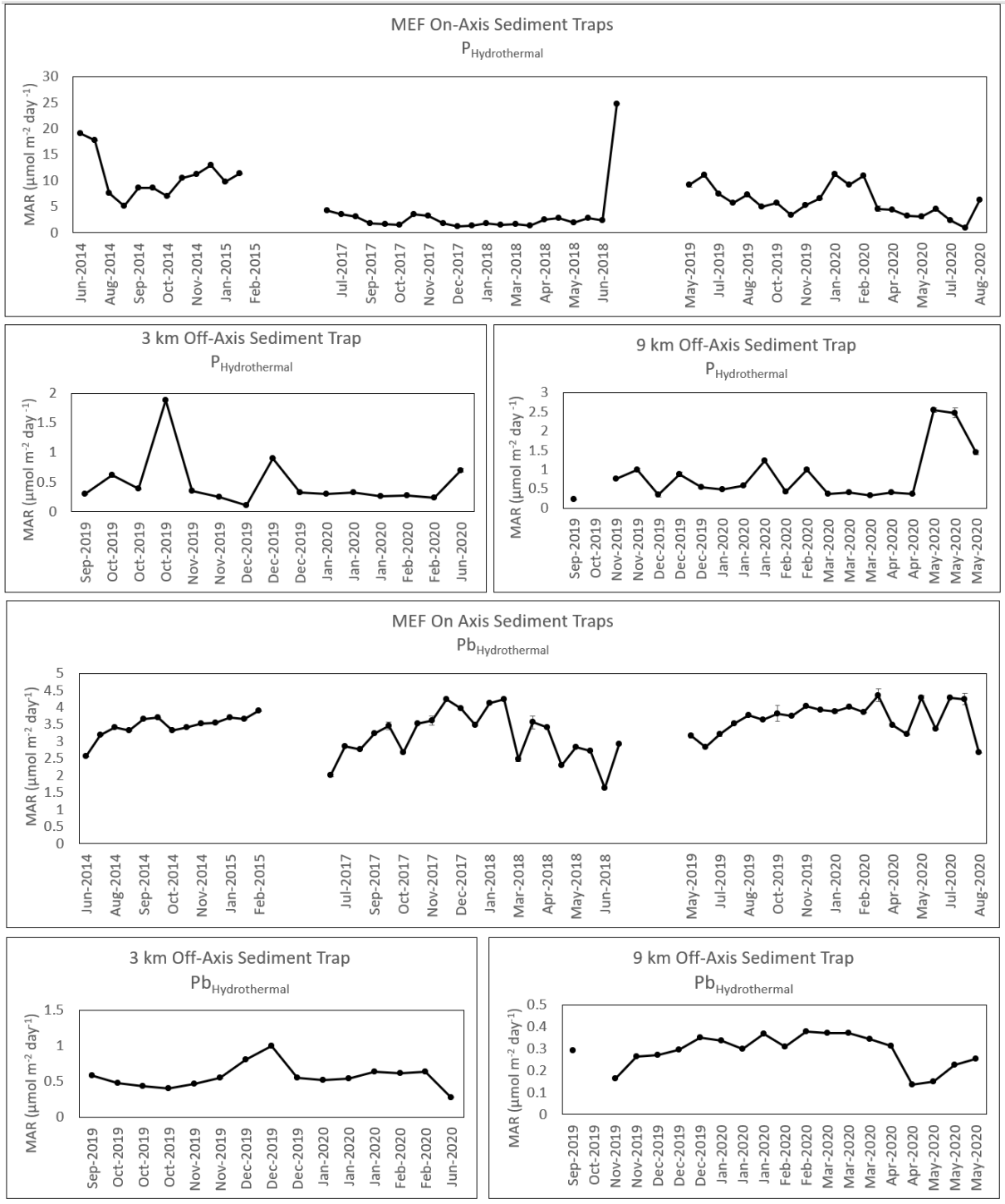

Figure 4.16 Mass accumulation rate for scavenged elements with largest concentrations (P and Pb) in the sediment trap samples from On-Axis, 3 km off-axis, and 9 km off-axis.

Table 4-7 (A) Concentration (µg g-1) (B) Mass Accumulation Rates (µmol m-2 day-1) of scavenged elements P and Pb, and partially hydrothermally derived As and Mo

	P_{HT} µg g^{-1}	Pb_{HT} µg g^{-1}	As_{HT} µg g^{-1}	Mo_{HT} µg g^{-1}
2014-2015 MEF On-Axis	2880 – 4670	345 – 525	90 – 180	46 – 66
2017-2018 MEF On-Axis	1600 – 2960	220 – 570	46 – 115	14 – 63
2019-2020 MEF On-Axis	2077 – 4808	360 – 590	100 – 177	38 – 87
3 km Off-Axis	817 – 1561	37 – 135	9 – 65	1.5 – 10
9 km Off-Axis	430 - 742	18 - 51	6 - 24	0.8 – 2.5

	P_{HT} MAR µmol m^{-2} day^{-1}	Pb_{HT} MAR µmol m^{-2} day^{-1}	As_{HT} MAR µmol m^{-2} day^{-1}	Mo_{HT} MAR µmol m^{-2} day^{-1}
2014-2015 MEF On-Axis	10.8 ± 4.0	3.45 ± 0.33	0.17 ± 0.045	0.016 ± 0.048
2017-2018 MEF On-Axis	3.34 ± 4.9	3.15 ± 0.7	0.056 ± 0.09	0.02 ± 0.047
2019-2020 MEF On-Axis	6.05 ± 2.86	3.7 ± 0.46	0.12 ± 0.06	0.04 ± 0.016
3 km Off-Axis	0.48 ± 0.42	0.57 ± 0.16	0.0034 ± 0.006	$3.5 \times 10^{-4} \pm 4.2 \times 10^{-4}$
9 km Off-Axis	0.83 ± 0.66	0.29 ± 0.07	0.0079 ± 0.005	$7.8 \times 10^{-4} \pm 4.9 \times 10^{-4}$

4.3.4 Biological elements

The biologic component (total carbon, organic carbon, inorganic carbon, and total nitrogen and P) in the sediment shows little difference in the total yearly biologic mass accumulation rates between sampling locations (on-axis and 9 km off axis) and the average daily mass accumulation rates, though there are variations on a monthly scale.

There appears to be seasonal variations in total carbon, organic carbon (OC), inorganic carbon (IC), and nitrogen (N) mass accumulation rates. On-axis mass accumulation rates of C and N are high in the samples collected during the summer (June-August), and in 2014-2015 and 2019-

2020 sediment trap samples the mass accumulation rate is high in the winter (December-February; Figure 4.17 A, C). High mass accumulation rates of organic material in the on-axis sediment trap samples correlate with high mass accumulation rate of hydrothermal material. The carbon (total, inorganic and organic) and nitrogen data for the sediment trap samples collected 9 km off axis are not at as high a temporal resolution as for the on-axis sediment trap

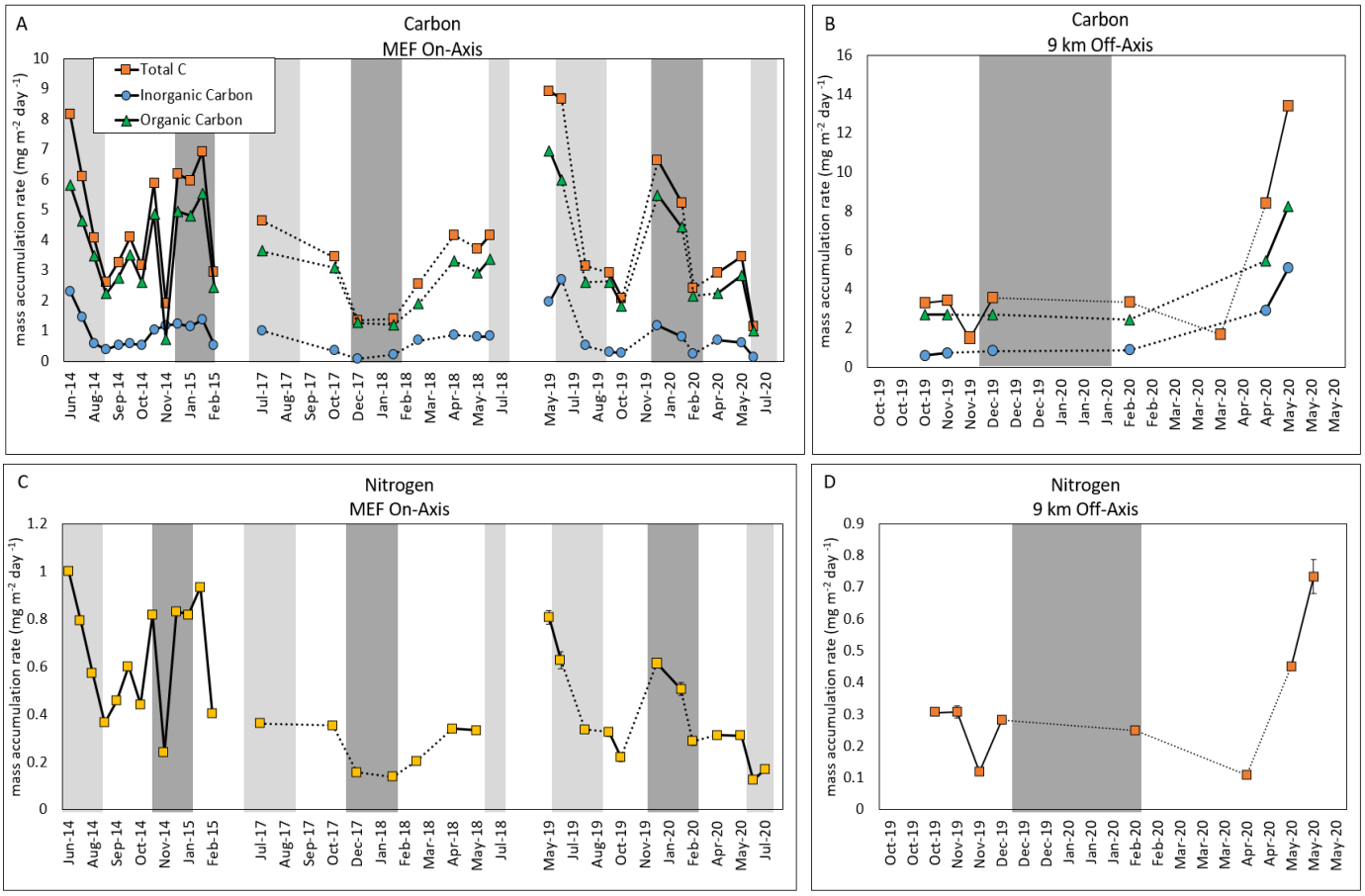

Figure 4.17 Mass accumulation rate of biological material collected in the sediment traps. (A) Total carbon, inorganic carbon, and organic carbon mass accumulation rates in the MEF on-axis sediment trap samples, (B) Total carbon, inorganic carbon, and organic carbon MARs in the 9 km off axis sediment trap samples, (C) Nitrogen MARs in the MEF on-axis sediment trap samples, (D) Nitrogen MARs in the 9 km off axis sediment trap samples. Seasons are indicated by grey bars, summer (May-August) is indicated by a light grey bar and winter (November-February) is indicated by a dark grey bar. Sample mass accumulation data are connected by a solid line if they are consecutive samples and a dotted line if there are samples that were not analyzed between them.

samples due to limited sample mass (Figure 4.17 B, D).

4.3.5 Sediment Core H-1581

4.3.5.1 ^{14}C dating of sediment core H-1581

The base of the core was dated at ~5,000 years. Due to the marine radiocarbon reservoir effect, there is an offset in the ^{14}C age between organisms that derive carbon from the

terrestrial environment and the marine environment. This is due to the fact that the ocean can only acquire atmospheric carbon at the surface during the formation of deep water in specific high-latitude regions during winter (Ascough et al., 2009). Due to the slow mixing of oceanic water masses, age corrections are regionally specific, and for planktonic foraminifera in waters in the northeast Pacific, a correction of approximately 600-800 years is normally applied (Alves et al., 2018). With the assumption that the sediment core has preserved approximately 6,000 years of sedimentation and the sediment accumulation rate has been constant, this is approximately 0.085 mm of sediment accumulation per year. Sediment accumulation rates on lobate flows in the Endeavour area were determined to range from 0.09-1.25 mm $year^{-1}$ (Clague et al., 2014a), this is a greater than or equal to the rate based on the sediment core. The higher rates derived by Clague et al. (2014) are to be expected as these largely come from near the ridge axis where the hydrothermal input, and therefore local sedimentation is likely to be larger. This suggests that the sediment preserved in the sediment core is sourced from settling water column particulate matter, and not from debris moving down the slope which would result in a higher rate of sedimentation.

4.3.5.2 Terrigenous Component

How the terrigenous component changes over time within the core is used to assess how the amount of detrital material changes over time using the sediment Ti concentration. As shown in Figure 4.18 Concentrations of Ti, Fe, Cu, Zn, and Mn in sediment core H-1581. Fe, Cu and Zn are reported as the calculated hydrothermally derived component. Ti and Mn are reported as the total concentration. Light grey line is the raw concentrations, data presented as thick black line is a calculated 5-point moving average to identify trends in concentrations. Dashed lines at 5 and 10 cm depths represent the green-brown transition zone. The highest Ti concentrations (3600 μg g^{-1}) are found at the top of the core. Concentrations of Ti range from 2,600-3,600 μg g^{-1} (average 3,080 μg g^{-1}) nearly double that in the 3 km off axis sediment trap samples (average Ti concentration 1720 μg g^{-1}), but more similar to sediment in the 9 km off axis sediment traps (1,100 – 3,300 μg g^{-1}, average 2,400 μg g^{-1}). The concentration of Ti in the sediment core is lower than the average Cascadia basin sediment concentration (7,200 μg g^{-1}). The concentration of terrigenous material varies with depth in a systematic pattern, the concentration of Ti is highest at the surface, there is a segment of lower Ti from 5-15 cm, a layer of higher concentration from 15-25 cm and another layer with lower Ti concentration from 25-43 cm.

4.3.5.3 Hydrothermal elements

The variation in the concentration of elements derived directly from hydrothermal vents (Fe, Cu, Zn, Mn, Ag, Mo and Cd) are shown as the hydrothermally derived component by removing the Cascadia Basin detrital component (Section 4.2.1). This shows the variation of the hydrothermal component preserved in the sediment core. There is no evidence from the core that there have been any significant breaks in hydrothermal activity over the last ~6,000 years; however, processes such as bioturbation and diagenesis can smooth out primary source variability. As will be discussed in Section 5.3, Zn, Mn, Ag and Cd, while hydrothermal in origin

cannot be used to discuss hydrothermal elements over time due to diagenetic remobilization that can occur in the sediments (Figure 4.19).

The concentration of hydrothermally derived Fe ranges from 14,800 – 29,000 μg g^{-1} (average concentration 25,890 μg g^{-1}), which is 30-55% of the total Fe in the sediment. With comparison to the concentration of hydrothermally-derived Fe in the sediment trap samples, the Fe concentration is higher than that in the 3 km off axis sediment trap samples (8,000-14,500 μg g^{-1}), but lower than in the on-axis sediment trap samples (42,000 – 462,000 μg g^{-1}). The top 5 cm of the core has a constant concentration of Fe (25,000 μg g^{-1}) , above the redox transition zone from ~6-10 cm. Below this, the Fe concentration decreases to a minimum of 14,800 μg g^{-1}, and shows two further cycles of increasing and decreasing concentrations progressively deeper in the core (Figure 4.18 B). The concentration of hydrothermal Fe in the sediment is inversely proportional to the concentration of Ti.

The concentration of hydrothermally derived Cu in the sediment core ranges from 110-280 μg g^{-1} (average 184 μg g^{-1}) (Figure 4.18 C). The high end of the range of sediment core Cu concentration is similar to the low end of the 3 km off axis sediment trap samples (237-730 μg g^{-1}), and closer to the concentration of hydrothermally derived Cu in samples from the 9 km off axis sediment trap which have an average Cu concentration of 111 μg g^{-1} (range 51-165 μg g^{-1}). Cu in the sediment core appears to behave similarly to Fe, with Cu/Fe being nearly constant with depth. In the upper 6 cm of the core, the Cu concentration is ~ 150 μg g^{-1}, and then it increases to a maximum concentration from 6-12 cm. Below this, Cu goes to a minimum at ~20 cm, and shows two further cycles of increasing and decreasing concentrations progressively deeper in the core. In the sediment core, Zn behaves differently to Fe and Cu (Figure 4.18 D), with a higher concentration in the surface and a decrease in concentration with depth. The concentration of Zn_{HT} in the sediment core, similarly to Cu_{HT} is comparable to the 9 km off-axis sediment trap sample concentrations.

In the sediment core, the removal of the terrigenous component for Mn results in a negative value at depth, which suggests that the terrigenous component is over-estimated, or the core has lost some detrital Mn. To avoid reporting negative concentrations, Mn is presented as the raw concentration in Figure 4.18. The surface sediments have the highest Mn concentrations, of up to 4,057 μg g^{-1}, and this decreases to 860 μg g^{-1} at 5 cm below the surface (at the top of the brown-green transition). The deeper samples have much lower Mn concentrations ranging between ~600-800 μg g^{-1}, with no discernable cyclicity with depth. Compared to Cascadia Basin sediments, with a Mn concentration of ~1,160 μg g^{-1}, the surface sediments are enriched and sediments below the brown-green transition zone are depleted in Mn. The utility of using Mn as a hydrothermal tracer will be discussed further, as it appears that Mn is remobilized due to changing redox conditions within the sediments.

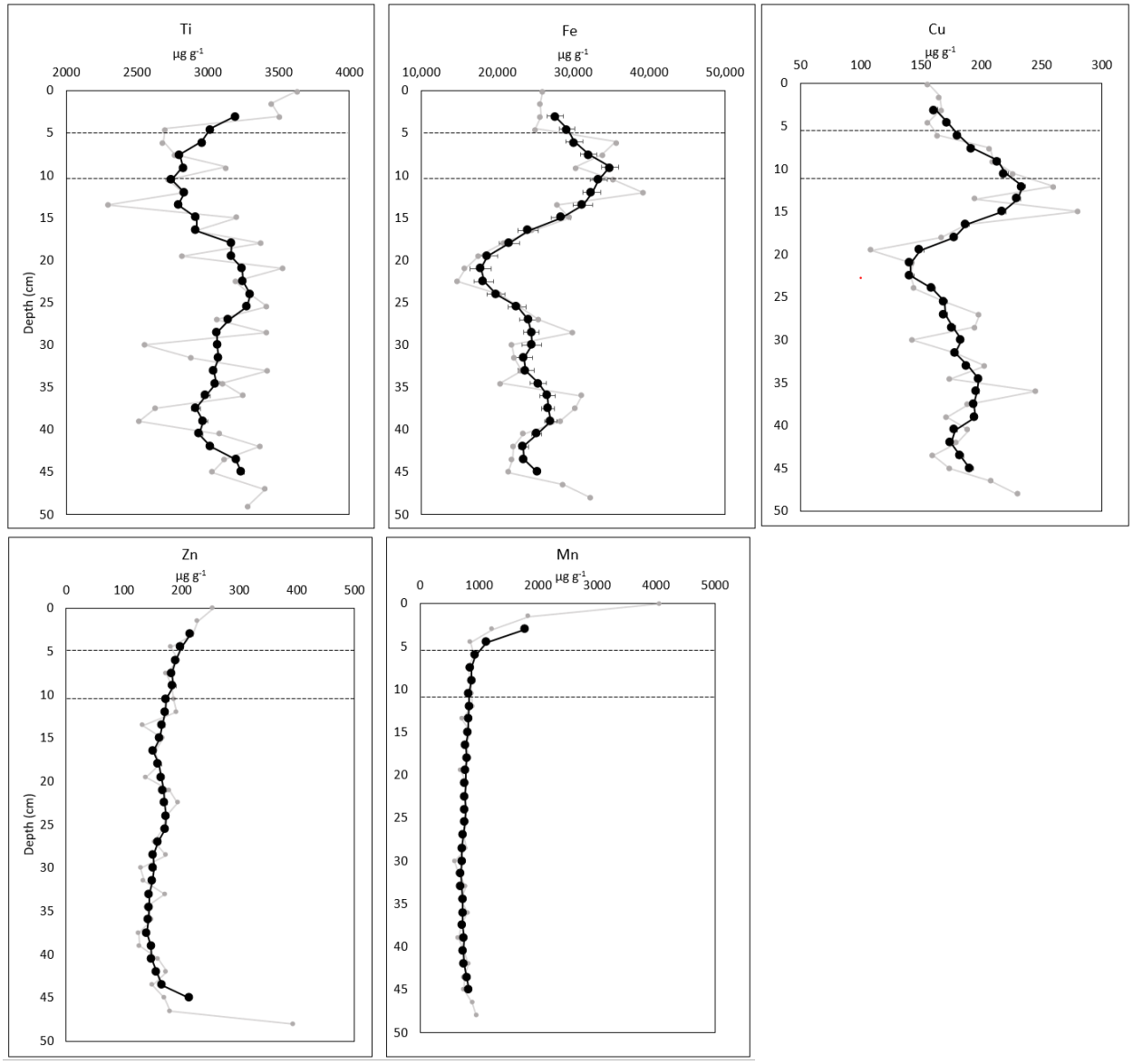

Figure 4.18 Concentrations of Ti, Fe, Cu, Zn, and Mn in sediment core H-1581. Fe, Cu and Zn are reported as the calculated hydrothermally derived component. Ti and Mn are reported as the total concentration. Light grey line is the raw concentrations, data presented as thick black line is a calculated 5-point moving average to identify trends in concentrations. Dashed lines at 5 and 10 cm depths represent the green-brown transition zone.

4.3.5.4 Scavenged and hydrothermally derived elements on 1000-year time scales

In hydrothermally derived sediments, the behaviour of elements scavenged by Fe-bearing particles in the plume should behave similarly to the hydrothermal Fe in the sediment core – not necessarily – it depends how the scavenging occurs over time (and how they are mobilised by diagenesis). Scavenged elements show much lower element$_{HT}$/Fe$_{HT}$ ratios in X compared to the 3 km off-axis sediment trap samples (Section 4.2.4). As observed in Figure 4.19,

there are gradients in the concentration of elements at approximately 5-10 cm of depth in the sediment core, with either a concentration low or high. Due to the concentration gradients occurring above, at, or below the brown-green transition zone, the concentration of these elements (P, Cd, Co, Tl, U, and Mo; Figure 4.18) suggest that post-depositional diagenetic changes that have occurred, in the sediments, which will be discussed further in Section 5.3.

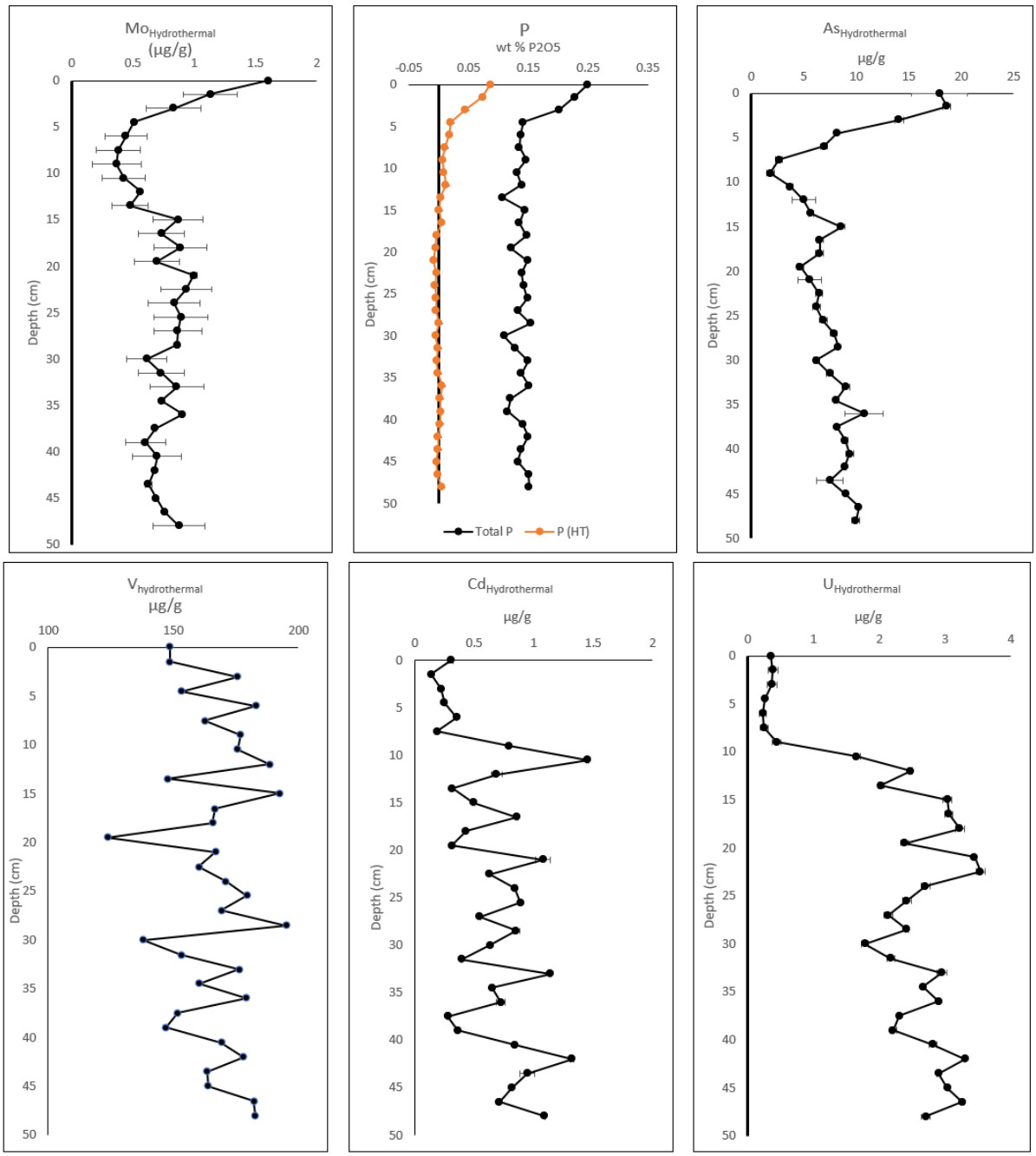

Figure 4.19 Concentrations of scavenged elements V, Cd, Co, Tl, U, and Mo. These elements are identified as those likely being altered by post-depositional changes based on comparison with hydrothermal Fe and pore fluid chemistry.

4.3.5.5 Changes in the biological component on 1000-year time scales

In the sediment core, the concentration of total carbon changes very little with depth, ranging between 21,500 – 27,200 µg g^{-1} with one sample with high total carbon at the base of the core with a concentration of 35,000 µg g^{-1}. Due to the high uncertainty on duplicate samples of measured total carbon (e.g. as seen in the sample at 12 cm depth; Figure 4.20) there may be less true variation in total carbon contents. The concentration of organic carbon ranges from 16,000 – 26,600 µg g^{-1}, and the concentration of inorganic carbon ranges from 4160 – 9290 µg g^{-1} (Figure 4.20). Organic Carbon:Nitrogen (OC:N) ratios ranging from 9-14, higher than the Redfield ratio (6.6), suggesting mobilization of some N during degradation of the organic material within the sediment core.

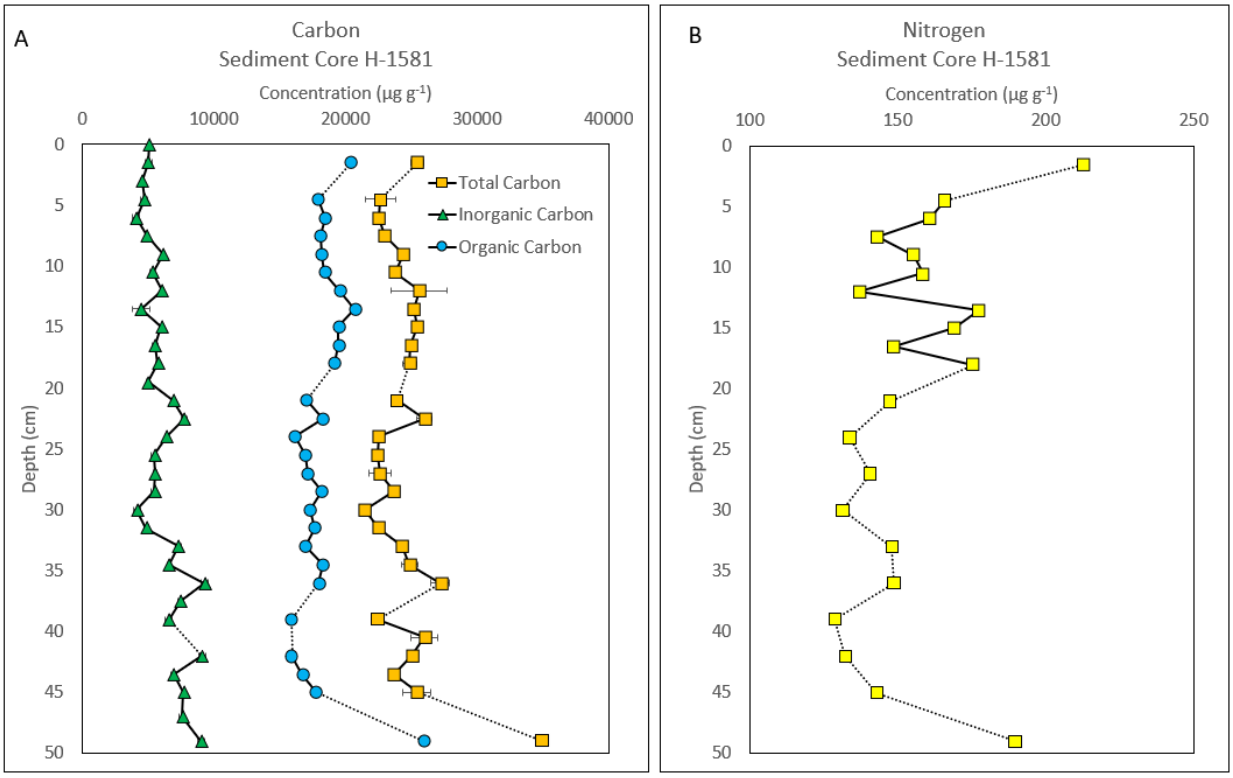

Figure 4.20 Sediment core biological components (A) total carbon, inorganic carbon, and organic carbon, (B) nitrogen. Dashed line is an interpolation between samples analyzed and those not due to mass limitations.

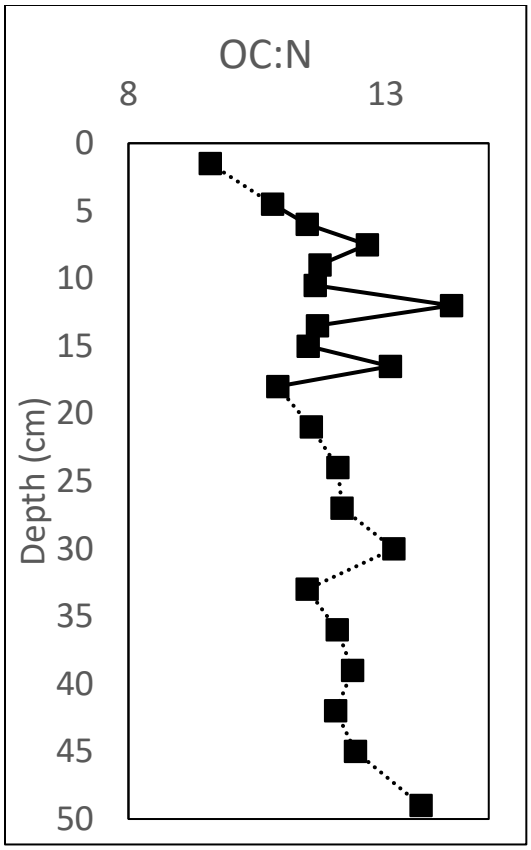

Figure 4.21 Organic C:N ratio in the sediment core

4.3.5.6 Pore fluid geochemistry

The chemistry of the pore fluids was determined to assess for post depositional changes in the sediment core (Table 4.8). An enrichment in the element in the pore fluid compared to deep Pacific seawater could be indicative of leaching of elements into the pore fluids at the time of collection.

Hydrothermally derived elements (Fe, Cu, Zn and Mn) have pore fluid concentrations that are higher than deep Pacific seawater. The concentration of Fe in the pore fluids ranges from 16-400 nmol kg^{-1}, two orders of magnitude higher than the concentration of Pacific Ocean Fe at 2000 – 3000 m depth (0.6-0.7 nmol kg^{-1}; Martin et al., 1989). This large variation could be due to a contamination by particles smaller than the 0.2µm filter. The concentration of pore fluid Fe in the top 3 cm of the sediment core is constant and is the lowest concentration, with increasing concentration with depth (Figure 4.22A). The concentration of Cu in the pore fluid ranges from 131-1,246 nmol kg^{-1}, higher than seawater concentrations of ~4 nmol kg^{-1} (Bruland, 1980). The concentration of pore fluid Cu is highest in the surface sediments and decreases linearly with depth to 10 cm, where the concentration is lowest and then remains relatively constant to the base of the core (Figure 4.22B). The concentration of Zn in the pore fluids ranges from 16-110 nmol kg^{-1}, higher than seawater concentration of 8 nmol kg^{-1} (Bruland, 1980; Figure 4.22C). The concentration of Mn in the pore fluids is very high compared to the

other hydrothermally derived elements, ranging from 606-4,865 nmol kg^{-1}, and the concentration of Mn in seawater is 0.1-0.2 nmol kg^{-1}(Landing and Bruland, 1980). The minimum concentration of pore fluid Mn is at the surface of the sediment core, increasing to a maximum at 5 cm, the top of the brown-green transition zone. Below this, the concentration of Mn is relatively constant with depth (Figure 4.22D).

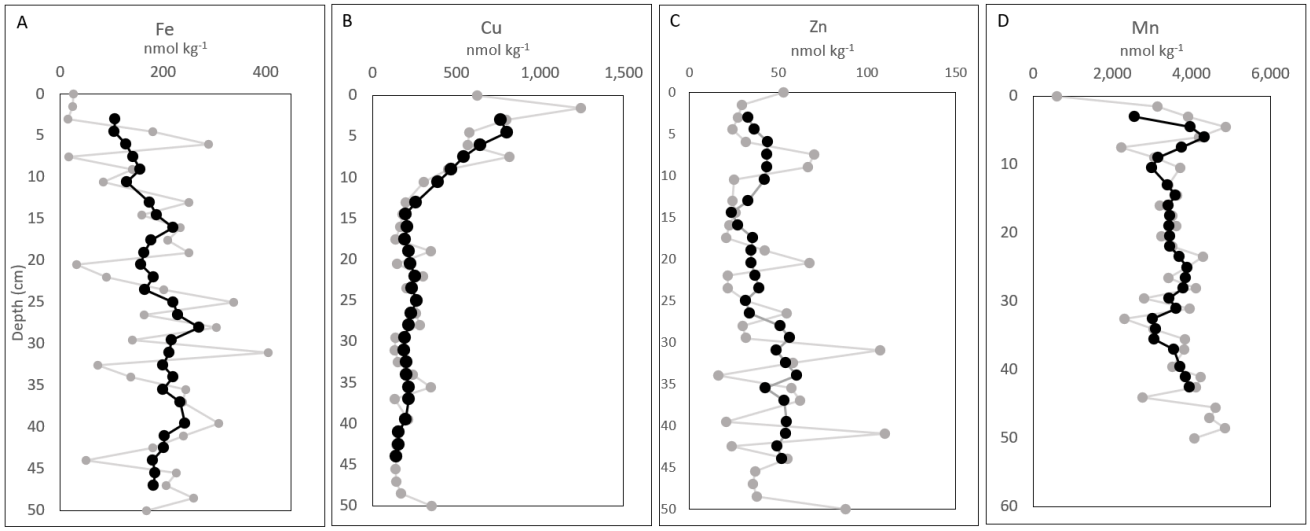

Figure 4.22 Concentration of pore fluid Fe, Cu, Zn, and Mn in the sediment core. Black points are a calculated 5 point moving average, light grey is the raw concentration data. Variability in raw concentration data may be due to contamination by particles <0.2 µm that passed through the filter. Seawater concentrations obtained from MBARI, sources above: Fe 0.6-0.7 nmol kg^{-1}, Cu ~4 nmol kg^{-1}, Zn of 8 nmol kg^{-1}, Mn 0.1-0.2 nmol kg^{-1}.

Other elements, including those that are scavenged by hydrothermally derived particles (Section 4.2.3) can be grouped by pore fluid behaviour above and below the brown-green transition zone, and with comparison to seawater concentration. The first group of elements is Cd, V, Co, and Tl, which have pore fluid concentrations that peak above or within the brown-green boundary and have low concentrations at the surface and at depth, similarly to Mn (Figure 4.23). The average concentrations of these elements are higher than seawater. In the pore fluid, the concentration of V ranges from 6-490 nmol kg^{-1} (average 97 nmol kg^{-1}), the concentration of V in seawater is 36.6 nmol kg^{-1}. On average the concentration is higher than seawater, and there is a peak in concentration is at 7 cm depth in the core, within the brown-green transition zone. The concentration of Cd is only enriched relative to seawater within the brown-green transition zone, a concentration of 1.47 nmol $kg^{-1}$and at depth concentrations are below the detection limit. Similar to Cd, Tl has a maximum concentration within the brown-green transition zone and is near the detection limit at depth. Cobalt is highest in the surface sediments above the brown-green transition zone, and decreases to a constant concentration of around 1 nmol kg^{-1} at depth.

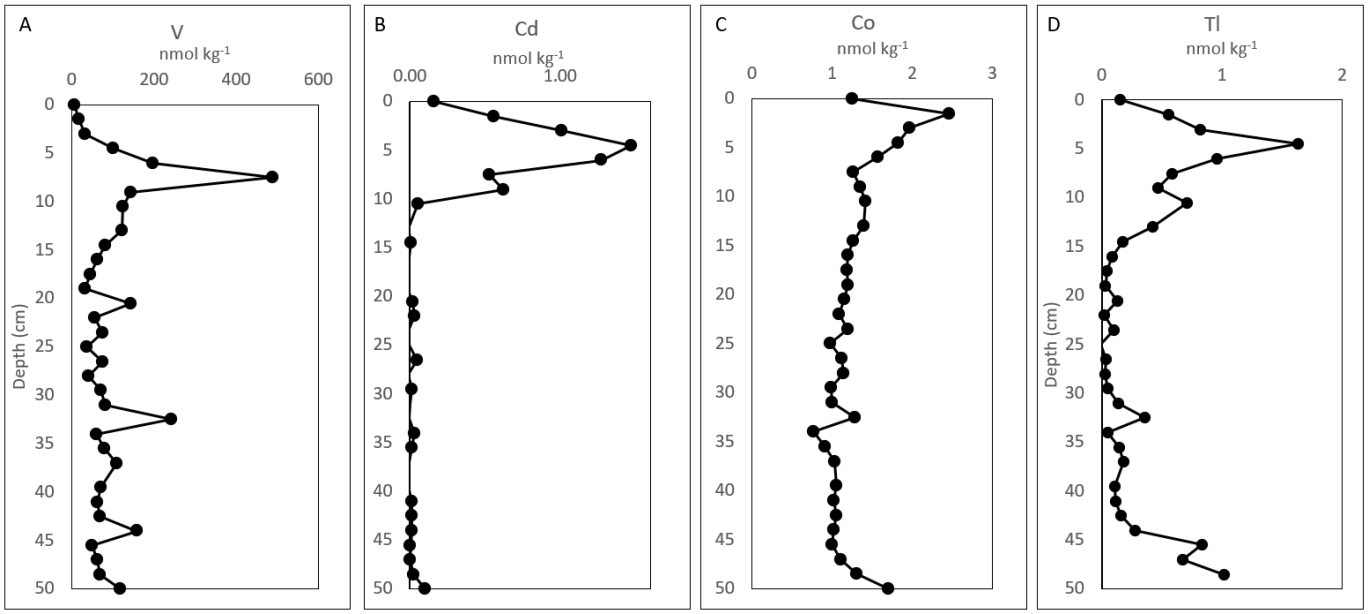

Figure 4.23 Concentration of pore fluid V, Cd, Co and Tl in the sediment core. Seawater concentrations obtained from MBARI: V 36.6 nmol kg^{-1}, Cd 810 pmol kg^{-1}, Co 13 pmol kg^{-1}, Tl 64 pmol kg^{-1}

Mo and U are depleted in the pore fluids in the surface sediments and are higher at depth (

Figure 4.24). The concentration of U ranges from 0.5 – 8 nmol kg^{-1}, the concentration is low to 10 cm, the base of the brown-green transition zone, and then increases to a concentration that is relatively consistent to the base of the sediment core. The concentration of U in seawater is 13.6 nmol kg^{-1}, the sediments pore fluid is depleted in U with respect to seawater. The concentration of Mo ranges from 3-50 nmol kg^{-1}, and it is low in the surface sediments to ~10 cm and then increases continuously with depth. The concentration of Mo in seawater is 106 nmol kg^{-1}, the pore fluid is depleted in Mo with respect to seawater.

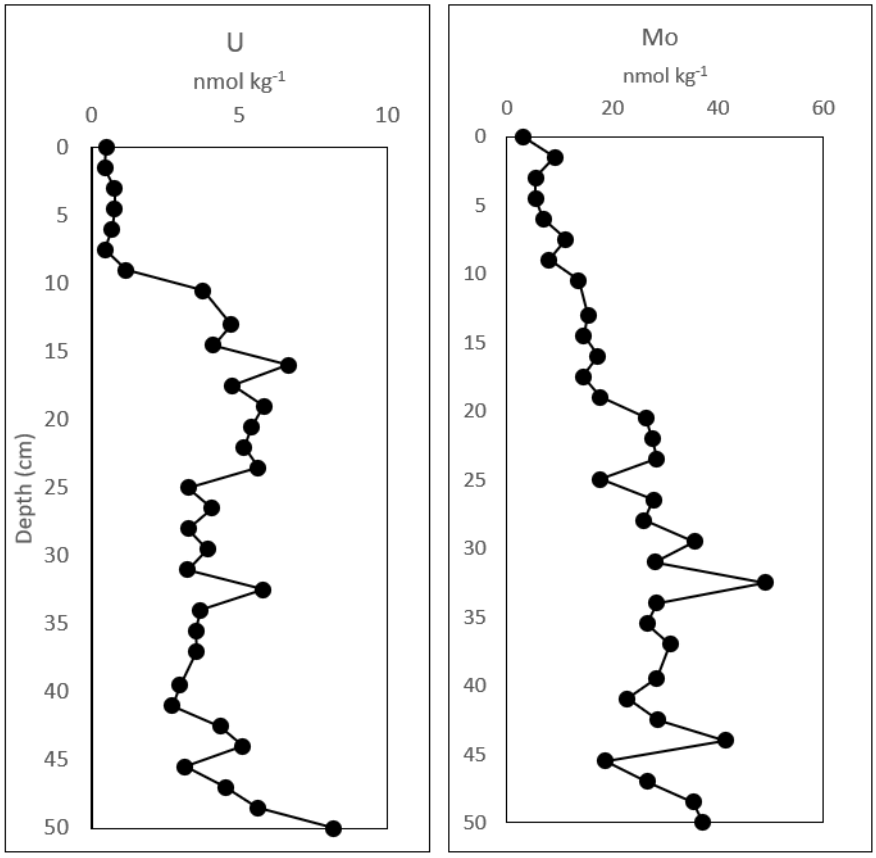

Figure 4.24 Concentrations of pore fluid U and Mo in the sediment core. Seawater concentrations obtained from MBARI: U 13.6 nmol kg^{-1}, Mo 106 nmol kg^{-1}

Table 4-8 Comparison of the concentration of elements in the pore fluid with deep Pacific seawater concentrations

Element	Pore fluid concentration (nmol kg^{-1})	Deep Pacific Seawater concentration (nmol kg^{-1})
Fe	16-400	0.64
Cu	132 – 1245	4.26
Zn	16 – 110	8.38
Mn	606 – 4,865	0.15
V	6 – 490	36.6
Co	0.7-2.4	0.013
Mo	3 – 50	106
U	0.52-83	13.4

4.4 Summary

The hydrothermally derived elements in the sediments collected by the sediment traps are diluted by the input of Cascadia Basin terrigenous sediment. To interpret the hydrothermal component of the sediment, the Cascadia Basin background sediment is subtracted from the bulk concentration of these elements. Sediment trap samples from on-axis at the Main Endeavour Field, 3 km off-axis and 9 km off axis, have concentration of hydrothermally derived elements (Fe, Cu, Zn) that are highest on-axis, lower in the 3 km off-axis sediment traps, and lowest in the 9 km off-axis sediment trap samples. and lowest in the 3 km off axis sediment trap samples, and higher in the 9 km off axis sediment trap samples. The mass accumulation rates of hydrothermally derived elements are highest on-axis sediment trap samples, lowest in the 3 km off-axis sediment trap samples, and higher than the 3 km off-axis samples in the 9 km off-axis sediment trap samples. This is believed to be due to placement of the 3 km off axis sediment trap. We then see hydrothermally derived Mn increasing with distance from the vent. The temporal variation of hydrothermally derived elements reveals large variations throughout the yearly sampling periods in the on-axis sediment trap samples, and the concentrations and mass accumulation rates of Fe, Cu, and Zn are closely correlated. Elements that are scavenged by the hydrothermally derived particles are shown to have a close correlation with the concentration of Fe.

Sediment core, H-1581, that was collected 2.8 km from the ridge axis has lower concentrations of all investigated elements, except for Fe, than samples from the sediment trap at a similar distance from the vents. The pore fluid chemistry in this core shows high concentrations of hydrothermally associated elements relative to seawater concentrations, and various behaviours above or within the brown-green transition zone. This reveals the potential for post-depositional changes that have occurred over the past 6,000 years of sedimentation.

5 Discussion

The geochemistry of sediment trap samples collected on-axis at the Main Endeavour Field, 3 km off axis, and 9 km off axis, as well as a sediment core collected 2.8 km NNW of active venting were presented in Section 4. The spatial variation of sediment trap geochemistry will be discussed in Section 5.1, specifically to address what processes are controlling the chemistry and mass accumulation rates of the hydrothermally derived components of the sediments. The temporal variation of the hydrothermally derived component is discussed in Section 5.2. The sediment traps were in place for less than a year, and the variation observed in the hydrothermally derived component can be used to understand how the system is behaving on a short timescale. The variation in the concentration and the flux of the hydrothermally derived elements can be used alongside terrigenous and biological components to understand how the proportions of each component are changing over sampling periods. The short-term temporal variation is used as a comparison to the geochemistry of the longer time series of 6,000 years of sedimentation on the west flank of the Endeavour Ridge and is discussed in Section 5.3. A comparison to the geochemistry in the sediment trap samples and the sediment core can be used to evaluate the utility of hydrothermal sediment cores as reliable records of hydrothermal activity over longer time scales will be discussed in Section 5.4.

5.1 Spatial variation in sediment trap geochemistry

This section discusses the spatial variation in the geochemistry of the sediment trap samples that were collected at the Main Endeavour Field, 3 km off axis, and 9 km off axis. The spatial data (Section 4.2) provides a framework to answer the following question “what processes control the chemistry and mass accumulation rates of the hydrothermally derived component of the sediments?”. This is divided into the processes occurring near active venting

in the buoyant plume, and processes that persist with distance from the vents in the neutrally buoyant plume.

5.1.1 Rapidly precipitated hydrothermal elements - Fe, Cu, Zn

When hot hydrothermal fluids mix with cold oxygenated seawater, there is rapid precipitation of Fe-sulfide minerals (e.g. pyrite, Findlay et al. 2019). Copper and zinc precipitate almost instantaneously as chalcopyrite and sphalerite (Feely et al., 1992). Then the formation of Fe-oxyhydroxides occurs rapidly in the buoyant plume after the formation of sulfides, which aggregate and coagulate into larger particles and fall out of the hydrothermal plume (Field and Sherrell, 2000; Klar et al., 2017). Cu and Zn are also associated with Fe-oxyhydroxide phases as it is believed that co-precipitation and sorption reactions are occurring during Fe-oxyhydroxide mineral formation in the buoyant plume (Dunk and Mills, 2006).

In the sediment trap samples, the main control on the chemistry and the mass accumulation are the processes controlling particle formation and deposition. The early formation of particles in the hydrothermal plume are controlled by factors including the composition of the high-temperature fluid, the fluid flux, chemical and biological processes that transfer elements into and out of the particulate phase, and physical oceanographic conditions controlling the movement of the plume**.**

The overall sediment mass accumulation (

Table 4-1), and the mass accumulation rate of hydrothermal Fe, Cu, and Zn are highest in the on-axis sediment trap samples due to the proximity to active venting (Table 4-5; Figure 4.5). The on-axis sediment traps collect the sulfides and Fe-oxyhydroxides that are quickly deposited after deposition from the buoyant plume, as well as biological, and detrital material from the overlying water column. As presented in Chapter 4, the predominant composition of the on-axis sediment traps is hydrothermal in origin. Very few other sediment trap studies have been done at the Endeavour hydrothermal vent field, Dymond and Roth, (1988) placed a sediment trap beneath the plume near the High Rise vent field and collected 25 ± 6 g $year^{-1}$ m^{-2}, which is comparable to that collected at the Main Endeavour Field (

Table 4-1).

With distance from active venting, the concentration and mass accumulation of hydrothermally derived elements decreases rapidly. This is due to progressive dilution of the hydrothermal plume with distance from the active vents, which occurs due to the fallout of particulate matter in the area surrounding the vent as well as increasing dilution of the hydrothermal plume with further mixing with ambient seawater. With hydrothermal plume dilution, the mass accumulation of hydrothermal Fe, Cu, and Zn (Table 4-5) decreases from the highest in the on-axis sediment trap samples, to lowest in the 9 km sediment trap samples (Figure 4.4). However, unpredictably, hydrothermal Fe, Cu, and Zn in the 3 km off axis trap samples is lower than that in the 9 km off axis sediment trap samples (Figure 4.4). This is unexpected as the mass accumulation should decrease with distance; however, in terms of overall sediment mass accumulation, the 3 km off axis sediment trap collected only a very small amount of sediment (Table 4-5). The lower sediment mass accumulation in the 3 km off-axis sediment trap could be the result of the sediment trap clogging as the mass accumulation rate of both hydrothermal and detrital component are low. If it were solely a decrease in the hydrothermal component, it could be explained by variability in the location of the trajectory of the neutrally buoyant plume. However, this wouldn't be accompanied by a decrease in the detrital component as well.

The decrease of both the concentration and mass accumulation rates of hydrothermal elements in the off-axis sediment trap samples compared to on-axis sediment trap samples is consistent with rapid deposition of sulfides in the area proximal to the vents (Hrischeva and Scott, 2007). Mineralogical and geological studies in the sediments (e.g. Hrischeva and Scott, 2007) have shown that the Cu and Zn in the sediments away from the vents are deposited in both sulfide and Fe-oxyhydroxide hosted minerals. A linear correlation between Fe_{HT} and Zn_{HT}, and Fe_{HT} and Cu_{HT} in each of the sediment trap samples (on-axis, 3 km off-axis, and 9 km off-axis) supports the presence of sulfide and Fe-oxyhydroxide minerals in each; though there is a non-linear decrease between sediment trap samples with distance (Figure 4.4, Figure 4.5). The

deposition of sulfide and Fe-oxyhydroxide minerals is the primary process controlling the fate of these elements in the hydrothermal plume. as a primary process controlling the fate of these elements in the hydrothermal plume. The faster decrease in Zn_{HT} and Cu_{HT} concentration with distance compared to Fe_{HT} is expected as the sulfide bearing minerals that are enriched in Cu and Zn in the near-vent sediments are larger (1-70 µm in diameter) and denser than the colloidal Fe-oxyhydroxide particles that are predominant in the neutrally buoyant plume (Feely et al., 1994). This size and density difference will lead to differential sedimentation rates leading to changing particulate composition with distance from the vent (Feely et al., 1994; Hrischeva and Scott, 2007). Other processes that have been suggested include mineral dissolution and biological repackaging, that can impact the sedimentation of hydrothermal particulate matter between the on-axis sediments with distance from active venting (Hrischeva and Scott, 2007). In the on-axis sediment trap samples, there is a correlation between hydrothermal and detrital input, which suggests that the controls on the hydrothermal component may not be solely controlled by the formation and settling of particulate matter. Alternative models could include the aggregation of hydrothermal particles with settling detrital material, as a scavenging mechanism as described in Section 1.4.1. Another process could be resuspension of bottom sediment, which would control both the hydrothermal and detrital input; however, the placement of the on-axis sediment trap at 8 m above seafloor is to help decrease the likelihood of collecting resuspended particles. A third, but unlikely explanation as there was no evidence of this occurring in the sediment mass accumulation rates, would be changes in the efficiency of the sediment trap, where the collection of material may be impacted due to clogging.

5.1.2 Scavenged and partially hydrothermal origin elements

Elements that are scavenged by hydrothermal particles from seawater or co-precipitated during formation of sulfides and Fe-oxyhydroxides can be used along with hydrothermal elements (Fe, Cu, and Zn) to understand the processes controlling formation and deposition of hydrothermal particles moving off-axis (Section 1.4.1; 4.2.3; Figure 4.6). Fe-oxyhydroxides, sulfides, and Mn-oxides are efficient scavengers of dissolved seawater species, such as P, V, Cr, As, Y, Co, Cd, Mo, Pb, U, and the Rare Earth Elements (REEs) (German et al., 1991; Rudnicki and Elderfield, 1993; Dunk and Mills, 2006; Poulton and Canfield, 2006). The concentration of the calculated hydrothermal component of these elements in the on- and off-axis sediment trap samples correlate linearly with the concentrations of Fe_{HT} (Figure 4.6) due to plume dilution and fallout processes controlling the presence of hydrothermally derived particles with distance from the vents, as described above.

The uptake of elements (e.g., P, V, Cr, As, Y, Co, Cd, Mo, Pb, U, and REEs) onto hydrothermal particles is by scavenging and co-precipitation with Fe-oxyhydroxides, sulfides, and poorly crystalline Mn-oxides. The co-precipitation mechanism encompasses the time associated with the formation of a solid solution and the initial rapid trace metal sorption during the period of iron particle formation in the buoyant plume (Rudnicki and Elderfield, 1993). Colloidal ferrihydrite ($Fe(OH)_3$) derived from the hydrothermal plume is a highly efficient sink for the above scavenged elements, as it has a high specific surface area (Feely et al., 1994;

Dunk and Mills, 2006). Previous studies (e.g. Feely et al. (1994) and references therein), have looked at the mechanisms of scavenging by hydrothermal particulate matter that show a significant amount of scavenging from seawater occurs in the rising buoyant plume. The high concentrations of the above elements in the hydrothermal component is controlled by the co-precipitation of anions present in the ocean water. This co-precipitation mechanism occurs during the formation of hydrothermal sulfides and Fe-oxyhydroxide particles in the rising plume and the early neutrally buoyant plume (Metz and Trefry, 1989; Feely et al., 1991, 1994, 1998; Rudnicki and Elderfield, 1993; German et al., 1997; Edmonds and German, 2004).

Similarly to the processes controlling the presence of P, V, Cr, As, Y, Co, Mo, Pb, and U, are the co-precipitation and scavenging mechanisms of the rare earth elements from seawater onto Fe-oxyhydroxides in the buoyant and early neutrally buoyant plume (Michard et al., 1983; Michard and Albarède, 1986; Rudnicki and Elderfield, 1993; Klinkhammer et al., 1994; Mitra et al., 1994; Bao et al., 2008). In the on-axis sediment trap samples, normalization to Cascadia Basin sediments reveals a positive Eu anomaly, negative Ce anomaly, and a slight heavy REE enrichment (Figure 4.8). The Eu/Eu* in the on-axis sediment trap samples ranges from 1.5-2.5, which is typical of hydrothermal vent fluids, and I interpret this as indicating that the REE in the on-axis sediments accumulate REE directly from the vent fluids, not just by scavenging these from seawater (Michard and Albarède, 1986; German et al., 1990; Klinkhammer et al., 1994; Hrischeva and Scott, 2007). The Ce/Ce* ranges from 0.66-0.88, a negative Ce anomaly, which is a signature obtained from seawater, that is interpreted as scavenging of REEs from seawater (Hrischeva and Scott, 2007).

With increasing distance from active venting, there is less of a hydrothermal input of REE's to the sediments and an increased proportion of detrital material or scavenging from seawater, this is reflected in the REE signature of the 3 km and 9 km off axis sediment trap samples. The REE pattern in the 3 km and 9 km off-axis sediment trap samples, relative to background Cascadia basin sediment, is LREE enriched (Figure 4.8) with a smaller negative Ce anomaly (0.85-1.0), and a negative Eu anomaly (0.86-0.94). The small light REE enrichment may be indicative of a small amount of continual scavenging occurring within the neutrally buoyant plume (Barrett and Jarvis, 1988). Light REEs are preferentially scavenged onto Fe-oxyhydroxide particles in the neutrally buoyant plume as the HREEs form more stable and soluble complexes than LREE in seawater, rendering them less susceptible to removal from the aqueous phase (Owen and Olivarez, 1988).

5.1.3 Hydrothermal Manganese

The presence of Mn in the hydrothermal plume is controlled by the initial concentration of Mn in the vent fluid, and further the oxidation rate of Mn and subsequent particle formation and settling rates (Section 1.4), which differ from those controlling the presence of Fe, Cu, Zn, and scavenged elements. In the sediment trap samples the Mn concentration increases with distance from the vents, in contrast with the other hydrothermal elements. This is interpreted to be due to the sluggish oxidation kinetics of Mn(II) to Mn(III/IV) in the neutrally buoyant

plume (Cowen et al., 1986) compared to that of Fe(II) oxidation and formation of Fe(III)-oxyhydroxides. The MAR of Mn in the sediment trap samples (Figure 4.5) increases with distance from active venting, though with the same low MAR being observed in the 3 km off axis sediment trap samples as other hydrothermal elements, suggesting the trap was not collecting a significant amount of hydrothermal material.

5.2 Short term temporal variation in sediment trap geochemistry

The main purpose of this section is to interpret the observed variations in the compositions of hydrothermally derived sediments collected in on-axis sediment traps on a monthly to yearly time scale. Off-axis (3 km and 9 km) sediment trap samples are examined on a monthly scale. This data is used to interpret the stability of the hydrothermal plume. The on-axis sediment trap samples are used to examine processes occurring in the water column near active vents that affect the sedimentation of hydrothermally derived and scavenged elements.

Chemical analyses of hydrothermal vent fluids (e.g. Massoth, 1994) demonstrate that hydrothermal systems are dynamic systems with variable chemical and physical properties. To understand what controls this variability, frequent sampling and continual monitoring of the hydrothermal plume and sediments is necessary. From geochemical analyses of hydrothermal sediments over short term time scales collected in sediment traps, we see that the MARs of the hydrothermally derived elements (Fe, Cu, and Zn) in the on-axis sediment trap samples vary over a one-year sampling period (Figure 4.13**,** Figure 4.14). There are several possible explanations for this variation. The first is that changes in hydrothermal activity can influence the output and chemistry of hydrothermal vent fluids that can have an influence on particulate matter formation. Secondly, a change in the proportions of the overall material (i.e. amount of each component: hydrothermal, detrital, and biological) may suggest an increased influence from the water column above, or a decrease in hydrothermal activity. Thirdly, variations in hydrothermal sedimentation rate could be due to the influence of bottom currents within the ridge at the Main Endeavour Field, this can be examined through ACDP data. A last but unlikely mechanism would be the sediment trap clogging or malfunctioning, for which we do not have any evidence during the study based on the mass accumulation rates of the sediment collected.

The mass of sediment accumulated in sediment traps (Figure 4.1,Table 4-1) was relatively constant yearly sediment mass flux in the on-axis sediment traps when comparing total yearly mass accumulation, in 2014-2015 31.1 g m^{-2} $year^{-1}$, 2017-2018 18.08 g m^{-2} $year^{-1}$, and 2019-2020 24.8 g m^{-2} $year^{-1}$ of sediment was collected. Periods of high mass accumulation in the on-axis sediment trap samples occurred in the early Summer and Winter in the 2014-2015 and 2019-2020 sediment trap samples. This seasonal variation is not observed in the 2017-2018 sediment trap samples; however, the overall rate of accumulation is much lower in the 2017-2018 sediment trap samples, and the highest rate of accumulation coincides in time with the lower level of accumulation in the 2014-2015 and 2019-2020 sediment trap samples. This difference in mass accumulation may be due to differences in the placement of the

sediment traps (Figure 2.7), it could also be due to slight variations in plume trajectory or a decreased level of hydrothermal activity during this time.

The mass accumulation rate of the hydrothermal component (Fe, Cu, Zn) correlates strongly with the total rate of sediment mass accumulation in the 2014-2015, and 2019-2020 sediment trap samples. When the rate of hydrothermal element accumulation is high during periods of high sediment mass accumulation, there may have been an increase in hydrothermal activity, or a dynamic change in the plume chemistry and/or particle formation. In the 2017-2018 sediment trap samples, a correlation between the abundance of different hydrothermal elements exists although there is a difference in the relationship between mass accumulation and hydrothermal element accumulation. A comparison of the temporal trends in the 2017-2018 samples shows increasing sediment mass accumulation from December 2017 onwards, whereas this trend is not observed in the hydrothermal element mass accumulation. This period of time aligns with an increase in both terrigenous and biological mass accumulation rates (Figure 4.12, Figure 4.14, Figure 4.17). Therefore, I suggest that an increase in delivery of material from the overlying water column, and perhaps a subsequent decrease in hydrothermal activity and/or sedimentation may explain these observations. Besides this anomalous time period in 2017-2018, the mass accumulation rates of hydrothermal Cu and Zn are strongly correlated with hydrothermal Fe, sediment mass accumulation rate, and the mass accumulation rate of terrigenous and biological material (Figure 5.2). The proportion of each component is relatively constant within each sampling period, as observed in the ratio of Fe_{HT} MAR to Ti MAR. The consistency of the sediment composition, although there is a changing amount of material being collected by the sediment traps, could indicate a tight correlation between hydrothermal, terrigenous, and biological material in the near axis sediments. This could be explained by aggregation of hydrothermal particulate matter with terrigenous and biological material from the water column is occurring before deposition (Breier et al., 2012). It could also be indicative of resuspension and redeposition of bottom material into the sediment traps, and for this reason the sediment traps are emplaced at a height of 8 m to minimize the amount of resuspended material that is able to be caught by the traps.

An Oceans Network Canada Acoustic Doppler Current Meter (ADCP) was deployed next to the sediment trap provides insight into local currents above the sediment trap. This data can be downloaded from the ONC online database and was processed, and plots were created by Dr. Steve Mihaly. This data can be used to understand the currents close to the seafloor in the near on-axis region, which appears to control the rates of sediment deposition in the on-axis sediment traps. The 600 kHz ACDP data at 12 m above the bottom of the seafloor gives insight into the currents above the height of the sediment traps. The ADCP is deployed to the south of the cluster of vents in the MEF (Grotto, Dante, Lobo, etc.) where the plumes of these isolated vents coalesce into a single plume at around 10 m above the bottom (Thomson et al. (2005), Figure 1.8). The near bottom currents are focussed towards the rising coalescing plume from the cluster of vents in the ridge valley, due to an inflow of bottom water toward the plume as the buoyant plume is rising (Thomson et al. (2005); Figure 1.8). Current reversals had been

observed by Thomson et al. (2005) ~10% of the time, which is consistent with the data collected over the 2017-2018 sampling period with a 13% current reversal, and 11% in the 2019-2020 sampling period. It has been suggested that the reversals are linked to intermittent bursts of strong southwesterly flow in the overlying water column that may be wind-driven (Thomson et al 2005). The near-bottom currents may have an impact on the amount of hydrothermal particulates from the buoyant plume, as well as the amount of background material (terrigenous and biological) that is able to accumulate in the sediment traps as the currents control the fallout of the material from the water column. In the following ADCP plots data is presented for the 2017-2018 and 2019-2020 (Figure 5.1) sediment trap sampling periods.

In the 2017-2018 sampling period, the northward flow rate was slower from October 2017 to January 2018 (Figure 5.1) than during the rest of the year, depicted in Figure 5.1 as 2-week time indicators plotting closer together. A slower northward flow correlates with an increase in the mass accumulation during that period (Figure 5.2). During this period, the increase in overall sediment mass accumulation is accompanied by an increase in terrigenous and biological material mass accumulation rates, and a decrease in hydrothermal mass accumulation rates. This could be explained by sediment resuspension due to the change in the speed of bottom water currents, or a higher influx of terrigenous material due to bottom water resuspension. This can be explained by a lower ratio of Fe_{HT}:Ti mass accumulation rates during this time period (Figure 5.2).

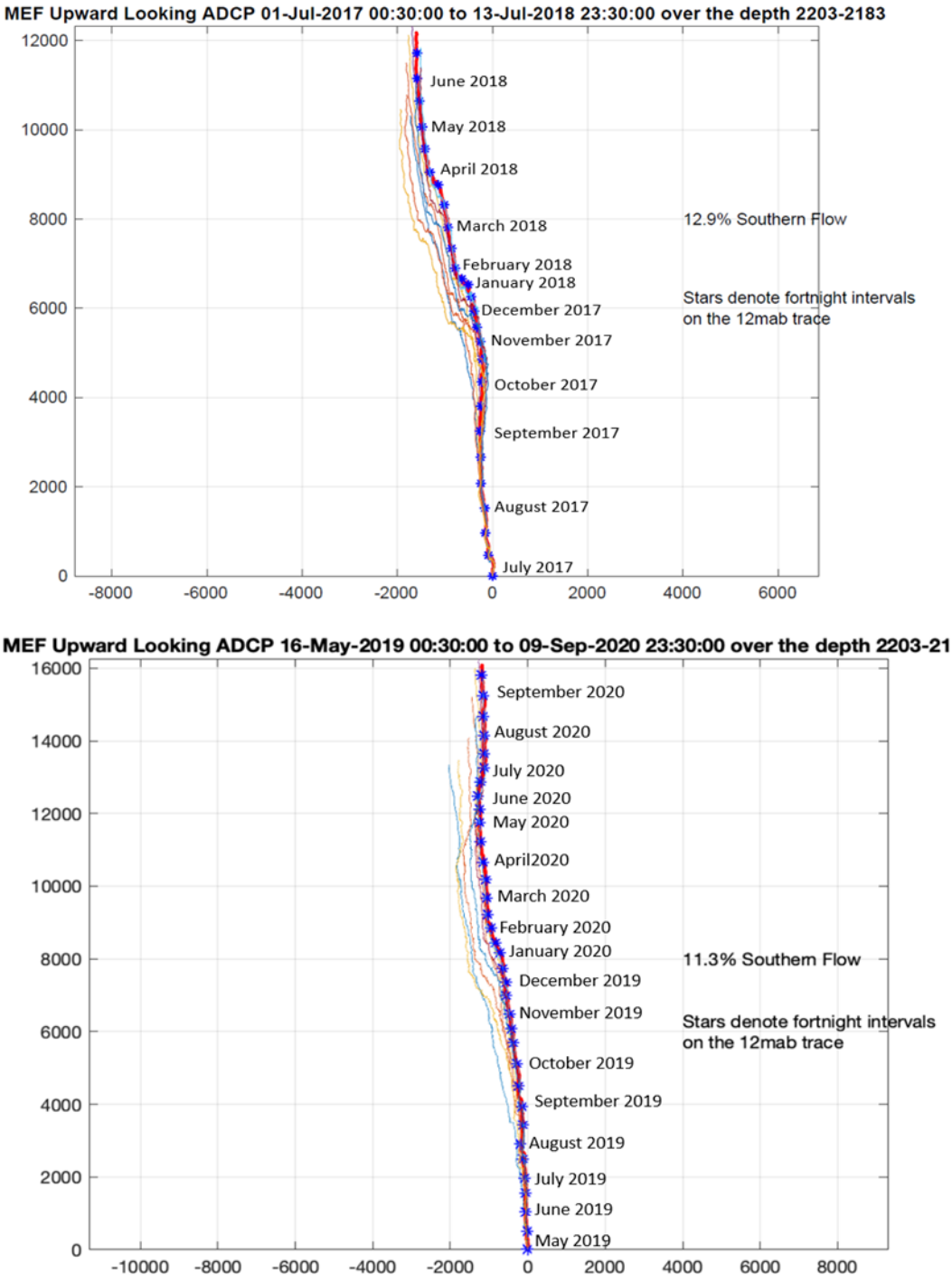

Figure 5.1 Acoustic Current Doppler Meter data for two sampling periods July 2017 to July 2018 (top), which encompasses the range of deployment dates of the 2017-2018 on-axis sediment trap, and May 2019 to September 2020 (bottom), which encompasses the range of deployment dates of the 2019-2020 on-axis sediment trap over the depth 2203-2221 mbsl. Each blue star is placed at two-week intervals on the 12 meter above bottom (mab) tracer.

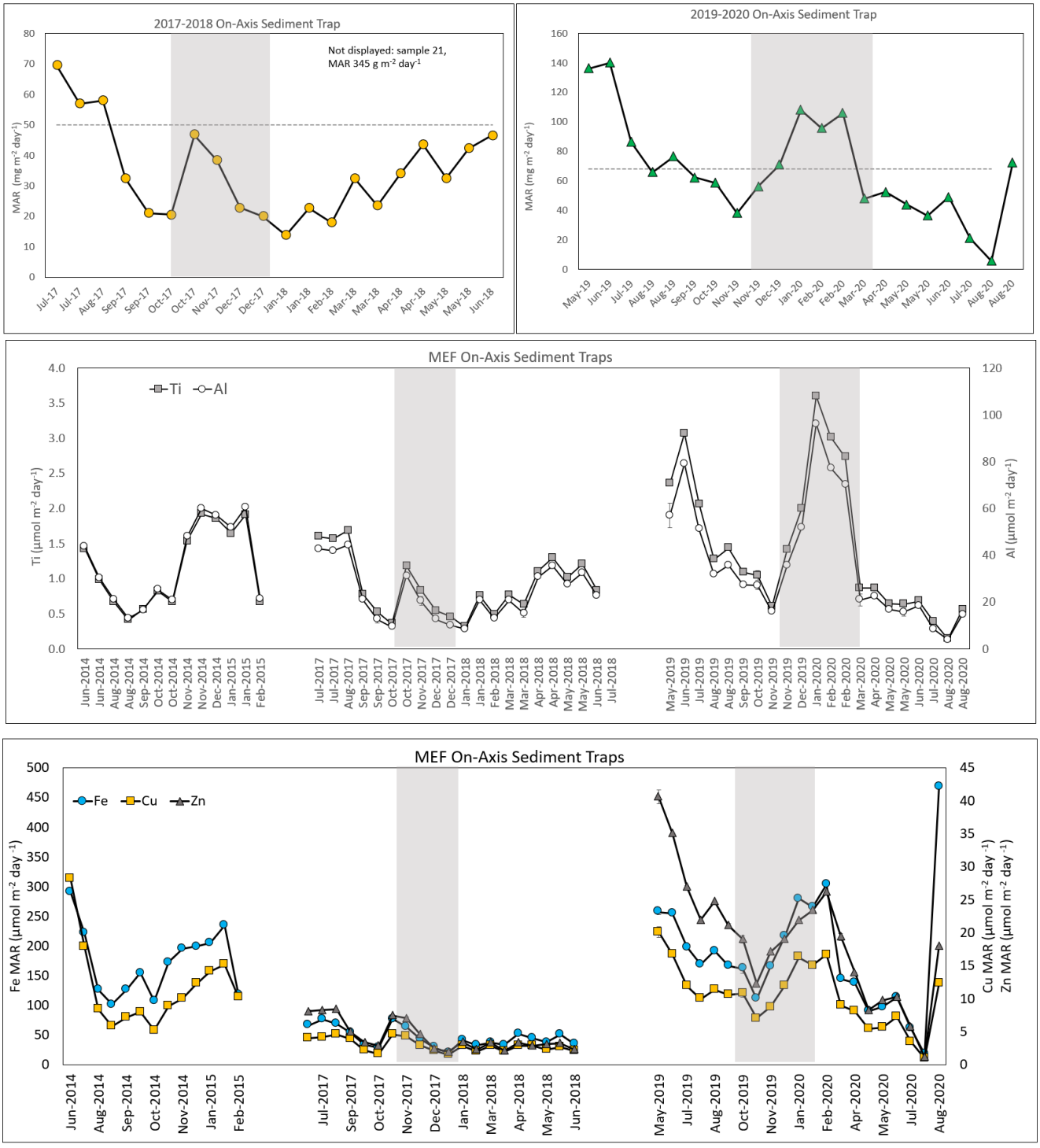

Figure 5.2 Comparison of 2017-2018 and 2019-2020 on-axis sediment trap (A) sediment mass accumulation, (B) terrigenous (Ti and Al) mass accumulation rates, and (C) Fe_{HT}, Cu_{HT}, and Zn_{HT} mass accumulation rates. Grey bars indicate time periods of slower northward flow as determined by an ONC ADCP meter as reference in Figure 5.1

Other potential explanations for the decrease in the hydrothermal mass accumulation rates during October – January 2017-2018, and December-February 2019-2020 could be due to a decrease in hydrothermal venting. When there is less vigorous venting, there may be less hydrothermal particulate matter forming, or a change in the composition of the hydrothermal particulate matter. The concentration of Cu is useful, as its concentration relative to Fe and Zn in vent fluids is temperature dependent (Seyfried et al., 2003). There is a 2x variation in the ratio of Cu_{HT}/Fe_{HT} observed over the on-axis sediment trap sampling periods and an approximately 3x variation in the ratio of Zn_{HT}/Fe_{HT} (Figure 5.3). There is little variation observed in the Cu_{HT}/Fe_{HT} ratio over the periods of December-February 2017-2018 and December-February 2019-2020). Which I interpret as indicating that decreased hydrothermal venting does not explain the decrease in hydrothermal mass accumulation during the periods of slow northward flow.

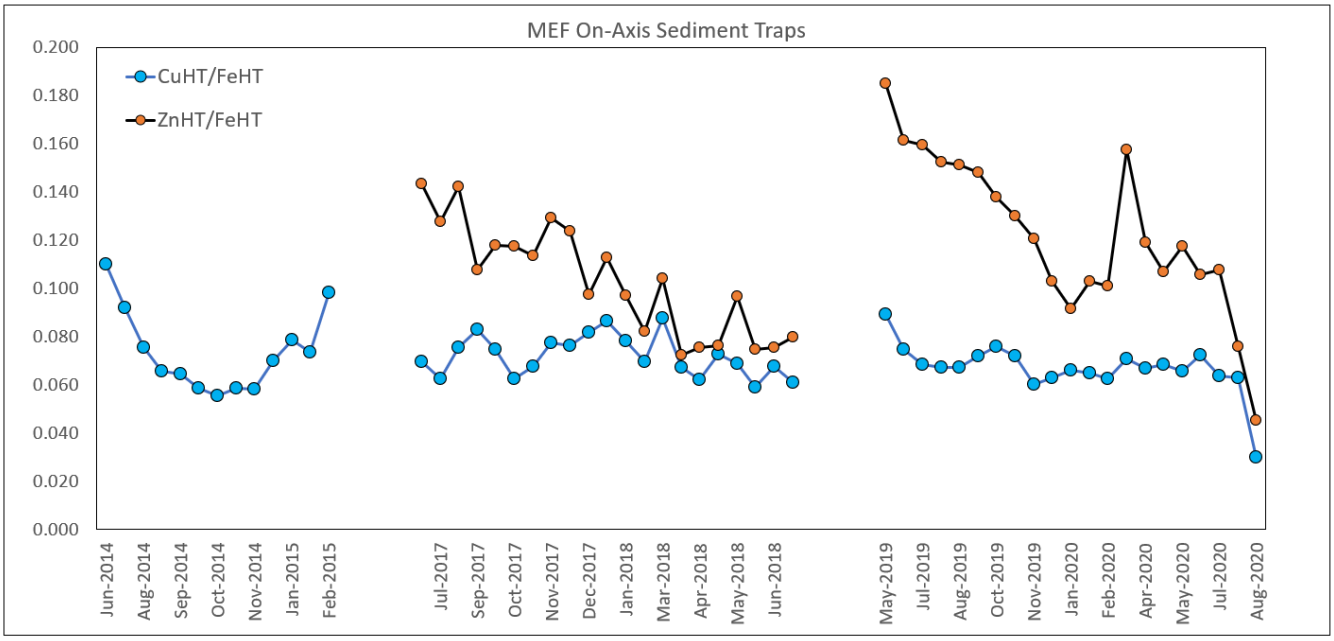

Figure 5.3 Ratio of CuHT/FeHT and ZnHT/FeHT over the 2014-2015, 2017-2018, and 2019-2020 on-axis sediment trap sampling periods.

An increase in terrigenous material in the on-axis sediment trap from October - January 2017-2018 and December – February 2019-2020 could also be due to storms along the North American coast, resulting in a higher amount of detrital material being transported from the continental margin to the ridge axis and deposited. This could be an explanation for the lower ratio of Fe_{HT}:Ti during this time period, however cannot explain the decreased rate of hydrothermal mass accumulation. The decreased rate of hydrothermal mass accumulation is likely a result of the slower northward current influencing the deposition of hydrothermal plume material during this time period.

5.2.1 Temporal variation in off-axis sediment trap geochemistry

In this section, changes in the mass accumulation rate of hydrothermally derived elements in the off-axis sediment traps are interpreted to provide insight into the stability of the plume and the processes operating within the near-axis hydrothermal plume.

There is a higher detrital mass accumulation rate in the 9 km off axis sediment trap than in the 3 km off axis sediment trap. In the off-axis sediment traps, the variation of mass flux may be due to local effects impacting the sedimentation of hydrothermal, terrigenous particles, and biological material. Hydrodynamic effects have been shown to affect the time series of mass flux over short periods of time (Siegel and Deuser, 1997; German et al., 2002; Buesseler et al., 2007; Adams et al., 2011; Rouxel et al., 2016). Previous work shows that bottom water currents affected by rough seafloor topography can be important in the temporal and spatial variability of hydrothermal mass fluxes (German et al., 2002; Adams et al., 2011), which is a potential explanation for the temporal variation observed in the off-axis sediment trap samples. Varying particle densities due to aggregation of hydrothermal particles with biological material (Figure 1.5) can also result in differential settling rates, which can result in short term variations in mass accumulation rates (Breier et al., 2012).

The 3 km off axis sediment trap collected a very small amount of sample at an average rate of 3.07 g m^{-2} $year^{-1}$. This is much lower than the sediment trap mass accumulation rates in the on-axis sediment trap samples that range from 18-31 g m^{-2} $year^{-1}$. As discussed in Section 4.2 the hydrothermal component significantly decreases with distance from the vent and the predominant component is the terrigenous component by 3 km off-axis (Figure 4.3, Figure 4.5).

The higher concentration and mass accumulation rate of Mn in the off-axis sediment trap samples compared to in the on-axis sediment trap samples is interpreted to be due to oxidation kinetics of Mn in the neutrally buoyant plume (as discussed in Section 1.4). The correlation between hydrothermally derived Fe and Mn in the 3 km off-axis sediment trap samples (Figure 4.4) is interpreted to indicate that both Fe-Mn oxyhydroxides and Cu-sulfides persist at this distance away from the vent, though a high amount of sulfide material has likely already been deposited in the near-vent sediments.

5.3 Post-depositional changes in the sediment core

The geochemistry of hydrothermal sediment cores are useful in understanding sedimentation processes and how the hydrothermal component may have changed over time. The preserved chemical composition should be evaluated using both sediment geochemistry and pore fluid chemistry to assess whether changes have occurred after deposition. If elements have been impacted by diagenesis, they may not be a suitable proxy to track long term hydrothermal sedimentation. Diagenetic processes in marine sediments include aerobic respiration of organic matter in the surface sediments, in which particulate organic matter is resolubilized. During this process, organic carbon, nitrogen (nitrate), and phosphorus (phosphate) are broken down in ratios that follow Redfields-Richards stoichiometry, 106:16:1.

Aerobic respiration increases the pore water concentrations of these components, and through complete oxidation of organic matter will generate CO_2. This process can further cause the breakdown of any calcareous shells in the sediment. Organic matter oxidation is favoured in the presence of O_2, as O_2 is depleted and sediments become anoxic, the sequence of reduction is denitrification, Mn(IV) oxide reduction to Mn(II), Fe(III) oxide reduction to Fe(II) and SO_4^{2-} reduction, based on the relative energetics of redox reactions (Libes, 2009). In the sediment core analyzed for this study, a strong brown-green oxidation-reduction (redox) boundary (Lyle, 1983) is present at 5-10 cm, and the geochemical signature of the elements preserved in the sediment and the concentrations of elements in the pore fluids are useful to understanding redox reactions in hydrothermal sediments.

There are multiple ways to identify elements that may be affected by diagenesis. The first is by comparison to the concentration of hydrothermally derived or scavenged elements to background sediments from the Cascadia Basin, where if the concentrations seen in the sediment core are at background concentration with little to no enrichment, it has potentially been lost from the sediments by diagenetic remobilization. A comparison with the 3 km off axis sediment trap can then be made, since the sediment core was collected from a similar distance from active venting, and if an enrichment is seen in the 3 km off axis sediment trap and not in the sediment core, this could also be indicative of post-depositional loss. The brown-green boundary in the core is indicative of changing redox conditions where Fe is reduced, and a change in the concentration of the element across this colour-change boundary may be due to their behaviour being different under Fe-oxidizing and Fe-reducing conditions, and elemental associations with Fe_{HT} in these sediments. This is often accompanied by mobilization and reprecipitation within the sediment core.

The ratio of OC:N (Figure 5.4) increases with depth, indicative of organic material breakdown. The Redfield-Richards OC:N ratio for unaltered organic material is 6.6. The average OC:N ratio is 7.4 in the on-axis sediment trap samples, 8.6 in the 9 km off-axis sediment trap samples, and within the sediment core the ratio ranges from 9.5-14 (average 12.3), which is consistent with organic matter breakdown with depth in the sediment core where the mobilization of N is preferred. There is no significant systematic variation in the sulfur concentration in the sediment core (Figure 5.4). The S concentration in the sediment core is ~5000 $\mu g\ g^{-1}$, this is much lower than in the on-axis sediment trap samples with high concentrations of sulfides, but cannot be compared to the 3 km and 9 km off-axis sediment trap samples as the data was unreliable as explained in Section 3.4, as well as not reported by Carpentier et al. (2013) for Cascadia Basin sediments. This low, and relatively unchanging concentration with depth, may be indicative of sulfur already have been lost from the sediment throughout the entire core to the pore fluid. Pore fluid chemistry data has not been collected for carbon, nitrogen, or sulfur; therefore, the above hypothesis cannot be tested with the data currently available.

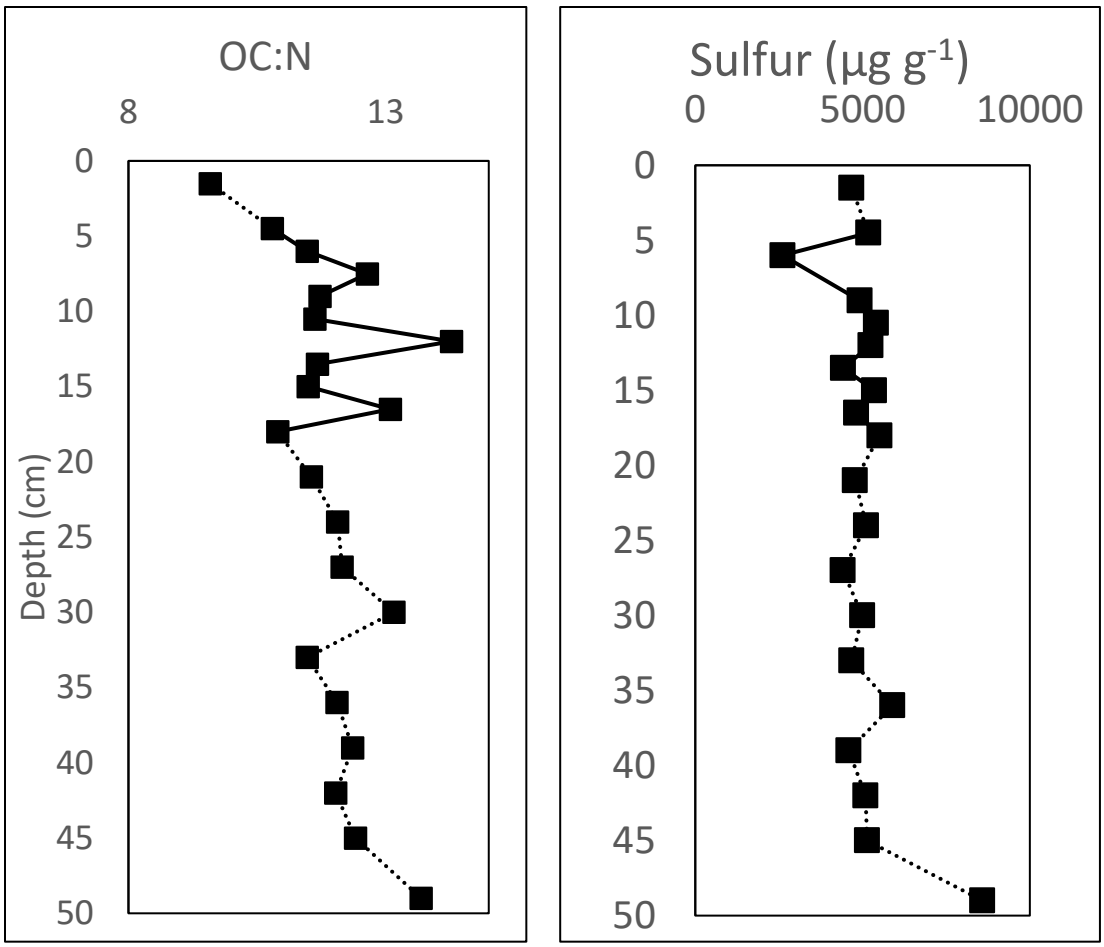

Figure 5.4 (left) ratio of Organic Carbon to Nitrogen (OC:N) in sediment core H-1581. (right) sulfur concentration in sediment core H-1581. Dotted line is representative of sample depth that had not been analysed and is missing from the core reconstruction.

5.3.1 Post-depositional alteration of hydrothermally derived elements

The most notable redox related change in hydrothermally derived elements in the sediment core is observed for manganese. The highest Mn concentration is in the surface sediments, which have a Mn concentration of 4,000 µg g^{-1} above the brown-green transition zone and this decreases to 580 µg g^{-1} at 6 cm below the surface, at the top of the brown-green transition zone (Figure 4.18). The deeper samples with a concentration of Mn of ~580 µg g^{-1} (~0.1 wt% MnO) are comparable to background Cascadia Basin sediments, with an MnO content of 0.1-0.2 wt% (Carpentier et al., 2013). The concentrations of Mn in the pore fluids is higher than in deep Pacific seawater throughout the core, ranging from ~600-5,000 nmol kg^{-1} (Figure 4.22). In previous studies of Mn in sediments and pore fluids, it has been observed that under reducing conditions (e.g. below the brown-green boundary) Mn becomes depleted in the sediment when Mn(IV) is reduced to the more soluble Mn(II), which diffuses upward and reprecipitates in the oxidized zone near the surface (Lyle, 1983) or escapes to the water column (Shimmield and Price, 1986; Scholz et al., 2013). The high Mn concentration in the upper 5-6 cm of sediments is highly suggestive of Mn re-precipitating in the oxidized surface layer. The concentration of Mn

in the upper sediments of the sediment core is higher than the average concentration of Mn in the 3 km off axis sediment trap sample, which supports the hypothesis that Mn is re-precipitating in the oxidized surface layer (Shimmield and Price, 1986).

This behaviour of Mn has been observed in other core samples taken of hydrothermal sediments at varying locations in the ocean. For example, in a hydrothermal sediment core taken from 1°N of the East Pacific Rise near zero Mn concentrations were determined in the uppermost sediments, aged >20 ky BP, which was attributed to MnO_2 reduction and upward migration of dissolved Mn(II) (Lund et al., 2016), as I believe is occurring in sediment core H-1581.

The concentration of hydrothermal Fe and Cu in the sediment in the sediment core follow similar downcore trends, with the highest concentrations observed within the brown-green transition zone between 6-10 cm and decreasing below and are depleted compared to the sinking particles collected in the 3 km off axis sediment trap (Figure 4.4, Figure 4.18). The concentration of Fe and Cu in the pore fluid are elevated above seawater concentrations. The pore fluid profile of Cu (Figure 4.18) reveals elevated concentrations in the oxidized surface sediments, above the brown-green transition zone. Within the reducing sediments at depth, the concentration of Cu in the pore fluid is lowest and relatively constant (Figure 4.22). The pore fluid profile of Fe (Figure 4.18) overall has a small increase in concentration with depth. When compared to the 3 km off axis sediment trap, the range of concentration of hydrothermal Fe in the sediment core is higher than the 3 km off axis sediment trap, with an overlap on the lower end of concentrations (Figure 4.4). This is suggestive of little Fe being lost from the sediment core; as with higher pore fluid Fe concentrations there may be some Fe-sulfide dissolution, which would be a source of Fe into the pore fluid. With respect to Cu, it is suggestive that hydrothermal Cu is being lost from the sediment, likely due to dissolution of Cu-bearing minerals that are delivered by hydrothermally derived particulate matter.

The concentration of hydrothermal Zn in the sediment core (Figure 4.18) and in the pore fluids (Figure 4.22) are low, and relatively constant at all depths in the sediment and pore fluid. When compared to the 3 km off axis sediment trap, the hydrothermal Zn in the sediment core is lower (Figure 4.4). This suggests that Zn-bearing minerals are dissolving during diagenesis.

In summary, the concentration of Fe_{HT} appears to be minimally altered in the sediment core, and therefore probably can be used as a paleo-proxy for the analysis of the hydrothermal component of sediments over thousand-year time scales (~6,000 years), whereas Cu, Zn, and Mn are partially to fully lost during diagenetic reactions at depth.

5.3.1.1 Post-depositional alteration of scavenged elements

The concentration of Mo, P, and As in the sediments in the sediment core are highest at the surface, reach a minimum within the brown-green transition zone, and are then relatively constant with depth (Figure 4.19) Pore fluid concentrations of Mo are low in the surface sediments and increase with depth (

Figure 4.24), similar to Mn in the pore fluid (Figure 4.22). The calculated concentration of hydrothermal P is close to zero below the brown-green transition zone, suggesting that little to no hydrothermal phosphorus remains – in all of the above the context of the concentrations in the 3 km off-axis sed trap would help. There is no P or As data for the pore fluids due to calibration issues. In the hydrothermal plume, Mo is predominantly associated with Mn-oxides and hydrothermal sulfides (Morford et al., 2005; Mills et al., 2010), in the on-axis sediment trap samples Mo is associated primarily with hydrothermal sulfides, as previously observed by Mills et al. (2010). Oxidation of sulfides will release Mo to the pore water, and it may be that the Mo content of the post-oxic sediments is controlled by redox cycling of Mn at depth (Schaller et al 2000; Mills et al 2010). In the sediment core Mo does not correlate well with either Mn or S (Figure 5.5). This is likely due to loss of all Mn in the reducing sediments, and diagenetic loss of sulfur at depth. Therefore, it is difficult to determine the importance of these elemental and mineralogical associations. Similar to Mo and Mn, P and As appear to have been mobilized post deposition. Earlier work suggested that elements scavenged by Mn and Fe colloidal phases in hydrothermal particulates are likely to undergo dissolution in reducing sediments, which would release these elements to the pore waters (Feely et al., 1994). Without pore fluid concentrations, this cannot be tested directly, but the sediment compositions suggest that P and As are being remobilized at depth. If hydrothermal Mo, P, and As are remobilized at depth with changing redox conditions, as is suggested by the geochemical data, their utility as paleo-hydrothermal tracers may be limited.

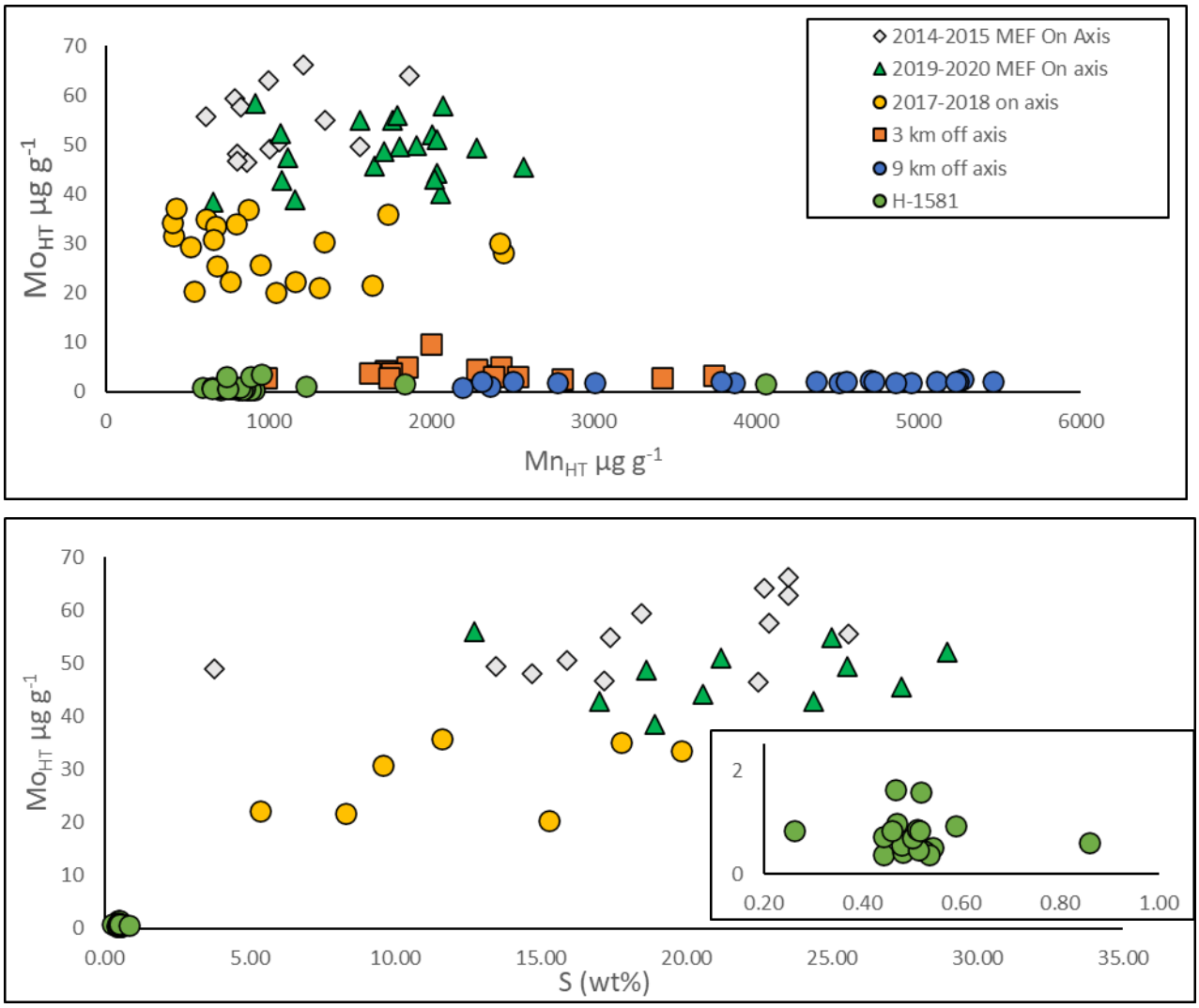

Figure 5.5 (top) cross plot of hydrothermal Mn versus hydrothermal Mo for on-axis, 3 km off axis, 9 km off axis sediment trap samples and sediment core H-1581. (bottom) cross plot of sulfur vs hydrothermal Mo for sediment trap samples, zoomed in box is the concentrations in sediment core H-1581.

5.3.2 Sediment geochemistry changes in the context of glacial-interglacial hydrothermal activity

From the geochemical data of the hydrothermal and scavenged elements, it appears the primary signature is somewhat masked by post depositional changes. This raises the question as to whether sediment cores provide reliable records that can be used in long term studies for changes in hydrothermal activity. Based on the sediment and pore fluid data, it appears that hydrothermal Fe preserves a reliable record of hydrothermal activity and is not significantly modified by post-depositional changes. Based on the potential for changes to occur in various redox conditions, it raises the question of: are hydrothermal sediment records useful to reconstruct hydrothermal activity in the sedimentary record based on how they have been changed over 6,000 years of deposition? While it is not realistic to draw conclusions based on

the behaviour of one sediment core, as it may not be a reliable archive of hydrothermal activity over time, the magnitude of changes that are being preserved in the sediment core can be compared to previous studies over glacial periods as summarized below.

Lund and Asimow (2011) first suggested a relationship between sea level and hydrothermal flux on mid-ocean ridges where the lowering of sea level during glacial maxima is hypothesised to lead to increased melting and greater magma fluxes to the ridge crest. Such a change in hydrothermal activity was observed in Icelandic subaerial volcanoes (Jull and McKenzie, 1996) where it is suggested to be due to a decrease in the overburden load from the ice sheet retreat, which reduced pressure in the mantle and subsequently enhanced melt production and magma supply to the surface. On the global mid-ocean ridge system, the change in pressure due to the variable glacioeustatic sea level is much smaller than that due to ice sheet retreat in Iceland; however, a global deglaciation would affect all the mid-ocean ridges and could have a significant effect on hydrothermal activity. Sediment cores have been analysed from the East Pacific Rise (e.g., Lund et al., (2016)), Mid Atlantic Ridge (e.g. Costa et al., (2016)), and the Juan de Fuca Ridge (e.g., Costa et al., (2017)) to test this hypothesis.

The variation in the concentration of Fe in sediments near hydrothermal vent fields over glacial-interglacial time scales can be compared to those measured in the 6,000 year old sediment core studied here. In the sediment core, the concentration of hydrothermal Fe show an approximately two fold variation (Section 5.3). Across glacial-interglacial periods Lund et al., (2016) show an approximately 2-2.5x increase in the flux of Fe on the East Pacific Rise during the termination of the last glacial period. Middleton et al., (2016) observed a 6-8x increase in the hydrothermal Fe and Cu flux at the last glacial maxima preserved in sediment from the Mir zone of the TAG hydrothermal field at 26N on the Mid-Atlantic Ridge. Costa et al., (2017) observed a variation of 2-3x in the concentration of hydrothermal Fe and a 6-8x increase in hydrothermal Fe flux over multiple glacial-interglacial periods on the Juan de Fuca Ridge. The overall variation of hydrothermal Fe flux observed across glacial-interglacial periods (Middleton et al., 2016; Costa et al., 2017) is higher than the variation in the hydrothermal accumulation rates observed in the sediment core; however, the variation in concentration observed is comparable. The variation in concentration observed is comparable to that observed across glacial-interglacial time scales, which is has previously been suggested as large variations that can be attributed to these large global changes; however, if the changes are observed on a short time scale it may not be reliable to say the spike in hydrothermal component is definitively related to G-IG changes.

5.3.3 Sediment core geochemistry compared to the tectonic evolution history of the MEF

As has been previously discussed, the concentration of Fe in the sediment core has likely been relatively unchanged due to the effects of diagenesis, especially with comparison to the depletion of Cu, Zn, and Mn in the sediment core to the sediment trap samples. The timing of variability in the Fe_{HT} concentration in the sediment core, with the assumption of a constant rate of accumulation based on the ~5,000 year radiocarbon date from the basal section,

correspond loosely to the timing of magmatic events on-axis at the Main Endeavour Field as analyzed by (Clague et al., 2014b). This study denoted three key periods at the Main Endeavour Field, where prior to ~4,300 yr BP there were frequent, large volume eruptions and is called the magmatic phase, from ~4,300 - ~2,300 yr BP there were infrequent eruptions as the ridge extended and the axial graben formed which was the tectonic phase, and since then the Endeavour Segment has been undergoing intense hydrothermal activity.

The timing of magmatic phase and hydrothermal phase appear to be preserved in the geochemistry of the sediment core, where if accumulation was constant over ~5,000 years, each centimeter of deposition represents a time period of ~500 years. The above time phases are depicted in Figure 5.6. Where the highest concentrations that correspond with the top 20 cm of the sediment core appear to correlate with the hydrothermal phase, where the lower concentrations of the bottom 30 cm of the sediment core correlate with the tectonic and magmatic phases of the history of the Main Endeavour Field. The timing of these events appear to be preserved in the depositional history of the sediment on the western flank of the Main Endeavour Field.

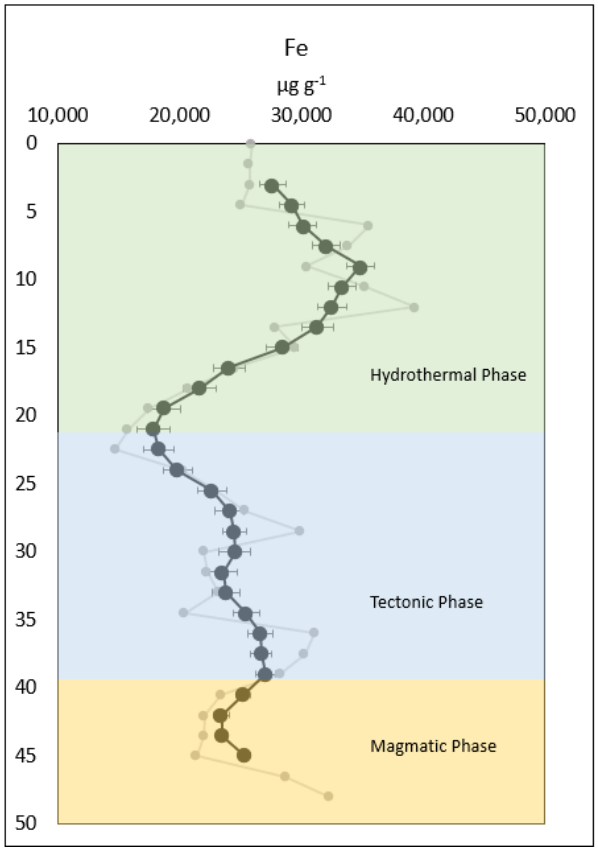

Figure 5.6 Time periods of the eruptive and tectonic history as described by Clague et al. (2014) compared to the variation in the concentration of FeHT in the sediment core with the assumption of constant accumulation over time.

6 Conclusions and Further Research

The division of this work into spatial and temporal variation in the composition of hydrothermal sediments at the Endeavour hydrothermal vent field gives new insights into how the composition of the sediment changes with distance from the vents and the variation of sediment chemistry over short-time scales. Previous to this study, very few sediment trap analyses have been conducted to study the change in composition over time at the Endeavour Hydrothermal Vent Field; firstly, a sediment trap by Dymond and Roth (1988) was deployed near the High Rise vent field to study hydrothermal particulate chemistry and mass accumulation rates, and another sediment trap in 2014-2015 was emplaced near active venting at the Main Endeavour Field by Coogan et al. (2017) to investigate the change in hydrothermal composition with distance from the vent. The collection of the Main Endeavour Field on-axis sediment traps from 2017-2018 and 2019-2020, and the 2019-2020 3 km and 9 km off-axis sediment traps has increased the availability of sediment chemistry data to understand further what processes are controlling the chemistry and mass accumulation of hydrothermal sediments with distance from active venting and over time on short (weekly to yearly) time scales.

The investigation of the spatial variation of the geochemistry of hydrothermal sediments with distance from the vents predictably shows that near active venting, the early formation of sulfides and Fe-oxyhydroxide particles, and their subsequent sedimentation, is the predominant control on the high concentrations of hydrothermal Fe, Cu, and Zn in the near vent-field sediment trap. Through isolation of the hydrothermal component, by removal of the detrital component, the change in the composition of the hydrothermal component was examined with distance from active venting. With distance from the vents, progressive dilution of the hydrothermal plume and plume fallout of hydrothermal particulate matter, results in a decrease in the concentration of hydrothermal Fe, Cu, Zn, Ag, and Cd in the 3 km and 9 km off-axis sediment trap samples. The concentration of these elements in the 3 km off axis sediment trap samples does not fully follow the predicted pattern, with lower concentrations and sediment mass accumulation than expected. It is thought that this may be due to the trajectory of the hydrothermal plume, and the sediment trap not being placed directly beneath the path of the plume. The elements (P, Pb, Mo, REEs) that are scavenged and/or co-precipitated by hydrothermal particles (sulfides and Fe-oxyhydroxides) exhibit comparable behaviour to hydrothermal Fe concentration and mass accumulation rates. This may be expected if a significant amount of the scavenging process occurs rapidly in the early stages of the formation of the hydrothermal plume, and not progressively with distance from the vent. The concentration and mass accumulation rate of Mn in the sediments is lowest in the on-axis sediment trap samples and increases in the sediment trap samples with distance from the vents. The concentration of hydrothermal Mn exhibits the opposite behaviour to Fe, Cu, and Zn

in the sediments is due to its sluggish oxidation kinetics (Cowen et al., 1990; Lavelle et al., 1992) in the hydrothermal plume.

The investigation of short-term temporal variability in the hydrothermal sediment composition gives insight into how the composition changes on monthly to yearly timescales. These changes are used as comparisons to changes observed over thousand-year time scales. The magnitude of change in both the concentration and mass accumulation rate of hydrothermal Fe, Cu, and Zn in the on-axis hydrothermal sediments show large variations in both the concentrations and mass accumulation between 21-day sampling periods. During periods of high sediment mass accumulation rate, the mass accumulation rate of hydrothermal elements (Fe, Cu, and Zn) are high; this could suggest an increase in the amount of hydrothermal fluid flux, a change in vent fluid chemistry, and/or particle formation. The amount of hydrothermal fluid flux could change without a change in vent fluid chemistry due to bottom water currents. Acoustic Doppler Current Meter data indicate a short term (2-3 months) decrease in the hydrothermal mass accumulation rate coincides with periods of flow reversal. The ADCP is deployed close to the cluster of vents in the MEF where the plumes of multiple isolated vents coalesce and move away from vents in a southwest direction, the near bottom currents are focussed towards the rising plume and away from the current meter and sediment traps. This period of flow reversal would move the hydrothermal particulate material away from the sediment traps.

In the off-axis sediment trap samples, the variation in the mass accumulation of the hydrothermal elements is lower than in the on-axis sediment trap samples. The 3 km off axis sediment trap however has a lower mass accumulation rate than in the 9 km off axis sediment trap samples, there is no evidence the trap had clogged during the collection period. This continues to be observed in subsequent sediment traps, and no explanation has been determined. There is an approximately 3x variation in the mass accumulation of the hydrothermal elements observed in the 3 km and 9 km off axis sediment trap samples over a year, and this range of variation is 3 orders of magnitude lower than the mass accumulation in the on-axis sediment traps samples. This is consistent with progressive dilution of the hydrothermal plume and a high degree of particulate fallout in the near-vent sediment trap samples.

The collection of a sediment core and pore fluids, along with sediment trap samples can be used together to understand post-depositional changes on hydrothermal sediments. The sediment trap samples are fresh, minimally altered particulate material collected as fallout from the hydrothermal plume, whereas the sediment core samples have been diagenetically altered. The utility of the hydrothermal elements (Fe, Cu, Zn, and Mn) in the sediment core was investigated to understand how post-depositional processes affect the preservation of this component. Based on the comparison of the concentration of these elements, it appears that Fe provides a reliable record of past hydrothermal activity and is not significantly modified by post depositional changes. Other hydrothermal and hydrothermally associated elements (Cu,

Zn and Mn, As, P, Cd, Mo) have been lost from the sediment core based on comparison to fresh, unaltered sediment from the sediment trap samples. This raises the question as to whether sediment cores are reliable records that can be used in long-term studies for changes in hydrothermal activity.

6.1 Future work

Moving forward in the study of hydrothermal activity, specifically hydrothermal sediment chemistry at the Endeavour Hydrothermal Vent Field, the continuation of deployment of sediment traps on-axis, 3 km off axis, and 9 km off axis will be important to creating a long-term, high resolution time series dataset on sedimentation along this transect below the hydrothermal plume. Major and trace element analyses should be continued to add to the already available dataset from the 2014-2015, 2017-2018, and 2019-2020 on-axis sediment trap samples and 2019-2020 3 km and 9 km off-axis sediment trap samples. With increasing experience in the preparation and analysis of these types of geological samples, these methods will continue to be optimized to obtain high quality chemical data.

In addition to major and trace element analyses, mineralogical analyses, such as using SEM and/or EDX methods on sediment trap samples would be valuable to understand how the mineralogy of the sediment changes with distance from active venting. These methods have been previously used on hydrothermal plume particles (e.g. Lough, 2016). High resolution mineralogical data on the sediment particles can be used to determine the composition of particles and their morphology. It is known that near vent deposits are dominated by rapidly precipitating Fe-sulfide minerals and Fe-oxyhydroxides and can be identified by mineralogy studies. With mineralogy data the speciation of the Fe-bearing minerals in the near vent deposits can be separated. With distance from the vent, the larger, dense sulfide minerals rapidly fall out of the plume, and the Fe-oxyhydroxide and nano-particulate sized sulfide particles are transported away from the axis. Particle morphology and composition can be used to further research metal bearing mineral size partitioning with distance from the vent. This data can be used to understand scavenging and co-precipitation mechanisms through the association of trace metals with specific minerals. In this study, scavenging and co-precipitation is assumed through the association of trace metals such as Mo, As, P, Co, Cd, Pb with hydrothermal Fe, Cu and Zn. If the mineralogy of the sulfide and oxyhydroxide particles was known, the signal of elements through SEM/EDX analysis can be used to develop a deeper understanding of how these elements are removed from the water column by hydrothermal particles. This is important as removal by hydrothermal particles acts as a sink for these trace elements in the deep ocean. The morphology and composition of particles can also be used to determine the aggregation of hydrothermal particles with biological and/or terrigenous material, which can then be used to understand sinking mechanisms and calculate particle flux rates of the particles from the hydrothermal plume to the sediments.

Further collection of sediment cores surrounding the hydrothermal plume, especially in the southwest direction from active venting, below the trajectory of the neutrally buoyant

plume and between the on-axis, 3 km off axis, and 9 km off-axis sediment traps can be used to increase the resolution of the spatial variation. Sediment samples should also be taken at further distances from hydrothermal venting as it is known that hydrothermal plumes can travel thousands of kilometers away from the source (Fitzsimmons et al., 2014) to determine if the hydrothermal signal persists in the sediments and to add available data to the study of the composition of marine sediments.

As more sediment cores are collected and analysed at a high resolution, like has been done in this work with 1.5 cm segments of core, the effect of post-depositional changes on hydrothermal elements over changing redox conditions with depth in the sediment core can be further studied. From this work, it appears that Fe is a good tracer of hydrothermal sedimentation over thousands of years, and Cu, Zn and Mn are diagenetically remobilized and lost from the sediment. It is difficult to make conclusions based on one sediment core, therefore further high-resolution analyses of sediment cores and pore fluids should be made.

The basal section of the sediment cores collected below the neutrally buoyant plume should be dated using radiocarbon analysis on foraminifera to further understand how hydrothermal sedimentation has changed over time. If multiple depths in the sediment core can be dated, a higher resolution time series of sedimentation should be reconstructed. This will aid in the creation of sedimentation models to understand how sedimentation has changed over time. The separation of hydrothermal and terrigenous component, as was done in this work, can be used to model the variation of hydrothermal activity. If sediment cores that span across the glacial-interglacial boundary are collected, work that has been previously published from the Juan de Fuca Ridge (Costa et al., 2017) can be continued to determine if the high hydrothermal signal at the last glacial maximum persists across all sampling sites.

The continuation of ACDP deployments near the hydrothermal vents, close to the on-axis sediment trap, can be used to further understand how bottom currents affect sedimentation. In this study, the two time periods of flow reversal, which would move material away from the sediment trap, were associated with decreased hydrothermal sedimentation in the sediment trap samples. The relationship between hydrothermal sedimentation, biological activity, and terrigenous input during these times of flow reversal can be used to understand how currents and the overlying water column affects the accumulation of hydrothermal sediments.

The relationship between the sediment chemistry and plume chemistry is increasingly important to create models of particle movement in the neutrally buoyant plume and subsequent sedimentation. The combination of both sediment and plume chemistry can be used to understand metal cycling within the deep Pacific Ocean. This is important in terms of Fe availability in the deep ocean due to its persistence in the neutrally buoyant plume (Fitzsimmons et al., 2014).

Through continuation and expansion of these types of collection methods (sediment traps and sediment cores, plume samples), it is important that there is consistency in terms of collection and analytical methods between research groups globally. This will make it easier to compare how the chemical composition of the sediments changes with distance from active venting at various hydrothermal vent fields.

7 References

Adams, D.K., Mcgillicuddy Jr, D.J., Zamudio, L., Thurnherr, A.M., Liang, X., Rouxel, O., German, C.R., and Mullineaux, L.S., 2011, Surface-Generated Mesoscale Eddies: Science, v. 332, p. 580–583.

Alt, J.C., 1995, Subseafloor processes in mid-ocean ridge hydrothermal systems, *in* Geophysical Monograph Series, doi:10.1029/GM091p0085.

Alves, E.Q., Macario, K., Ascough, P., and Bronk Ramsey, C., 2018, The Worldwide Marine Radiocarbon Reservoir Effect: Definitions, Mechanisms, and Prospects: Reviews of Geophysics, v. 56, p. 278–305, doi:10.1002/2017RG000588.

Ascough, P.L. and Cook, G.T. and Dugmore, A., 2009, Methodological approaches to determining the marine radiocarbon reservoir effect: Progress in Physical Geography, v. 29, p. 532–547, https://eprints.gla.ac.uk/5017/1/5017.pdf.

Baker, T., 1994, A 6-year time series of hydrothermal plumes over the Cleft segment of the Juan de Fuca Ridge: v. 99, p. 4889–4904.

Baker, E.T., and Massoth, G.J., 1987, Characteristics of hydrothermal plumes from two vent fields on the Juan de Fuca Ridge, northeast Pacific Ocean: Earth and Planetary Science Letters, v. 85, p. 59–73, doi:10.1016/0012-821X(87)90021-5.

Bao, S.X., Zhou, H.Y., Peng, X.T., Ji, F.W., and Yao, H.Q., 2008, Geochemistry of REE and yttrium in hydrothermal fluids from the Endeavour segment, Juan de Fuca Ridge: Geochemical Journal, v. 42, p. 359–370, doi:10.2343/geochemj.42.359.

Barrett, T.J., and Jarvis, I., 1988, Rare-earth element geochemistry of metalliferous sediments from DSDP Leg 92: The East Pacific Rise transect: Chemical Geology, v. 67, p. 243–259, doi:10.1016/0009-2541(88)90131-3.

Bennett, S.A., Rouxel, O., Schmidt, K., Garbe-Schönberg, D., Statham, P.J., and German, C.R., 2009, Iron isotope fractionation in a buoyant hydrothermal plume, 5°S Mid-Atlantic Ridge: Geochimica et Cosmochimica Acta, v. 73, p. 5619–5634, doi:10.1016/j.gca.2009.06.027.

Bischoff, J.L., and Seyfried, W.E., 1978, HYDROTHERMAL CHEMISTRY OF SEAWATER FROM 25 degree TO 350 degree C.: Am J Sci, v. 278, p. 838–860, doi:10.2475/ajs.278.6.838.

Bostrom, K., and Peterson, M.N.A., 1968, The origin of Aluminum-poor ferromanganoan sediments of high heat flow on the East Pacific Rise: v. 7, p. 427–447.

Breier, J.A., Toner, B.M., Fakra, S.C., Marcus, M.A., White, S.N., Thurnherr, A.M., and German, C.R., 2012, Sulfur, sulfides, oxides and organic matter aggregated in submarine hydrothermal plumes at 9°50’N East Pacific Rise: Geochimica et Cosmochimica Acta, v. 88, p. 216–236, doi:10.1016/j.gca.2012.04.003.

Bruland, K.W., 1980, Oceanographic distributions of cadmium, zinc, nickel, and copper in the North Pacific: Earth and Planetary Science Letters, v. 47, p. 176–198, doi:https://doi.org/10.1016/0012-821X(80)90035-7.

Buesseler, K.O. et al., 2007, An assessment of the use of sediment traps for estimating upper ocean particle fluxes: Journal of Marine Research, v. 65, p. 345–416, doi:10.1357/002224007781567621.

Burd, B.J., and Thomson, R.E., 1994, Hydrothermal venting at endeavour ridge: effect on zooplankton biomass throughout the water column: Deep-Sea Research Part I, v. 41, p. 1407–1423, doi:10.1016/0967-0637(94)90105-8.

Carpentier, M., Weis, D., and Chauvel, C., 2013, Large U loss during weathering of upper continental crust: The sedimentary record: Chemical Geology, v. 340, p. 91–104, doi:10.1016/j.chemgeo.2012.12.016.

Clague, D.A., Dreyer, B.M., Paduan, J.B., Martin, J.F., Caress, D.W., Guilderson, T.P., and Mcgann, M.L., 2014a, Eruptive and tectonic history of the Endeavour Segment, Juan de Fuca Ridge, based on AUV mapping data and lava flow ages: v. 15, p. 3364–3391, doi:10.1002/2014GC005415.Received.

Clague, D.A., Dreyer, B.M., Paduan, J.B., Martin, J.F., Caress, D.W., Guilderson, T.P., and Mcgann, M.L., 2014b, Eruptive and tectonic history of the Endeavour Segment, Juan de Fuca Ridge, based on AUV mapping data and lava flow ages: Geochemistry, Geophysics, Geosystems RESEARCH, v. 15, p. 3364–3391, doi:10.1002/2014GC005415.Received.

Clague, D.A., Martin, J.F., Paduan, J.B., Butter, D.A., Jamieson, J.W., Saout, M. Le, Caress, D.W., and Thomas, H., 2020, Hydrothermal Chimney Distribution on the Endeavour Segment , Juan de Fuca Ridge: Geochemistry , Geophysics , Geosystems, p. 1–12, doi:10.1029/2020GC008917.

Coogan, L.A., Attar, A., Mihaly, S.F., Jeffries, M., and Pope, M., 2017, Near-vent chemical processes in a hydrothermal plume: Insights from an integrated study of the Endeavour segment: Geochemistry, Geophysics, Geosystems, v. 18, p. 1641–1660, doi:10.1002/2016GC006747.

Costa, K.M., McManus, J.F., Boulahanis, B., Carbotte, S.M., Winckler, G., Huybers, P.J., and Langmuir, C.H., 2016, Sedimentation, stratigraphy and physical properties of sediment on the Juan de Fuca Ridge: Marine Geology, v. 380, p. 163–173, doi:10.1016/j.margeo.2016.08.003.

Costa, K.M., McManus, J.F., Middleton, J.L., Langmuir, C.H., Huybers, P.J., Winckler, G., and Mukhopadhyay, S., 2017, Hydrothermal deposition on the Juan de Fuca Ridge over multiple glacial–interglacial cycles: Earth and Planetary Science Letters, v. 479, p. 120–132, doi:10.1016/j.epsl.2017.09.006.

Cowen, J.P., Massoth, G.J., and Baker, E.T., 1986, Bacterial scavenging of Mn and Fe in a mid- to far-field hydrothermal particle plume: Nature, v. 322, p. 169–171, doi:10.1038/322169a0.

Cowen, J.P., Massoth, G.J., and Feely, R.A., 1990, Scavenging rates of dissolved manganese in a hydrothermal vent plume: Deep Sea Research Part A, Oceanographic Research Papers, v. 37, p. 1619–1637, doi:10.1016/0198-0149(90)90065-4.

D. C. Lund, P. D. Asimow, K. A. Farley, T. O. Rooney, E. Seeley, E. W. Jackson, Z.M.D., 2016, Enhanced East Pacific Rise hydrothermal activity during the last two glacial terminations: Science, v. 351, p. 475–478, doi:10.1126/science.aad8868.

Von Damm, K., 1990, Seafloor Hydrothermal Activity: Black Smoker Chemistry And Chimneys: Annual Review of Earth and Planetary Sciences, doi:10.1146/annurev.earth.18.1.173.

Von Damm, K.L., and Bischoff, J.L., 1987, Chemistry of hydrothermal solutions from the southern Juan de Fuca Ridge.: Journal of Geophysical Research, v. 92, p. 334–346, doi:10.1029/jb092ib11p11334.

Dunk, R.M., and Mills, R.A., 2006, The impact of oxic alteration on plume-derived transition metals in ridge flank sediments from the East Pacific Rise: Marine Geology, v. 229, p. 133–157, doi:10.1016/j.margeo.2006.03.007.

Dymond, J., and Roth, S., 1988, Plume dispersed hydrothermal particles: A time-series record of settling flux from the Endeavour Ridge using moored sensors: Geochimica et Cosmochimica Acta, v. 52, p. 2525–2536, doi:10.1016/0016-7037(88)90310-9.

Edmonds, H.N., and German, C.R., 2004, Particle geochemistry in the Rainbow hydrothermal plume, Mid-Atlantic Ridge: Geochimica et Cosmochimica Acta, v. 68, p. 759–772, doi:10.1016/S0016-7037(03)00498-8.

Eggins, S.M., Woodhead, J.D., Kinsley, L.P.J., Mortimer, G.E., Sylvester, P., Mcculloch, M.T., Hergt, J.M., and Handler, M.R., 1997, A simple method for the precise determination of >40 trace elements in geological samples by ICPMS using enriched isotope internal standardisation: Chemical Geology, v. 134, p. 311–326.

Feely, R.A., 1987, Composition and dissolution of black smoker particulates from active vents on the Juan de Fuca Ridge.: Journal of Geophysical Research, v. 92, doi:10.1029/jb092ib11p11347.

Feely, R.A., Massoth, G.J., Baker, E.T., Lebon, G.T., and Geiselman, T.L., 1992, Tracking the Dispersal of Hydrothermal PLumes From the Juan de Fuca Ridge Usingn Suspended Matter Compositions: v. 97, p. 3457–3468.

Feely, R.A., Massoth, G.J., Trefry, J.H., Baker, E.T., Paulson, A.J., and Lebon, G.T., 1994, Composition and sedimentation of hydrothermal plume particles from north Cleft segment, Juan de Fuca Ridge: Journal of Geophysical Research, v. 99, p. 4985–5006, doi:10.1029/93JB02509.

Feely, A., Trefry, J.H., Lebon, G.T., and German, R., 1998, The relationship between P/Fe and V/Fe ratios in hydrothermal precipitates and dissolved in phosphate in seawater.: v. 25, p. 2253–2256.

Feely, R.A., Trefry, J.H., Massoth, G.J., and Metz, S., 1991, A comparison of the scavenging of phosphorus and arsenic from seawater by hydrothermal iron oxyhydroxides in the Atlantic and Pacific Oceans: Deep Sea Research Part A, Oceanographic Research Papers, v. 38, p. 617–623, doi:10.1016/0198-0149(91)90001-V.

Field, M.P., and Sherrell, R.M., 2000, Dissolved and particulate Fe in a hydrothermal plume at 9°45'N, East Pacific Rise: Geochimica et Cosmochimica Acta, v. 64, p. 619–628, doi:10.1016/s0016-7037(99)00333-6.

Findlay, A.J., Estes, E.R., Gartman, A., Yücel, M., Kamyshny, A., and Luther, G.W., 2019, Iron and sulfide nanoparticle formation and transport in nascent hydrothermal vent plumes: Nature Communications, v. 10, p. 1–7, doi:10.1038/s41467-019-09580-5.

Fitzsimmons, J.N., Boyle, E.A., and Jenkins, W.J., 2014, Distal transport of dissolved hydrothermal iron in the deep South Pacific Ocean: Proceedings of the National Academy of Sciences of the United States of America, v. 111, p. 16654–16661, doi:10.1073/pnas.1418778111.

Fitzsimmons, J.N., John, S.G., Marsay, C.M., Hoffman, C.L., Nicholas, S.L., Toner, B.M., German, C.R., and Sherrell, R.M., 2017, Iron persistence in a distal hydrothermal plume supported by dissolved-particulate exchange: Nature Geoscience, v. 10, p. 195–201, doi:10.1038/ngeo2900.

German, C.R. et al., 1997, Hydrothermal scavenging on the Juan de Fuca Ridge: 230Thxs, 10Be, and REEs in ridge-flank sediments: Geochimica et Cosmochimica Acta, v. 61, p. 4067–4078, doi:10.1016/s0016-7037(97)00230-5.

German, C.R., Campbell, A.C., and Edmond, J.M., 1991, Hydrothermal scavenging at the Mid-Atlantic Ridge: Modification of trace element dissolved fluxes: Earth and Planetary Science Letters, v. 107, p. 101–114, doi:10.1016/0012-821X(91)90047-L.

German, C.R., Colley, S., Palmer, M.R., Khripounoff, A., and Klinkhammer, G.P., 2002, Hydrothermal plume-particle fluxes at 13°N on the East Pacific Rise: Deep-Sea Research Part I: Oceanographic Research Papers, v. 49, p. 1921–1940, doi:10.1016/S0967-0637(02)00086-9.

German, C.R., Klinkhammer, G.P., Edmond, J.M., Mura, A., and Elderfield, H., 1990, Hydrothermal scavenging of rare-earth elements in the ocean: Nature, v. 345, p. 516–518, doi:10.1038/345516a0.

German, C.R., and Seyfried, W.E., 2013, Hydrothermal Processes: Elsevier Ltd., v. 8, 191–233 p., doi:10.1016/B978-0-08-095975-7.00607-0.

GOFS, 1989, Sediment Trap Technology and Sampling: Report of the U.S. GOFS Working Group on Sediment Trap Technology and Sampling, p. 101, http://scholar.google.com/scholar?hl=en&btnG=Search&q=intitle:SEDIMENT+TRAP+TECHNOLOGY+AND+SAMPLING#0%5Cnhttp://scholar.google.com/scholar?hl=en&btnG=Search&q=intitle:Sediment+trap+technology+and+sampling#0.

Hannington, M., Jamieson, J., Monecke, T., Petersen, S., and Beaulieu, S., 2011, The abundance of seafloor massive sulfide deposits: Geology, doi:10.1130/G32468.1.

Hannington, M.D., De Ronde, C.E.J., and Petersen, S., 2005, Sea-Floor Tectonics and Submarine Hydrothermal Systems.:

Hauser, P.C., 2019, Coulometry: Encyclopedia of Analytical Science, v. 2, p. 202–209, doi:10.1016/B978-0-12-409547-2.14436-1.

Hayes, C.T. et al., 2015, Intensity of Th and Pa scavenging partitioned by particle chemistry in the North Atlantic Ocean: Marine Chemistry, v. 170, p. 49–60, doi:10.1016/j.marchem.2015.01.006.

Haymon, R.M., 1983, Growth history of hydrothermal black smoker chimneys: v. 301, p. 695–698.

Hrischeva, E., and Scott, S.D., 2007, Geochemistry and morphology of metalliferous sediments and oxyhydroxides from the Endeavour segment, Juan de Fuca Ridge: Geochimica et Cosmochimica Acta, v. 71, p. 3476–3497, doi:10.1016/j.gca.2007.03.024.

Jamieson, J.W., Hannington, M.D., Clague, D.A., Kelley, D.S., Delaney, J.R., Holden, J.F., Tivey, M.K., and Kimpe, L.E., 2013, Sulfide geochronology along the Endeavour Segment of the Juan de Fuca Ridge: v. 14, doi:10.1002/ggge.20133.

Janecky, D.R., and Seyfried, W.E., 1983, The solubility of magnesium-hydroxide sulfate-hydrate in seawater at elevated temperatures and pressures.: American Journal of Science, v. 283, p. 831–860, doi:10.2475/ajs.283.8.831.

Jull, M., and McKenzie, D., 1996, The effect of deglaciation on mantle melting beneath Iceland: The effect of deglaciation on mantle melting beneath Iceland, v. 101 B10, p. 21815–21828, doi:10.1029/96jb01308.

Kadko, D., Feely, R., and Massoth, G., 1994, Scavenging of 234Th and phosphorus removal from the hydrothermal effluent plume over the north Cleft segment of the Juan de Fuca Ridge: Journal of Geophysical Research, v. 99, p. 5017–5024, doi:10.1029/93JB02952.

Kelley, D.S. et al., 2012, Endeavour segment of the juan de Fuca ridge, one of the mos t remarkable places on earth: Oceanography, v. 25, p. 44–61, doi:10.5670/oceanog.2012.03.

Klar, J.K., James, R.H., Gibbs, D., Lough, A., Parkinson, I., Milton, J.A., Hawkes, J.A., and Connelly, D.P., 2017, Isotopic signature of dissolved iron delivered to the Southern Ocean from hydrothermal vents in the East Scotia Sea: Geology, v. 45, p. 351–354, doi:10.1130/G38432.1.

Klinkhammer, G.P., Elderfield, H., Edmond, J.M., and Mitra, A., 1994, Geochemical implications of rare earth element patterns in hydrothermal fluids from mid-ocean ridges: Geochimica et Cosmochimica Acta, v. 58, p. 5105–5113, doi:10.1016/0016-7037(94)90297-6.

Landing, W.M., and Bruland, K.W., 1980, Manganese in the North Pacific: Earth and Planetary Science Letters, v. 49, p. 45–56, doi:10.1016/0012-821X(80)90149-1.

Lavelle, J.W., Cowen, J.P., and Massoth, G.J., 1992, A model for the deposition of hydrothermal manganese near ridge crests: Journal of Geophysical Research, v. 97, p. 7413–7427, doi:10.1029/92JC00406.

Lee, J.M. et al., 2021, Changing chemistry of particulate manganese in the near- and far-field hydrothermal plumes from 15°S East Pacific Rise and its influence on metal scavenging: Geochimica et Cosmochimica Acta, v. 300, p. 95–118, doi:10.1016/j.gca.2021.02.020.

Libes, S.M., 2009, Introduction to Marine Biogeochemistry: Amsterdam ; Boston : Elsevier/Academic, 909 p.

Longerich, H.P., Jenner, G.A., Fryer, B.J., and Jackson, S.E., 1990, Inductively coupled plasma-mass spectrometric analysis of geological samples: A critical evaluation based on case studies: Chemical Geology, v. 83, p. 105–118, doi:10.1016/0009-2541(90)90143-U.

Lund, D.C., and Asimow, P.D., 2011, Does sea level influence mid-ocean ridge magmatism on Milankovitch timescales? Geochemistry, Geophysics, Geosystems, v. 12, doi:10.1029/2011GC003693.

Lyle, M., 1983, The Brown-Green Color Transition in Marine Sediments : A Marker of the Fe (III) -Fe (II) Redox Boundary: Limnology, v. 28, p. 1026–1033.

Martin, J.H., Gordon, R.M., Fitzwater, S., and Broenkow, W.W., 1989, Vertex: phytoplankton/iron studies in the Gulf of Alaska: Deep Sea Research Part A, Oceanographic Research Papers, v. 36, p. 649–680, doi:10.1016/0198-0149(89)90144-1.

Massoth, G.J., 1994, Temporal and spatial variability of hydrothermal manganese and iron at Cleft segment, Juan de Fuca Ridge: Journal of Geophysical Research, v. 99, p. 4905–4923, doi:10.1029/93JB02799.

Metz, Simone; Trefry, J.H., 1989, Role of hydrothermal precipitates in the geochemical cycling of Vanadium: Nature, v. 342, p. 531–533.

Michard, A., and Albarède, F., 1986, The REE content of some hydrothermal fluids: Chemical Geology, v. 55, p. 51–60, doi:10.1016/0009-2541(86)90127-0.

Michard, A., Albarède, F., Michard, G., Minster, J.F., and Charlou, J.L., 1983, Rare-earth elements and uranium in high-temperature solutions from east pacific rise hydrothermal vent field (13 °N): Nature, v. 303, p. 795–797, doi:10.1038/303795a0.

Middleton, J.L., Langmuir, C.H., Mukhopadhyay, S., McManus, J.F., and Mitrovica, J.X., 2016, Hydrothermal iron flux variability following rapid sea level changes: Geophysical Research Letters, v. 43, p. 3848–3856, doi:10.1002/2016GL068408.

Mills, R.A., Taylor, S.L., Plike, H., and Thomson, J., 2010, Hydrothermal sediments record changes in deep water oxygen content in the SE Pacific: Paleoceanography, v. 25, p. 1–16, doi:10.1029/2010PA001959.

Mitra, A., Elderfield, H., and Greaves, M.J., 1994, Rare earth elements in submarine hydrothermal fluids and plumes from the Mid-Atlantic Ridge: Marine Chemistry, v. 46, p.

217–235, doi:10.1016/0304-4203(94)90079-5.

Morford, J.L., Emerson, S.R., Breckel, E.J., and Kim, S.H., 2005, Diagenesis of oxyanions (V, U, Re, and Mo) in pore waters and sediments from a continental margin: Geochimica et Cosmochimica Acta, v. 69, p. 5021–5032, doi:10.1016/j.gca.2005.05.015.

Mottl, M.J., and McConachy, T.F., 1990, Chemical processes in buoyant hydrothermal plumes on the East Pacific Rise near 21°N: Geochimica et Cosmochimica Acta, v. 54, p. 1911–1927, doi:10.1016/0016-7037(90)90261-I.

Murray, R.W., and Leinen, M., 1993, Chemical transport to the seafloor of the equatorial Pacific Ocean across a latitudinal transect at 135°W: Tracking sedimentary major, trace, and rare earth element fluxes at the Equator and the Intertropical Convergence Zone: Geochimica et Cosmochimica Acta, v. 57, p. 4141–4163, doi:10.1016/0016-7037(93)90312-K.

Owen, R.M., and Olivarez, A.M., 1988, Geochemistry of rare earth elements in pacific hydrothermal sediments: Marine Chemistry, v. 25, p. 183–196, doi:10.1016/0304-4203(88)90063-1.

Poulton, S.W., and Canfield, D.E., 2006, Co-diagenesis of iron and phosphorus in hydrothermal sediments from the southern East Pacific Rise: Implications for the evaluation of paleoseawater phosphate concentrations: Geochimica et Cosmochimica Acta, v. 70, p. 5883–5898, doi:10.1016/j.gca.2006.01.030.

Rafter, Patrick A.; Carriquiry, Jose; Herguera, Juan-Carlos; Hain, Mathis; Solomon, Evan; Southon, J., 2019, Anomalous > 2000 - Year - Old Surface Ocean Radiocarbon Age as Evidence for Deglacial Geologic Carbon Release Geophysical Research Letters: Geophysical Research Letters, v. 46.

Rouxel, O., Toner, B.M., Manganini, S.J., and German, C.R., 2016, Geochemistry and iron isotope systematics of hydrothermal plume fall-out at East Pacific Rise 9°50'N: Chemical Geology, v. 441, p. 212–234, doi:10.1016/j.chemgeo.2016.08.027.

Rudnick, R.L., and Gao, S., 2013, Composition of the Continental Crust: Elsevier Ltd., v. 4, 1–51 p., doi:10.1016/B978-0-08-095975-7.00301-6.

Rudnicki, M.D., and Elderfield, H., 1993, A chemical model of the buoyant and neutrally buoyant plume above the TAG vent field, 26 degrees N, Mid-Atlantic Ridge: Geochimica et Cosmochimica Acta, v. 57, p. 2939–2957, doi:10.1016/0016-7037(93)90285-5.

Scholz, F., McManus, J., and Sommer, S., 2013, The manganese and iron shuttle in a modern euxinic basin and implications for molybdenum cycling at euxinic ocean margins: Chemical Geology, v. 355, p. 56–68, doi:10.1016/j.chemgeo.2013.07.006.

Seyfried, W.E., Seewald, J.S., Berndt, M.E., Ding, K., and Foustoukos, D.I., 2003, Chemistry of hydrothermal vent fluids from the Main Endeavour Field, northern Juan de Fuca Ridge: Geochemical controls in the aftermath of June 1999 seismic events: Journal of Geophysical Research: Solid Earth, v. 108, p. 1–23, doi:10.1029/2002jb001957.

Shimmield, G.B., and Price, N.B., 1986, The behaviour of molybdenum and manganese during early sediment diagenesis - offshore Baja California, Mexico: Marine Chemistry, v. 19, p. 261–280, doi:10.1016/0304-4203(86)90027-7.

Siegel, D.A., and Deuser, W.G., 1997, Trajectories of sinking particles in the Sargasso Sea: Modeling of statistical funnels above deep-ocean sediment traps: Deep-Sea Research Part I: Oceanographic Research Papers, v. 44, p. 1519–1541, doi:10.1016/S0967-0637(97)00028-9.

Southon, John' Santos, Guaciara; Druffel-Rodriguez, Kevin;Druffel, Ellen; Trumbore, Sue; Griffin, Sheila; Ali, Shahla, Mazon, M., 2004, The Keck Carbon Cycle AMS Laboratory, University of California Irvine: Initial Operation and A Backgorund Surprise: Radiocarbon, v. 46, p. 41–49.

Speer, Kevin G., and K.R.H., 1996, Hydrothermal plumes: a review of flow and fluxes: Geological Society, London, Special Publications, v. 87, p. 373–385.

Thomson, R.E., Mihly, S.F., McDuff, R.E., and Stahr, S.R.V.& F.R., 2003, Constrained circulation at Endeavour ridge facilitates colonization by vent larvae: Nature, v. 424, p. 542–545, doi:10.1038/nature01814.

Thomson, R.E., Subbotina, M.M., and Anisimov, M. V., 2005, Numerical simulation of hydrothermal vent-induced circulation at Endeavour Ridge: Journal of Geophysical Research: Oceans, v. 110, p. 1–14, doi:10.1029/2004JC002337.

Toner, B.M., Fakra, S.C., Manganini, S.J., Santelli, C.M., Marcus, M.A., Moffett, J.W., Rouxel, O., German, C.R., and Edwards, K.J., 2009, Preservation of iron(II) by carbon-rich matrices in a hydrothermal plume: Nature Geoscience, v. 2, p. 197–201, doi:10.1038/ngeo433.

Waeles, M., Cotte, L., Pernet-Coudrier, B., Chavagnac, V., Cathalot, C., Leleu, T., Laës-Huon, A., Perhirin, A., Riso, R.D., and Sarradin, P.M., 2017, On the early fate of hydrothermal iron at deep-sea vents: A reassessment after in situ filtration: Geophysical Research Letters, v. 44, p. 4233–4240, doi:10.1002/2017GL073315.

Wilschefski, S.C., and Baxter, M.R., 2019, Inductively Coupled Plasma Mass Spectrometry: Introduction to Analytical Aspects: Clinical Biochemist Reviews, v. 40, p. 115–133, doi:10.33176/AACB-19-00024.

Yücel, M., Gartman, A., Chan, C.S., and Luther, G.W., 2011, Hydrothermal vents as a kinetically stable source of iron-sulphide-bearing nanoparticles to the ocean: Nature Geoscience, v. 4, p. 367–371, doi:10.1038/ngeo1148.

https://www.uicinc.com/carbon-dioxide-coulometer/